

# Nanoelectrochemistry: Metal Nanoparticles, Nanoelectrodes, and Nanopores

Royce W. Murray\*

Kenan Laboratories of Chemistry, University of North Carolina, Chapel Hill, North Carolina 27599-3290

Received July 27, 2007

## Contents

1. Introduction and Nanoboundaries	2688
2. Electrochemistry of Metal Nanoparticles	2688
3. Voltammetry of Solutions of Isolatable Nanoparticles	2689
3.1. Bulk-Continuum Voltammetry	2691
3.2. Quantized Double Layer Charging Voltammetry	2693
3.3. Voltammetry of Molecule-like Nanoparticles	2696
3.4. Electron Transfer Chemistry of Nanoparticle Solutions	2699
3.5. Voltammetry of Nanoparticles with Molecular Redox Labels	2701
4. Electrochemistry of Films of Nanoparticles	2702
4.1. Electrochemistry of Monolayers of Nanoparticles	2703
4.2. Nanoparticle Films Made by Langmuir Methods	2703
4.3. Electrochemistry of Multilayer Films of Nanoparticles	2704
4.3.1. Films Wetted by Electrolyte Solutions	2704
4.3.2. Electronic Conductivity of Dry Films	2706
5. Electrochemistry at Nanoscopic Electrodes	2709
5.1. Nanoelectrode Fabrication and Characterization	2709
5.2. Nanoelectrode Properties	2710
6. Electrochemistry at Single Nanopores	2713
6.1. Single Nanopores in Membranes	2713
6.2. Nanopore Electrodes	2716
7. Acknowledgments	2717
8. References	2717

## 1. Introduction and Nanoboundaries

Nano- is a big prefix-word. Much of contemporary chemistry focuses on small scale structures, and indeed, molecular science is intrinsically on the nanometer scale. Selecting material for this review of “nanoelectrochemistry” involved a necessary arbitrariness of defining what “nano” means. Here, it refers to a dimensional scale of electrodes and electrochemical events, as opposed to time or volume or mass. Still, most of molecular chemistry fits within the 1–1000 nm range of dimensions, as does a substantial body of charged or conducting substances, e.g., micro- and nanoparticles, colloids, emulsions, and aerosols. The topology of conducting substances can have nanoscopic dimensions, with mesoporous materials such as aerogels and xerogels being contemporary examples. These are important topics,

as are nanoparticle applications in bioanalysis, catalysis, and electrocatalysis, and nanomaterials such as fullerenes, carbon nanotubes and networks, semiconductor nanoparticles, and arrays of nanoelectrodes and nanopores. With apologies to those topics, I have chosen to whittle the scenery down to the electrochemistry of nanoparticles, and single nanoelectrodes and nanopores. Within these, attention will be biased toward metal nanoparticles having dimensions of only a small number of nanometers, because it is in the 10 nm and lower size range where many significant recent advances have been made. Similarly, I will focus mainly on single nanoelectrodes and nanopores, as opposed to arrays thereof. The literature cited here is predominantly not over a decade old; a lot has happened, and quickly. I hope the reader will find it an interesting decade.

What has promoted the rapid advances in the 1–10 nm range of dimensions? For nanoparticles, progress has been stimulated by synthetic innovations; for single nanoelectrodes and single nanopores, similarly by advances in methods of fabrication. Further, while making something that is really small can be special, it does not push science forward unless one can demonstrate its size and shape and chemical composition. So some substantial attention will be given to developments in fabrication and characterization. Knowing what you have prompts the more interesting and burning questions of how do its properties (of any kind, spectroscopic, electron transfer, etc). depend on its size, on the dimensions of other substances and structures that it interacts with (as in a nanopore), on the particular geometry of the small size, and of course on the extent that the chemist and electrochemist can tailor the composition and/or surface of the small particle/electrode/pore object to further expand its range of properties and usefulness. The authors cited in this report are leaving the first tracks—to some extent tentative tracks—in the scientific sand in these areas of nanoscience.

## 2. Electrochemistry of Metal Nanoparticles

Colloid chemistry is a discipline with great importance to both science and technology.<sup>1–3</sup> The electrical behavior of colloidal dispersions in solutions classically encompasses colloidal nanoparticles with surface charges caused by adsorption of small ions, surfactants, or polyelectrolytes and with consequent electrokinetic properties. The surface charges act as stabilizers, repelling the nanoparticles from one another, unless a high ambient electrolyte population screens the charges, or their stabilizing layers hydrophobically interact (in an aqueous dispersion), in which case the dispersion can become unstable and aggregation or flocculation occurs with a usual result of precipitation. Such phenomena have great practical importance in chemical

\* E-mail, rwm@email.unc.edu; telephone, 919-962-6296; fax, 919-962-2542.



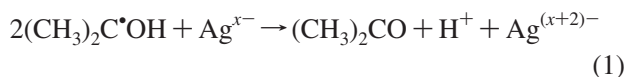
Royce W. Murray is Kenan Professor of Chemistry at the University of North Carolina at Chapel Hill. He studied with Professor Richard C. Bowers at Northwestern University and joined the UNC faculty in 1960. He is a member of the National Academy of Sciences and of the American Academy of Arts and Sciences and has served since 1991 as Editor-in-Chief of the ACS journal *Analytical Chemistry*. His research interests include molecular design of electrode surfaces and nanoparticles, electrochemically reactive ionic liquids, mass transport and electron transfer dynamics, and the analytical chemistry and properties of metal quantum dots.

manufacturing and other chemical processes, in sanitary water treatment, and in ocean chemistry, among others.

Colloids, or metal sols, have been known for a very long time, dating back to ancient techniques for imparting colors to glass. That such colorations are scattering phenomena was eventually qualitatively explained by Michael Faraday<sup>4</sup> in the middle of the 19th century. Our understanding of the optical coloration and absorbance spectra of metal nanoparticles was placed onto a quantitative footing by Mie<sup>5</sup> at the beginning of the 20th century.

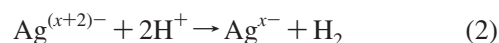
Metal colloids, and semiconductor colloids, exhibit the same surface ionic charging and electrokinetic properties as other colloids, but they also are able to act as electron donors and acceptors. This is an important distinction that was recognized in early papers by Henglein<sup>6</sup> and Grätzel<sup>7</sup> dealing, respectively, with electron storage on Ag nanoparticles during pulse radiolysis and with photocatalytic water reduction in the presence of colloidal Pt. The metal nanoparticles were aptly referred to as *colloidal microelectrodes*. In informative reviews<sup>8,9</sup> of work done in his and others' laboratories in the 1970s and 1980s, Henglein noted that metal colloids, "although not connected to a battery which determines their potential" had been shown to participate in electron transfer reactions with radicals in solutions, thereby acting as catalysts—or in more contemporary language—as electron transfer mediators.

Henglein's insight originated in part from pulse radiolysis experiments leading to the formation of very small silver (and some other metals) nanoparticles and which evoked catalytic reductions of other substrates in solution by silver nanoparticles. One well studied reaction<sup>6,10</sup> was the pulse radiolysis of acetone, which under  $\gamma$ -ray illumination produces the highly reducing radical  $(\text{CH}_3)_2\text{C}^\bullet\text{OH}$ . This radical becomes oxidized, at a close to diffusion-controlled rate, upon contact with a Ag nanoparticle, driving the nanoparticle potential to a more negative, reducing value



The Ag nanoparticles are themselves produced by preceding pulse radiolysis of a  $\text{AgNO}_3$  solution and were stabilized

by sodium polyvinylsulfate as surfactant. Reaction 1 is followed by a much slower reduction (rate constant  $5 \times 10^{-17} \text{ cm}^{-2} \text{ s}^{-1}$ ) of protons by the charged Ag nanoparticle,



The course of reactions 1 and 2 could be followed by changes in the ionic conductance of the solution that occurred over millisecond and minute time scales, respectively. From the charge storage properties of the Ag nanoparticles, it was estimated that, under the irradiation conditions used, an approximately 4 nm diameter Ag nanoparticle could carry as many as 450 stored electrons, with a double layer capacity of  $43 \mu\text{F}/\text{cm}^2$  of the nanoparticle surface. Calculations indicated that as many as 300 electrons could persist on a nanoparticle for about 1 min after irradiation had ceased.

A number of other metal nanoparticle reactions were accessed through the pulse radiolysis approach.<sup>8,9,11,12</sup> Pulse radiolysis-driven formation of metal nanoparticles has been extended to other metals, including core-shell structures<sup>13–16</sup> Pd,<sup>17</sup> Hg,<sup>18</sup> Cu,<sup>19</sup> Pb,<sup>20</sup> Pt,<sup>21</sup> Sn,<sup>22</sup> and Cd,<sup>23</sup> and several semiconductors.<sup>11,12</sup>

Grätzel<sup>7</sup> recognized the role of redox charging of Pt colloids in experiments aimed at understanding how the colloid facilitates photoreduction of water to hydrogen. Methyl viologen can be reduced by electron transfer from the excited state (450 nm) of the metal complex  $[\text{Ru}(\text{bpy})_3]^{2+}$  (where bpy = 1,10-bipyridine), with fast rereduction of the  $[\text{Ru}(\text{bpy})_3]^{3+}$  photoproduct by EDTA (as a sacrificial electron donor). The methyl viologen radical rapidly transfers electron charge to the Pt colloid, which now acts as a reducing surface for the reduction of protons to hydrogen. The latter step was demonstrated unequivocally by showing that hydrogen is directly evolved in mixtures of reduced viologen and Pt colloid. McClendon<sup>24,25</sup> further probed the roles of solution pH and redox potential of the viologen mediator, and more explicitly dissected the viologen/ $\text{H}_2$  process as one driven by direct electrolytic reduction of the viologen. The explicit theory presented<sup>25</sup> by Bard for the current flow cast the potential of the Pt colloidal particles as a mixed potential whose value depended on the incoming reductive viologen charge and the rate of hydrogen evolution.

Experiments like the above illustrate the modern beginnings of electron transfer-oriented chemistry of metal nanoparticles. They showed that metal nanoparticles can act as soluble electrodes that can be cathodically charged with large overall populations of electrons and that the dynamics of their reaction chemistry with other solution constituents can be quantitatively assessed.

### 3. Voltammetry of Solutions of Isolatable Nanoparticles

Pulse radiolytic formation of metal nanoparticles, and charging them by reactions with radiolytically or photolytically generated radicals are powerful approaches to metal nanoparticle electron transfer chemistry but are ultimately constrained by the need for specialized radiolysis equipment and more particularly by an inability to isolate and further manipulate the nanoparticles employed. A continuing phase of research on metal and semiconductor nanoparticle electrochemistry has been stimulated by developments in synthesis that produce nanoparticles stable enough to be isolated, purified, and analytically characterized. Central in this change were new choices of stabilizing ligands for nanoparticles—whereby

elements of modern coordination chemistry were brought into play and started to supplant the weaker and less specific interactions of traditional surfactants and polymer electrolytes with nanoparticle surfaces. Prominent among these ligands were phosphenes,<sup>2,26,27</sup> phenanthrolines,<sup>2,28,29</sup> amines,<sup>2</sup> organothiolates,<sup>30</sup> and dendrimers.<sup>31</sup> Also synthetically central were bottom-up metal nucleation tactics giving access to smaller nanoparticle dimensions and to some degree lowered size dispersities. These synthetic tactics on the one hand aimed at trapping a limited number of metal ion precursors in a small, uniform volume—such as that of a dendrimer<sup>31</sup>—and then reducing them to form nanoparticles. In other procedures, the metal ion precursors are reduced in the presence of traditional but relatively weak stabilizers (such as the reduction of Au(III) by citrate), followed by displacement of the weak ligand stabilizers by more strongly binding ones, such as organothiols.<sup>32,33</sup> The nanoparticle is alternatively formed in the immediate presence of the strongly stabilizing ligand, such as the organothiol;<sup>30</sup> this particularly can lead to passivation of the nanoparticle to further growth at a small size. It is a generality that evolution of study into chemical properties rides on the shoulders of designed chemical syntheses.

These developments in stabilizing ligands and synthesis, occurring over the past decade for metal nanoparticles (~two decades for semiconductor nanoparticles), caused an intensification and broadening of interest in their chemistry and especially in the properties of those with very small dimensions. Bulk metallic objects have well-known optical properties—continua of electronic states—and reactivity properties when used as electrodes. Well-investigated metal complexes that in contrast contain only a single metal site, bonded to various and diverse ligands, also have spectral and electrochemical properties defined by discrete electronic levels and states. What lies in between? With decreasing size, at what dimension, and at what number of metal atoms, do the properties of the bulk metal start to change toward those of molecular complexes—the so-called “metal-to-molecule” transition? The idea of chemical and other properties that depend on and vary with physical dimension has fascinated chemists—and theorists—for a very long time, perhaps longest and most intensely for chemists interested in colloids and in catalysis of reactions. Henglein<sup>9</sup> aptly noted Ostwald’s prescience<sup>34</sup> about the transition of colloidal to molecular matter. The subject has been given new urgency by the steady, continuing, diminution of feature size in the microelectronics industry—which is literally a life’s-blood technology of modern science and society. This urgency, plus the urges of basic scientific exploration, has helped to birth the field of molecular electronics,<sup>35</sup> where one aims to use molecular or near-molecular materials to mimic essential electronic functions, such as those of transistors.

An ability to isolate a nanoparticle in a purified form, perhaps a dry form, and redissolve it without change or decomposition (avoiding, in particular, aggregation of the nanoparticle), is a liberating gift to innovation by the nanoparticle chemist, in several respects. Experimental openings are generated to (a) defining what the nanoparticle is, on increasingly definitive terms, including the extent to which it exhibits bulk metal-like as opposed to molecule-like properties, (b) incrementally modifying the nanoparticle composition/structure so as to determine which of and how much its components—nanoparticle or stabilizing ligand shell—influence its properties, and thereby learning how to

manipulate nanoparticle properties, and (c) learning how to induce interactions between nanoparticles that probe their ability to communicate with one another in order to evolve a further dimension of properties within the metal-to-molecule dimension transition. Attaining these goals remains in a somewhat primitive state, but quite considerable progress has issued from the simple fact of isolation of very small, stable, nonaggregating nanoparticle materials.

An issue in applying analytical and structural tools to identify a nanoparticle is whether to base the assignment on a combination of data that infer a formulaic composition (such as  $[\text{metal}]_x[\text{stabilizing ligands}]_{y,z}$ ) or to define it according to its diameter as inferred from, typically, TEM and as having a stabilizing layer of certain surfactants without count of their population. This issue is the same whether the nanoparticle is on the metal or molecule side of the metal-to-molecule transition. This author joined the formulaic camp,<sup>2</sup> which, while posing a severe challenge to the characterization, forces evolution of the tools of nanoparticle characterization to a higher level. One must admire work in which single crystal structural analysis leaves no ambiguity about composition; but for thiolated Au nanoparticles this has only recently<sup>36</sup> been achieved. When it has not, the real uncertainties involved in expressing analytical compositions must be conceded. A major uncertainty stems from the fact that a synthesized nanoparticle sample is almost never an entirely pure material, in terms of size monodispersity. The *polydispersity* of a characterized nanoparticle material generally requires—lacking an analysis that distinguishes individual compositions in a mixture, such as mass spectrometry—that one express composition as an *average*. Many investigators in the nanoparticle field have, on the other side, preferred to cite nanoparticle dimensions as inferred from, most usually, transmission electron microscopy (TEM) and to note the stabilizing chemical (also called a capping reagent or protecting reagent or ligand). This is predominant in the semiconductor nanoparticle field. This review is not about issues of nanoparticle characterization, but it is not possible to separate that subject’s involvement in gaining a basic understanding of the electrochemistry of the nanoparticle, and it will creep into the discussion below.

The development of nanoparticle stabilizing chemistry enabled direct voltammetric observations on solutions of nanoparticles. We turn now to examining electrochemical experiments done directly on nanoparticles, and the kinds of electrochemical responses. Consider a sample of highly purified metal nanoparticles, consisting of a core of metal atoms and surrounded by a monolayer of ligands that prevent agglomeration of the metal atom cores, and stably dissolved in a solvent containing an appropriate inert electrolyte. Consider, in principle, the electron transfer chemistry that this metal nanoparticle may undergo in voltammetry at a working electrode and how that voltammetry would change as a function of size of the nanoparticle. Three voltammetric regimes—defined by ranges of core size—can be imagined (all experimentally known). I label these *bulk-continuum*, *quantized double layer charging*, and *molecule-like*. In a fourth regime (also known experimentally), the nanoparticle ligand monolayer may contain some intrinsically electroactive groupings, whose voltammetry would add to that attributable to the nanoparticle core.



### 3.1. Bulk-Continuum Voltammetry

This voltammetric behavior is that of large nanoparticles, with large meaning  $>3\text{--}4\text{ nm}$ . A simple but fundamentally important relation that distinguishes such nanoparticles from even smaller ones is

$$\Delta V = ze/C_{\text{CLU}} \quad (3)$$

where  $\Delta V$  is the change in electrochemical potential of a nanoparticle with double layer capacitance  $C_{\text{CLU}}$ , that is incurred upon transfer of  $z$  electrons to/from the nanoparticle. The subscript “CLU” connotes the capacitance of an individual metal *cluster* (i.e., not surface area normalized). The value of  $\Delta V$  must be considered in light of the Boltzman thermal energy distribution factor, which is  $k_{\text{B}}T_{25} = 25.7\text{ meV}$  at room temperature. If  $\Delta V \leq$  this factor, then successive electron transfers to/from the nanoparticle will result in a continuous—as opposed to stepwise—change in the nanoparticle’s potential. This “bulk-continuum” behavior is that expected of nanoparticles having a sufficiently large  $C_{\text{CLU}}$ , namely  $> ca. 6\text{ aF}$ .

Thus, room temperature voltammetry of dissolved nanoparticles having  $C_{\text{CLU}} \geq 6\text{ aF}$  should result in smooth current–potential traces, whether in unstirred solution with linear potential scanning, as in cyclic voltammetry (CV), or with very slow potential scanning and hydrodynamic transport, as in rotated disk electrode (RDE) voltammetry. The capacitive charging currents due to transport of nanoparticles to the working electrode are under mass transport control and can thereby be distinguished from background currents such as working electrode double layer charging and slow parasitic, kinetically controlled faradaic reactions. The capacitance currents for electronically charging the nanoparticle should, for example, increase with the square root of the potential scan rate and of the electrode rotation rate, in CV and RDE experiments, respectively. In a potential step experiment in unstirred solution, the diffusing nanoparticles would produce a current that decays inversely with the square root of time. These relations come from the Randles, Levich, and Cottrell equations, respectively.<sup>37</sup>

The earliest example of bulk-continuum voltammetry of an isolatable nanoparticle was reported by Mulvaney et al.<sup>38</sup> for 10 nm diameter Ag nanoparticles protected by a layer of polyacrylic acid. The diffusion coefficient of the Ag nanoparticle ( $5 \times 10^{-7}\text{ cm}^2/\text{s}$ ) in aqueous  $\text{NaClO}_4$  was measured by dynamic light scattering. Scanning a working electrode to more positive potentials gave currents for oxidation of the nanoparticle and ultimate dissolution. Scanning to negative potentials gave featureless, gradually rising currents whose values were, by potential step chronoamperometry and rotated disk voltammetry, shown with the Cottrell and Levich equations<sup>37</sup> to be controlled by mass transport of the Ag nanoparticle. These equations are, respectively,

$$i = \frac{nFAD^{1/2}C_{\text{Ag}}}{\pi^{1/2}t^{1/2}} \quad (4)$$

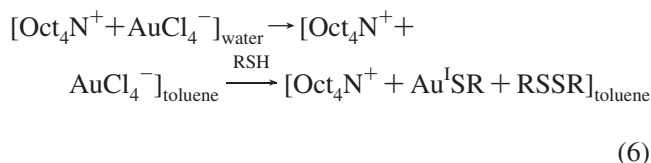
$$i = 0.62nFAD^{2/3}\omega^{1/2}v^{-1/6}C_{\text{Ag}} \quad (5)$$

Figure 1 shows that rotated disk electrode currents change linearly with  $[\text{rotation rate}, \omega]^{1/2}$ , which is a hydrodynamic mass transport criterion. Application<sup>38</sup> of the above equations gave the numbers ( $n$ ) of electrons transferred from working electrode to nanoparticle; for changes in potential of about

1 V, these were 1600 and 1650. A differently founded analysis of the blue shift of the Ag surface plasmon band maximum seen upon applying negative potentials to nanoparticles in an optically transparent thin layer cell gave a response of  $n = 1790$  electrons, roughly consistent with the RDE result.

This report showed that one can measure very large numbers of reducing equivalents stored on large metal nanoparticles that have large double layer capacitances. A nanoparticle surface area-normalized value of  $80\text{ }\mu\text{F}/\text{cm}^2$  was estimated. According to this value, eq 3 predicts a spacing between successive electrons transferred to the Ag of about 0.5 mV, which is much smaller than the resolution thermally imposed by  $k_{\text{B}}T_{25}$ . The observed current–potential responses accordingly contained no discontinuities relatable to successive, single, electron transfers.

Most subsequent direct voltammetry of metal nanoparticles has been on very small Au nanoparticles that are stabilized by organothiolate ligand monolayers. This kind of nanoparticle, called *monolayer protected clusters*, or MPCs, is prepared by a useful synthetic method—the “Brust synthesis”—reported by the Schiffrin laboratory.<sup>30</sup> Using the transfer reagent  $\text{Oct}_4\text{N}^+\text{Br}^-$ , chloroaurate is phase-transferred from water to toluene, where an organothiol is added, reducing the gold to a colorless  $\text{Au}^{\text{I}}$  thiolate complex, which typically is not isolated,



This reaction is followed by addition of a reducing agent, commonly  $\text{BH}_4^-$ . The concurrent presence of the thiol while Au nanoparticles are being reductively formed tends to constrain the nanoparticle sizes into the interesting, very small size regime. The choices<sup>39</sup> of reaction temperature, thiol:Au feed ratio, and other variables roughly influence the *average* MPC product core size, which can vary from about 5 down to 1 nm but is, in the raw reaction product, typically a mixture of Au core sizes. The nature of the organothiolate ligand dominates the MPC solubility properties; for example, those based on alkanethiolate or arylthiolate ligands are soluble in moderately polar to nonpolar media but not water. Solubility properties are important as regards fractionation procedures to lessen the MPC product’s size polydispersity.

MPCs can be elaborated beyond their initial protecting thiolate monolayers by replacing some of those ligands with different thiolates, in a reaction called “place exchange” or “ligand exchange”.<sup>36,41,42a</sup> The MPC is incubated in a solution of the new ligand for a period of time, and after product isolation, the extent of exchange in the isolated mixed monolayer MPC is evaluated (typically) by  $^1\text{H}$  NMR. (The nanoparticle-related broadening of the NMR resonances—which affects the mixed monolayer analysis—can be combated<sup>42b</sup> by decomposition of the MPC sample using cyanide or iodine, liberating free disulfides with sharp NMR resonances. The rates of decomposition vary with the specific ligands.<sup>42c</sup>) The number of ligands exchanged is a distribution, so the NMR analysis gives only an *average*. In this way, the MPC chemistry can be diversified by incorporating thiolate ligands with interesting terminal groupings, such as redox centers, as discussed later, or by generating sites for coupling

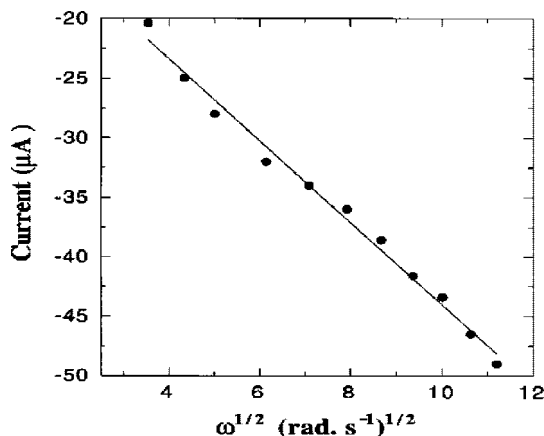


**Figure 1.** Levich plot of the limiting current vs square root of the RDE angular rotation rate. Solution conditions given in ref 38. Solution was  $N_2$ -saturated. Reprinted with permission from ref 38. Copyright 1997 American Chemical Society.

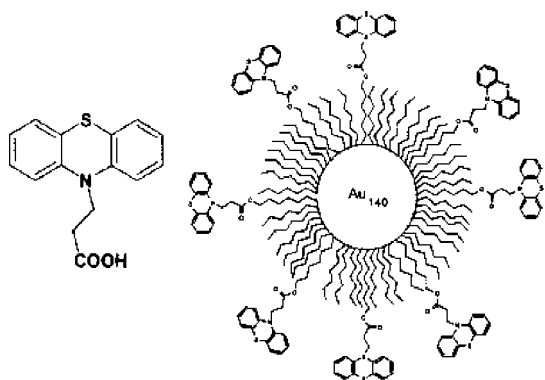


**Figure 2.** Cartoon of a phenothiazine labeled  $Au_{140}$  MPC. Reprinted with permission from ref 41. Copyright 2001 American Chemical Society.

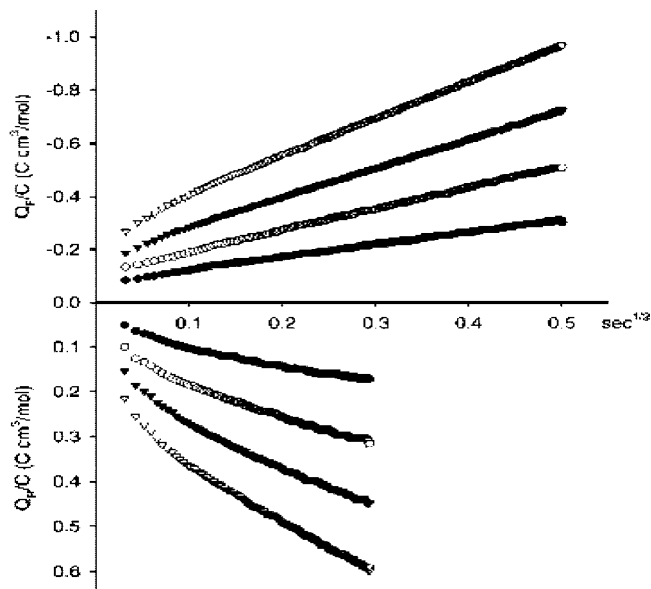


**Figure 3.** Chronocoulometry plots of concentration-normalized  $Q_F$  and  $Q_R$  against  $t^{1/2}$  (upper) and  $\tau$  (lower), respectively, for a  $48 \mu M$  solution of C6 MPC-A in methylene chloride/ $0.05 M Bu_4NClO_4$  at a Pt electrode.  $E_{FINAL} = +200$  (closed circles),  $+400$  (open circles),  $+600$  (closed triangles), and  $+800$  mV (open triangles);  $E_{INIT} = -200$  mV. Reprinted with permission from ref 41. Copyright 2001 American Chemical Society.

reactions where other entities can be subsequently bound. The nanoparticle cartoon in Figure 2 illustrates<sup>41</sup> the latter

with an MPC initially made with an octanethiolate monolayer into which was exchanged some  $\omega$ -hydroxyoctanethiolate ligands, that were in turn esterified with a phenothiazine carboxylic acid derivative.

The thiolate stabilized Au nanoparticle (MPC) has stability characteristics that allow fractionation into more monodisperse samples than the initial synthesis yields, and thusly, the electrochemical literature for Au MPCs is much more highly developed than that for other metals. An additional fact is you cannot study nanoparticle properties as a function of size if you cannot fractionate them by size, so substantial effort has been expended on this mundane issue.

Voltammetry that resembles bulk-continuum voltammetry has been reported for Au MPCs coated with hexanethiolate ligand shells. Mass transport control for charging of the MPC cores by a macroscopic working electrode was, for example, demonstrated by experiments such as that in Figure 3, where double potential step chronocoulometry<sup>41</sup> was used in forward- and back-potential steps of equal magnitude ( $\Delta E_F = \Delta E_R$ ), reversing the potential step after time  $\tau$ . Time-dependent charges for a diffusion-controlled electrode reaction in this method are given by<sup>37</sup>

$$Q_F = \frac{-2[\Delta E_F]C_{CLU}FAD_{CLU}^{1/2}Ct^{1/2}}{e\pi^{1/2}} - [\Delta E_F] \left[ AQ_{DL} + \frac{C_{CLU}FAG_{INIT}}{e} \right] \quad (7)$$

$$Q_R = \frac{2[\Delta E_R]C_{CLU}FAD_{CLU}^{1/2}C\theta}{e\pi^{1/2}} + [\Delta E_R] \left[ AQ_{DL} + \frac{C_{CLU}FAG_{FINAL}}{e} \right] \quad (8)$$

where  $\theta = [\tau^{1/2} + (t - \tau)^{1/2} - t^{1/2}]$  and  $t$  is time. The term  $(\Delta E)C_{CLU}/e = n_{DL}$  is the average number of electrons passed to charge each MPC's double layer, and the terms  $\Gamma_{INIT}$  and  $\Gamma_{FINAL}$  account for a small amount of physisorption of the MPCs onto the working electrode. (These relations have origin in older experiments<sup>37</sup> aimed at measuring adsorption of metal complexes on electrodes). The slopes of plots of the electrochemical charge passed to the MPCs, against the forward and reverse time parameters, yield an average value of  $C_{CLU} = 1.2$  aF. The MPC diffusion coefficient ( $D = 2.5 \times 10^{-6} \text{ cm}^2/\text{s}$ ) was measured using MPCs labeled with a few phenothiazine redox moieties in their monolayers (e.g., the MPC in Figure 2).

The roughly eight electrons transferred in the  $\Delta E = 1$  V step experiment<sup>41</sup> in Figure 3 contrasts sharply with the roughly 1600 electrons transferred in experiments such as those of Figure 1. This 200-fold difference is jointly rooted in the roughly 10-fold difference in surface area of the Ag and Au cores, and in their 20-fold different double layer capacitances ( $80$  vs  $4 \mu\text{F}/\text{cm}^2$ ). The small capacitance of the Au MPC interface arises from the low dielectric constant of the alkanethiolate protecting monolayer, which is a major factor facilitating electrochemical observation of the charging features of MPCs with even smaller cores, discussed below.

Bulk-continuum-like voltammetry was also seen for other MPCs bearing redox moieties in their protecting monolayers, namely ferrocene<sup>40,42</sup> and viologen,<sup>43</sup> at potentials where the redox groups were silent. Hydrodynamic mass transport control of MPC core charging was established using rotating disk electrodes, by observing that the (smooth)  $\Delta i/\Delta E$  slopes

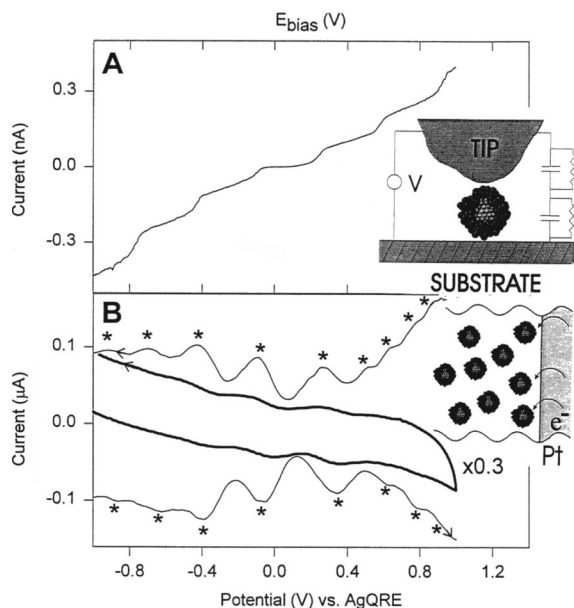


**Figure 4.** (inset) Au STM tip addressing a single cluster adsorbed on an Au-on-mica substrate and (top curve) Coulomb staircase  $I$ - $V$  curve at 83 K; potential is tip-substrate bias; equivalent circuit of the double tunnel junction gives capacitances  $C_{\text{upper}} = 0.59$  aF and  $C_{\text{lower}} = 0.48$  aF. Lower curve: voltammetry (CV s, 100 mV/s; DPV, \* are current peaks, 20 mV/s, 25 mV pulse, top and bottom are negative and positive scans, respectively) of a 0.1 mM 28 kDa cluster solution in 2:1 toluene:acetonitrile/0.05 M  $\text{Hx}_4\text{NClO}_4$  at a  $7.9 \times 10^{-3}$  cm<sup>2</sup> Pt electrode, 298 K, Ag wire pseudoreference electrode. Reprinted with permission from ref 44a. Copyright 1997 American Chemical Society.

were proportional to the square root of the electrode rotation rate. This dependency is predicted<sup>40</sup> for charging of the MPC core double layers.

### 3.2. Quantized Double Layer Charging Voltammetry

In this regime of nanoparticle voltammetry, the MPCs behave as quantum capacitors. Equation 3 teaches that a sufficiently small nanoparticle double layer capacitance ( $C_{\text{nanoparticle}} = C_{\text{MPC}} = C_{\text{CLU}}$ ) should cause the potential interval between successive single-electron changes in the electronic charge on the nanoparticle core to become experimentally observable. The discussion of eq 3 also teaches that not only must the nanoparticle be dimensionally small but it must also have a small double layer (charge/area) capacitance. In this regard, use of alkanethiolate coated nanoparticles is an apt choice to explore quantized double layer (QDL) charging of nanoparticles.

Figure 4, panel B shows the first reported<sup>44a</sup> example of QDL charging voltammetry, done on size-fractionated octanethiolate-coated Au MPCs. These MPCs were determined by laser desorption-ionization (LDI) mass spectrometry to have cores of mass  $\sim 28$  KDa, which means roughly 146 Au atoms/core. Panel A shows the variation of tip current with tip potential in scanning tunneling spectroscopy of a single MPC resting on a cold (83 K) surface. The current steps, spaced at regular intervals, represent a coulomb staircase of successive one electron changes in the electronic charge resident on the MPC core. Panel B shows room temperature cyclic (CV) and differential pulse (DPV)<sup>37</sup> voltammetry of a solution of the same MPCs. The potential spacing between the current peaks (especially that nearest 0 V) is very similar to that in panel A, supporting the notion

that the voltammetric features also have basically electrostatic origins. The current peaks are more prominent in the DPV experiment than in the CV; the former has a differentiation-like property of magnifying small current features.

A subsequent theoretical analysis of the QDL charging of MPCs in electrolyte solutions<sup>37,46</sup> was based on modeling<sup>40</sup> the MPC as a concentric sphere capacitor. The inner and outer spheres have radii  $r$  and  $r + d$ , corresponding to the MPC core radius and the core radius plus thiolate monolayer thickness  $d$ . The thiolate monolayer exerts an effective dielectric constant  $\epsilon$ . The relation for a concentric sphere capacitor is

$$C_{\text{CLU}} = A_{\text{CLU}} \frac{\epsilon \epsilon_0}{r} \frac{r + d}{d} = 4\pi \epsilon \epsilon_0 \frac{r}{d} (r + d) \quad (9)$$

where  $\epsilon_0$  is the permittivity of free space and  $A_{\text{CLU}}$  is the Au core surface area. Assuming that  $C_{\text{CLU}}$  is invariant with MPC core charge leads to a relation for the ratio of nanoparticles with core charge  $z$  to those with core charge  $z - 1$ , at a macroscopic electrode interface to which the potential  $E_{\text{APP}}$  is applied.

$$\alpha_z = \frac{N_z}{N_{z-1}} = \exp \left\{ \frac{e}{k_B T} \left[ E_{\text{APP}} - E_{\text{PZC}} - \frac{(z - 1/2)e}{C_{\text{CLU}}} \right] \right\} \quad (10)$$

$E_{\text{PZC}}$  is the potential of zero charge for the nanoparticle core. Equation 10 is Nernstian in its form, so that a QDL charging voltammetric wave shape should ideally be identical to that of a reversible one-electron redox couple, with a formal potential characteristic of the  $z/z - 1$  charge state change. The Nernstian character of stored charges on MPCs was established by observing<sup>47</sup> Nernstian shifts in equilibrium potentials of solutions prepared by mixing solutions of different, separately prepared, core charge states. Equation 10 predicts a series of identical waves, at both positive and negative potentials, in which the formal potentials of the successive  $z/z - 1$  charge state changes can be expressed as

$$E_{z,z-1}^\circ = E_{\text{PZC}} + \frac{(z - 1/2)e}{C_{\text{CLU}}} \quad (11)$$

This relation predicts a linear plot of peak potentials of a QDL voltammogram against  $z$  (the nanoparticle core charge state). Such “ $z$ -plots” require assignment of the  $E_{\text{PZC}}$  (see below) in order to define  $z = 0$ . Such assignment is not necessary to obtain average values of  $C_{\text{CLU}}$  from their slopes. The  $E_{\text{PZC}}$  of alkanethiolate-coated MPCs (a monolayer of them anchored to a surface) has been estimated<sup>48</sup> as *ca.*  $-0.2$  V vs Ag/AgCl, from a double layer capacitance minimum. (Strictly speaking, the capacitance minimum is the potential at which the diffuse layer of ions around the MPC is globally neutral).<sup>49</sup>

Seeing QDL peaks like those in Figure 4 requires nanoparticle samples in which the MPC producing the peaks is a significant fraction of the total population of different nanoparticle sizes (or different capacitances if some other aspect of the MPC besides size—such as the dielectric of the ligand monolayer—influences its capacitance). It is common in QDL voltammetry to see current peaks riding atop a substantial continuum of background current. Perfect uniformity in regard to MPC size (or capacitance) is elusive. This was in fact the case in the bulk-continuum-like voltammetry<sup>40,41</sup> discussed in Figure 3; the hexanethiolate-



coated Au MPCs samples used were sufficiently small as to potentially yield QDL current peaks but did not because of their substantial size dispersity. Voltammetric simulations<sup>45,48,50</sup> have shown that mixtures of MPCs with differing  $C_{CLU}$  values, with one of somewhat higher population, can produce voltammetry with a few clear current peaks near  $E_{PZC}$ , that fade to a continuum of current at higher charge state potentials. Methodologies that produce high purity MPCs are essential in electrochemical studies of QDL charging.

A number of further studies of quantized double layer charging voltammetry have been reported, as have been reviews.<sup>44b,c</sup> Many have concerned Au MPCs with  $\sim 29$  kDa core masses and alkanethiolate monolayers of various chain lengths. This size MPC seems to be an especially stable ("magic number") core size, although there is difficulty in being certain about its exact core shape<sup>38,52</sup> and, correspondingly, the exact number of Au atoms for the closed shell structure. That number could, for example, be 146 for a truncated decahedron<sup>51</sup> and 140 for a truncated octahedron. Further, there may be only small energy differences between one shell structure and another, so mixtures of shapes and sensitivity<sup>53</sup> to the thiolate ligand's packing and steric bulk (which can alter the ligand count) may result. The available mass spectrometry results do not resolve the issue, owing to extensive ligand and Au-loss fragmentation effects that yield low resolution spectra. Authors in the field choosing a formulaic expression of the nanoparticles while specifying a core atom number recognize its approximate nature. I will call the 29 kDa MPC simply  $Au_{140}$ , without implying exactitude between the possible core atom counts. Thermogravimetric analysis<sup>39</sup> of the organic ligand content gives, for a 140 atom core, 53 ligands (such as hexanethiolate), and the formula  $Au_{140}(SC_6)_{53}$ . The ligand count has an experimental uncertainty associated with that of the core atom count. Major advances in measurements, such as high resolution mass spectrometry of intact  $Au_{140}$  nanoparticles, are needed to resolve such uncertainties in nanoparticle formulas.

Equation 9 has been tested<sup>54</sup> for its dependence on the alkanethiolate monolayer thickness, by varying the chain length from C4 to C16 (a 4-fold variation of  $d$ ). Experimental values of  $C_{CLU}$  taken from  $z$ -plots over  $z = -2$  to  $+3$  charge states were typically within  $\pm 10\%$  of those predicted by eq 9 assuming  $d$  values for fully extended chains and an effective dielectric constant  $\epsilon = 3$  taken from measurements of the capacitances of alkanethiolate self-assembled monolayers on flat Au(111) surfaces.<sup>55</sup> A similar level of concurrence was found in  $C_{CLU}$  measurements for hexanethiolate coated  $Au_{140}$  MPCs in a variety of solvents; dielectric constants varying by a factor of 3-fold caused only  $\pm 10\%$  variation of experimental  $C_{CLU}$ . These and other<sup>56</sup> results show that eq 9 is a reasonably good estimator of MPC capacitance, in spite of the innate oversimplicity of the concentric sphere capacitor model. Unsurprisingly for such a simplistic model, it does have limitations, as discussed below.

Some additional examples of QDL voltammetry of  $Au_{140}$  MPC are shown in Figures 5 and 6. Figure 5 shows an experimental CV of a hexanethiolate-coated  $Au_{140}$  MPC that is compared<sup>57</sup> to a simulation of an ideal, reversible CV response that included a (measured) solution resistance factor. The fit to theory is good and helps to cement the conclusion drawn above regarding the essentially Nernstian character of the QDL charging phenomenon. Figure 6 shows a

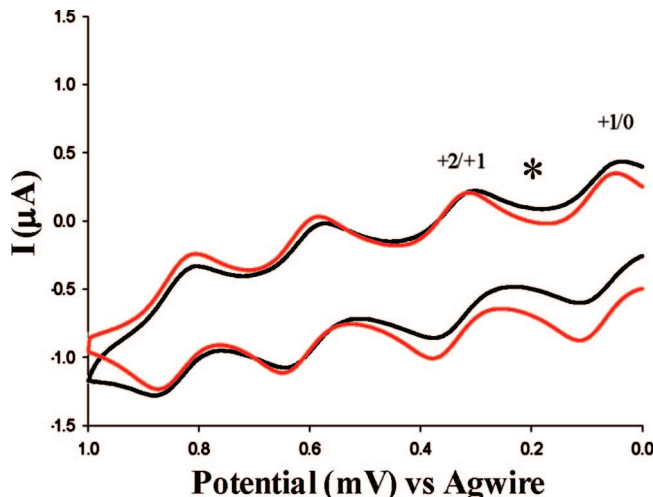


**Figure 5.** Cyclic voltammetry (50 mV/s, solid line) for the +4/+3, +3/+2, and +2/+1 charge state changes of annealed EtOH-soluble C6  $Au_{140}$  MPCs. Computer generated simulation (red line) using the DigiSim 2000 program; simulation parameters were as follows: initial potential  $-0.05$  V, switching potential  $1.0$  V, end potential  $-0.06$  V, scan rate  $0.05$  V/s, working electrode double layer capacitance  $1 \times 10^{-6}$  F, and solution uncompensated resistance  $2500 \Omega$  (measured using ac impedance with the same electrode in the same electrolyte solution), planar electrode geometry, electrode area  $0.02 \text{ cm}^2$ , MPC diffusion coefficient  $D = 3.4 \times 10^{-6} \text{ cm}^2/\text{s}$ , MPC concentration  $200 \mu\text{M}$ , reversible charge transfer. The simulated curve is offset by  $-0.25 \mu\text{A}$  to overlay the simulated and experimental curves. Reprinted with from ref 57. Copyright 2002 American Chemical Society.

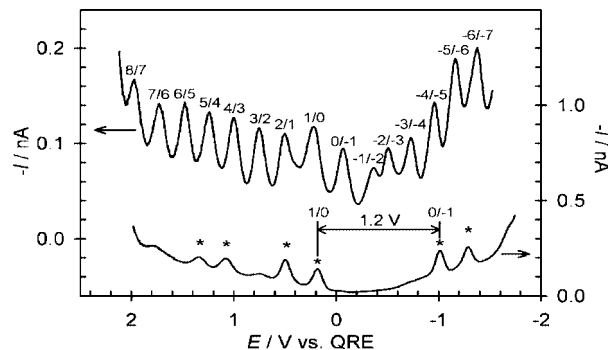


**Figure 6.** DPV responses for MPC solutions measured at a Pt microelectrode; as-prepared  $177 \mu\text{M}$  C6S- $Au_{147}$  (upper) showing 15 high-resolution QDL peaks and  $170 \mu\text{M}$  C6S- $Au_{38}$  (lower) showing a HOMO-LUMO gap. It can be seen that the as-prepared solution contains a residual fraction of  $Au_{38}$  that smears out the charging response at potentials where QDL peaks overlap. The electrode potential is scanned negative to positive. Reprinted with permission from ref 58. Copyright 2003 American Chemical Society.

voltammogram<sup>58</sup> reported by Quinn that exhibits 15 distinct current peaks for hexanethiolate-coated  $Au_{140}$  MPCs. It appears that the number of observable QDL current peaks may be limited only by the available electrochemical potential window and the width of the peaks. The Figure 6 voltammogram shows an average peak-to-peak spacing of about  $0.25$  V, corresponding to a nanoparticle capacitance  $C_{CLU} = 0.64$ , a value close to that found<sup>57</sup> ( $0.60$  aF) from the peak spacing in Figure 5. QDL voltammetry nearly as spectacular (in terms of numbers of peaks) was reported by Maran<sup>59</sup> for  $Au_{140}$  coated with a different ligand, phenylethanethiolate, where the potential spacing was slightly smaller ( $\Delta V = 0.22$ ) and the capacitance  $C_{CLU}$  ( $0.70$  aF) slightly larger.

One assumption of eq 9 is that  $C_{\text{CLU}}$  does not change with MPC charge state or with the solvent. The possible consequences of this assumption were discussed early in its exploration,<sup>54</sup> and indeed deviations from the predicted uniform spacing between current peaks have been reported. Peak spacing often decreases<sup>58,60</sup> and can be somewhat irregular at higher charge states.<sup>41,57</sup> Peak spacing can be very sensitive to solvent<sup>60–63</sup> and electrolyte,<sup>60,64</sup> it was for example<sup>60</sup> increased by 20% by introduction of the hydrocarbon dodecane into  $\text{CH}_2\text{Cl}_2$ , relative to  $\text{CH}_2\text{Cl}_2$  alone.

The sensitivity of QDL peak spacing to solvent and electrolyte is substantially related to the permeability of the MPC monolayer. The organothiolate ligands of self-assembled monolayers on flat Au(111) surfaces are tightly ordered; those on highly curved MPC surfaces necessarily have increasing spaces between them at distances further from the Au–S bonding interface. This radial effect on ligand density means that the MPC monolayer may be permeated by solvent (and potentially electrolyte ions), which consequently alter its effective dielectric ( $\epsilon$ ) constant and thickness; such permeation may further depend on the MPC core charge.<sup>60,65</sup> Taylor dispersion measurements<sup>66</sup> of MPC diffusivity suggest, in fact, that the termini of alkanethiolate chains are free-draining of solvent. There have been several subsequent theoretical (Poisson–Boltzmann solutions) assessments, by Quinn,<sup>58</sup> Girault,<sup>63</sup> and Mafe,<sup>67</sup> that usefully model penetration of the MPC monolayer to solvent and electrolyte ions, and provide an improved framework of the concentric sphere model. The latter is a very instructive report<sup>67</sup> that highlights the various complexities of the permeation problem and assesses previous work regarding monolayer permeability.

Another of the peak spacing effects reflects a fundamental feature common to all electrical double layer phenomena. Spacings between peaks immediately adjacent to zero charge of the MPC ( $z = 0$ ) are observed<sup>58,60,64</sup> to pass through a small maximum. This is anticipated, in fact, from the potential dependency of the diffuse double layer component of the nanoparticle double layer capacitance. Diffuse layer effects are explicitly neglected<sup>54</sup> in eq 9. Quinn<sup>58</sup> correctly recognized the importance of treating the radial dispersion of the diffuse layer ionic space charge and presented calculations from the Poisson–Boltzmann equation in radial coordinates. The calculation reasonably well simulated the small changes in peak spacing in Figure 6. Guo et al.<sup>60</sup> extended examination of the diffuse layer contribution by observing QDL voltammetry as a function of electrolyte concentration and comparing current peak spacings to radial calculations. Peak spacing near  $z = 0$  increased as electrolyte concentration was decreased, as seen in Figure 7. Example values extracted for compact and diffuse layer capacitances are shown in the figure legend; those for  $C_{\text{DIFFUSE}}$  are  $\gg C_{\text{COMPACT}}$  even at 1 mM electrolyte concentration. Remembering that the overall double layer capacitance ( $C_{\text{MPC}}^{-1}$ ) is obtained by summing the reciprocals of  $C_{\text{DIFFUSE}}$  and  $C_{\text{COMPACT}}$ , the diffuse layer capacitance—while detectable—is a relatively minor contributor to the nanoparticle double layer. Deviations from eq 9 caused by permeation of solvent and electrolyte into the MPC monolayer are larger.

An extreme example of solvent-induced change in  $C_{\text{CLU}}$  occurs when a monolayer (or multilayer film) of an organic-soluble, water-insoluble MPC is attached to (or cast upon) an electrode that is then used in an aqueous electrolyte.<sup>61,68–71</sup> QDL peaks are seen (Figure 8) in the differential pulse

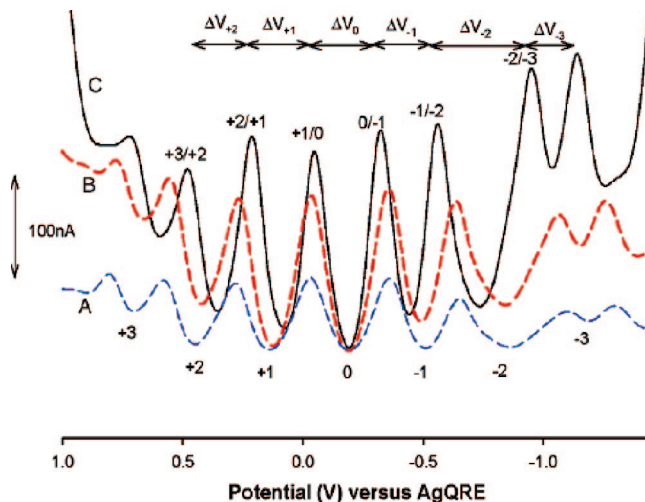


**Figure 7.** Osteryoung square wave voltammetry of 0.08 mM  $\text{Au}_{140}(\text{SC6})_{53}$  (SC6 stands for hexanethiolate) in  $\text{CH}_2\text{Cl}_2$  at 283 K with the  $\text{Bu}_4\text{NClO}_4$  concentrations (A) 0.74, (B) 1.02, and (C) 100 mM at 283 K. The voltammograms have been adjusted to a common  $E_{\text{PZC}}$  potential versus Ag/AgCl;  $E_{\text{PZC}}$  is about  $-0.2$  V vs Ag/AgCl. Estimated sample monodispersity is about 43%. Values of capacitance from analysis of these data are (A) 1 mM,  $C_{\text{CLU}} = 0.50$ ,  $C_{\text{DIFFUSE}} = 2.4$ , and  $C_{\text{COMPACT}} = 0.63$  aF; (C) 100 mM,  $C_{\text{CLU}} = 0.59$ ,  $C_{\text{DIFFUSE}} = 9.9$ , and  $C_{\text{COMPACT}} = 0.63$  aF. Reprinted with permission from ref 60. Copyright 2005 American Chemical Society.

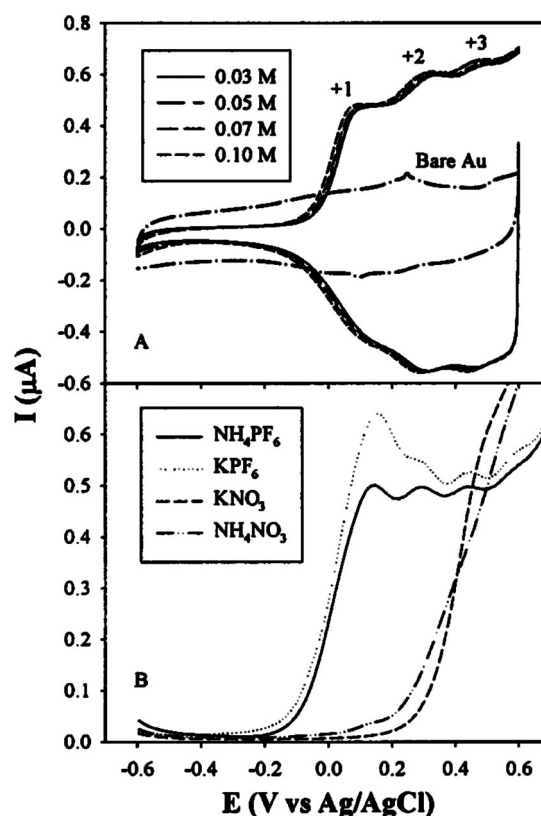


**Figure 8.** (A) CVs of a C6 Au MPC-modified Au electrode in aqueous  $\text{NH}_4\text{PF}_6$  solutions of various concentrations. Also shown is the CV of the same bare electrode in 0.1 M  $\text{NH}_4\text{PF}_6$ . Electrode area  $1.1 \text{ mm}^2$ . Sweep rate 100 mV/s. (B) DPVs of the same MPC-modified electrode in various electrolyte solutions (0.1 M). Pulse amplitude 50 mV, dc ramp 4 mV/s. Reprinted with permission from ref 61. Copyright 2000 American Chemical.

voltammetry only for positive core charge states and for  $\text{PF}_6^-$  but not  $\text{NO}_3^-$  electrolyte. Currents at potentials where the



MPC core would become charged negatively are small and featureless. The phenomenon was termed ion rectification. The potential at which the positive-charging QDL peaks appeared depends on the electrolyte anion; this onset potential effect was attributed<sup>70,71a</sup> to the preferred ion-pairing of more hydrophobic anions such as  $\text{PF}_6^-$  with an electrochemically positively charged but hydrophobic MPC. In a subsequent study, Quinn et al.<sup>72</sup> argued later that the MPC film/aqueous boundary should be regarded as a hydrophobic/aqueous liquid-like/liquid interface across which there is an ion transfer potential  $\Delta_{\text{w}}^{\text{film}}\varphi$  reflecting the relative ion solvation in the two phases and that this potential is the source of the observed changes in onset potential. In this model, the current for oxidation of the MPC film would be ion limited rather than ion rectified.

Albrecht et al.<sup>73</sup> have extended the STM spectroscopy experiment<sup>44</sup> shown in Figure 4A to electrochemical STM spectroscopy of  $\text{Au}_{146}$  MPC tethered to a Pt(111) surface by 4-mercaptopyridine ligands. Conducted in aqueous electrolyte, the STM spectroscopy peaks mirrored those seen in the above rectification voltammetry phenomenon, but with a smaller peak spacing. The interpretation suggested the importance of an interplay between reorganization free energy for electron transfers and the Coulombic charging energy responsible for the QDL.

The QDL voltammetry studies discussed above were conducted on  $\text{Au}_{140}$  (1.6 nm diameter core) MPCs. Reports of QDL for other thiolated Au nanoparticle dimensions include those with 1.4 nm (phosphine functionalized),<sup>74</sup> 2.0 nm ( $\sim\text{Au}_{225}$ ),<sup>67,75,76</sup> 2.2 nm ( $\sim\text{Au}_{314}$ ),<sup>77</sup> and 3.7 nm ( $\sim\text{Au}_{1415}$ )<sup>78a,b</sup> diameter cores. (The 3.7 nm MPC report<sup>78a,b</sup> and one for 5 nm  $\text{Rh}$ <sup>78c</sup> possibly reflect artifacts<sup>77</sup> of digitally controlled current sampling). The multiple, roughly evenly spaced current peaks that are characteristic of QDL voltammetry have also been seen for Cu,<sup>79</sup> Ag,<sup>80a,b</sup> and Pd<sup>79,80c</sup> MPCs, and in the case of Pd, for  $\sim\text{Pd}_{40}$ ,  $\sim\text{Pd}_{80}$ , and  $\text{Pd}_{140}$ .<sup>76</sup> Most of these MPC materials were prepared by the Brust reaction. The phosphine functionalized 1.4 nm Au MPCs are commercially available and were used<sup>74</sup> in a novel experiment in which they were coupled to the electrode, and then hydrophobically capped magnetic nanoparticles were used to generate a low dielectric (toluene) film over them. QDL responses could be observed that vanished when the magnetic nanoparticles were released by an external field, dispersing the toluene film. Other magnetic effects could be seen in magnetoelectrochemical experiments in which imposed fields influenced transport rates both in QDL<sup>81a</sup> and redox-labeled<sup>81b</sup> MPC voltammetry. Notable exceptions were Pd and Au nanoparticles prepared within dendrimers<sup>76</sup> and then extracted with hexanethiol; useful QDL voltammetry was obtained without further purification of the MPCs. The dendrimer preparation route is quite promising. In general, the stability and ease of preparation of appropriate size and purity Au nanoparticles that are protected by low dielectric ligand monolayers have produced much better defined QDL voltammetry than has been achieved when using other metals for the MPC core.

### 3.3. Voltammetry of Molecule-like Nanoparticles

The emergence of molecularity in the metal-to-molecule transition is signaled by the emergence of an energy gap, which may be detected optically or electrochemically or both. The optical energy gap for a nanoparticle is the electronic band edge or absorbance spectrum onset for transitions from

the HOMO (highest occupied molecular orbital) to the LUMO (lowest unoccupied molecular orbital). Optical absorbance band edges are detectable when they occur in the near-infrared region or at higher energies, i.e., above  $\sim 1$  eV. Optical energy gaps can have energies greater than those detectable electrochemically (owing to the available electrochemical potential window). The electrochemical energy gap is a difference (which is larger than the QDL charging energy) between electrochemical potentials for the first oxidation and first reduction wave for a parent species. Electrochemical energy gaps are detectable at lower energies than are usually feasible optically, and so they are useful estimators of small HOMO–LUMO energy gaps, provided that a reasonable correction can be made for charging energy.<sup>82</sup> As noted above, charging energy (or Born charging energy) is the voltage increment associated with generating, in the solvent medium employed, positive and negative species from a neutral one or with increasing the charge on already charged species. Its value can be expected to be roughly approximated by the spacing of potentials between QDL peaks. Optical HOMO–LUMO electronic excitation is not accompanied by a change in overall charge, and no charging energy correction is required. Uncertainties in values of the HOMO–LUMO energy gap are, for optical measurements, associated with measuring the energy for extinction of optical absorbance and, for electrochemical measurements, associated with estimating the charging energy correction.

In the case of Au MPCs smaller than those exhibiting quantized double layer charging voltammetry, where there is already an electrostatically based potential spacing between one-electron voltammetric peaks (eq 9), appearance of a HOMO–LUMO energy gap would produce an enlarged potential spacing between the current peaks for the first one-electron loss and the first one-electron gain of the parent or “native” (usually, but not necessarily,  $z = 0$ ) nanoparticle. Subtracting the QDL potential spacing (as an estimate of the charging energy) gives the electrochemically estimated HOMO–LUMO gap energy.

Within the family of Au nanoparticles protected by organothiolate ligands (MPCs), electrochemical energy gaps, and/or optical HOMO–LUMO energy gaps, have been detected for MPCs designated as having core sizes of  $\sim\text{Au}_{75}$  (or 14 kDa),<sup>83,84</sup>  $\sim\text{Au}_{55}$ ,<sup>85</sup>  $\text{Au}_{38}$ ,<sup>58</sup>  $\text{Au}_{25}$ ,<sup>86–88</sup> and  $\text{Au}_{13}$ .<sup>89</sup> This progress toward defining the metal-to-molecule transition (for Au nanoparticles with organothiolate ligands) is summarized in Figure 9 as three regimes of nanoparticle behavior, from bulk continuum at the left ( $\text{Au}_x$ ), where no voltammetric features are observable, to quantized double layer charging for  $\text{Au}_{225}$  and  $\text{Au}_{140}$ , to molecule-like on the right, for  $\text{Au}_{75}$ ,  $\text{Au}_{55}$ ,  $\text{Au}_{38}$ ,  $\text{Au}_{25}$ , and  $\text{Au}_{13}$ . The diverging lines represent the relative electrochemical potentials for the  $\text{MPC}^{+1/0}$  and  $\text{MPC}^{0/-1}$  reactions (these charge state designations assume that  $z = 0$  for the parent MPC;  $\text{Au}_{25}$  is a known exception, *vide infra*). The diverging lines drawn in the cartoon emphasize that, for the smaller nanoparticles where a HOMO–LUMO gap is developing, the gap between those potentials widens at a faster pace (than in the QDL region) with decreasing MPC core size. Available gap energy data are shown in blue at the upper right. It is somewhat remarkable that the  $\sim\text{Au}_{140}$  nanoparticle, with core diameter *ca.* 1.6 nm, exhibits no detectable HOMO–LUMO gap whereas the HOMO–LUMO gap has grown to a considerable 1.3 eV energy for the  $\sim\text{Au}_{25}$  nanoparticle, with a *ca.* 1

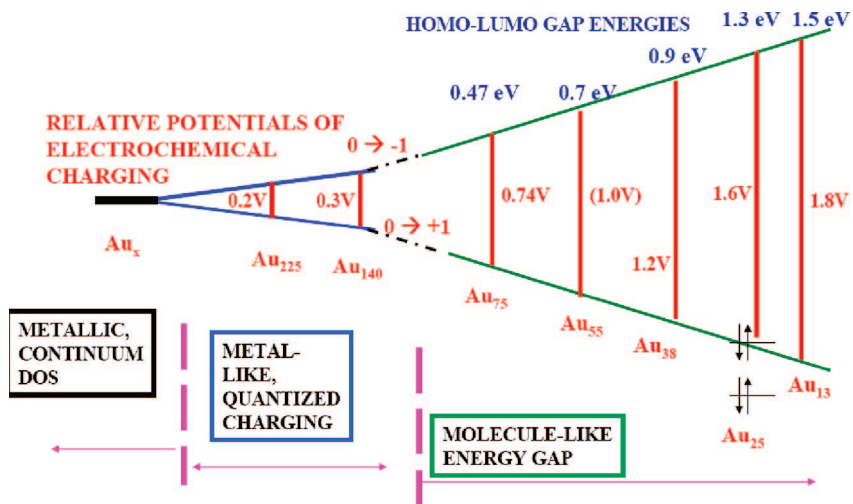


**Figure 9.** Summary of electrochemical behavior by MPC core size, showing estimated energy gaps (HOMO–LUMO gaps) and electrochemical energy gaps (which is the spacing between the first oxidation peak and the first reduction current peak for the native nanoparticle). Data for electrochemical energy gaps are as follows: for  $\text{Au}_{xx}$ ,  $xx = 225$  from refs 75, 80, and 83;  $xx = 140$  from refs 57 and 83;  $xx = 75$  from refs 83 and 84;  $xx = 55$  from refs 83 and estimate from homo–lumo datum;  $xx = 38$  from refs 58 and 83;  $xx = 25$  from refs 86;  $xx = 13$  from refs 89.

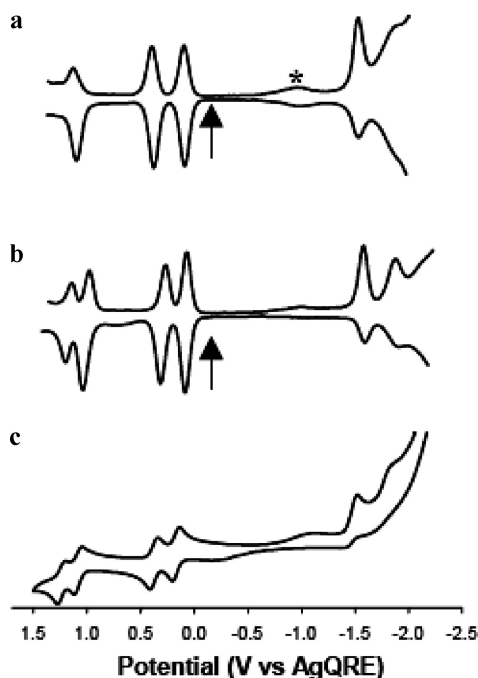


**Figure 10.** (a) 25 °C and (b) –70 °C differential pulse voltammograms (DPVs) at 0.02 V/s, and (c) –70 °C cyclic voltammogram (0.1 V/s) of  $\text{Au}_{25}(\text{PhC}_2\text{S})_{18}$  (corrected from  $\text{Au}_{38}(\text{PhC}_2\text{S})_{24}$  in ref 88) in 0.1 M  $\text{Bu}_4\text{NPF}_6$  in degassed  $\text{CH}_2\text{Cl}_2$  at a 0.4 mm-diameter Pt working electrode, a Ag wire quasireference (AgQRE) electrode, and a Pt wire counterelectrode. Arrows indicate solution rest potentials and \* indicates the wave for incompletely removed  $\text{O}_2$ , which varied from experiment to experiment. Reprinted with permission from ref 86. Copyright 2004 American Chemical Society.

nm diameter core. The metal-to-molecule transition for Au nanoparticles is very steep.

The electrochemical energy gap data in Figure 9 are taken from voltammetry<sup>86</sup> such as that in Figure 10 for the nanoparticle  $\text{Au}_{25}(\text{SCH}_2\text{CH}_2\text{Ph})_{18}$ . This nanoparticle is analogous to  $\text{Au}_{140}$  in that it seems to have a higher level of stability than neighboring core sizes.<sup>90</sup> The first oxidation and first reduction waves of the native nanoparticle lie at +0.1 V and –1.5 V vs the Ag quasireference electrode; the 1.62 V separation between them corresponds to the electro-

chemical energy gap for this MPC. The other electrochemical gap energies shown in Figure 9 were obtained in a similar manner. These data, as noted above, contain a charging energy term.

Recent experiments<sup>36c,91</sup> show that the native  $\text{Au}_{25}(\text{SCH}_2\text{CH}_2\text{Ph})_{18}$  nanoparticle has an intrinsic charge of –1. (The nanoparticle would otherwise have an odd electron count). That the HOMO of this MPC is doubly occupied is indicated by the doublet of oxidation peaks starting at *ca.* +0.1 V in Figure 10; the first electron transfer from the HOMO is followed by a second step at 0.29 V more positive (in  $\text{CH}_2\text{Cl}_2$  solvent). The two waves in Figure 10 then are for the  $\text{Au}_{25}^{0/-1}$  and  $\text{Au}_{25}^{+1/0}$  couples, and the nanoparticle “PZC” lies in between, at the potential at which the interfacial solution contains primarily  $\text{Au}_{25}^0$ . The 0.29 V voltage spacing is similar in magnitude to those in the QDL charging described above, i.e., of magnitude appropriate for a charging energy term. Thus, the electrochemically derived estimate of the  $\text{Au}_{25}^-$  MPC’s HOMO–LUMO gap energy is 1.33 V. Measurement of the optical absorbance edge for this MPC gave an extinction of absorbance at 930 nm, or 1.33 eV, for the optical HOMO–LUMO gap energy, in good agreement with the electrochemical estimate. Such good agreement is not always seen; in other solvents and with other thiolate ligands,<sup>86</sup> there were fluctuations of about 0.05 eV in the derived gap energy, apparently from variations in the charging energy term.

It must be noted that the MPC giving the voltammetry in Figure 10 was regrettably initially misidentified<sup>86</sup> as having a  $\sim\text{Au}_{38}$  core, substantially originating from the limitations of TEM diameter measurements at such a small size. This labeling error was propagated through several subsequent papers<sup>92–97</sup> on various aspects of the electrochemistry of this species. Subsequent, *definitive* high resolution mass spectrometry (electrospray<sup>88,91c</sup> and MALDI<sup>91</sup>) results have shown that MPCs prepared and fractionated by the protocols used in the earlier publication<sup>86</sup> actually produce mixtures of the two MPCs, with the  $\text{Au}_{38}$  MPC as a minor constituent. The composition of the  $\text{Au}_{25}$  MPC, now complemented by a recent X-ray crystallographic structure determination,<sup>36c</sup> was unequivocally established<sup>88,91c</sup> as  $\text{Au}_{25}(\text{SCH}_2\text{CH}_2\text{Ph})_{18}^-$ .

The  $\text{Au}_{25}\text{L}_{18}$  composition was also identified by Tsukuda et al.,<sup>99</sup> where  $\text{L}$  = glutathione, a different ligand.

Other aspects of the molecule-like MPC voltammetry seen in Figure 10 are that the doublet of oxidation peaks ( $\text{Au}_{25}^{0/1-}$  and  $\text{Au}_{25}^{+1/0}$ ) is followed, at somewhat more positive potential, by a second doublet of current peaks. This is a typical pattern for electron transfer reactions of molecular species and was proposed<sup>86</sup> for the  $\text{Au}_{25}$  nanoparticle to reflect the presence of two well-defined molecular orbitals, each doubly occupied with an electron pair. (This analysis of the voltammetry of the  $\text{Au}_{25}$  MPC differs from a recent theoretical study<sup>100</sup> that predicts changes in spin multiplicity with core charge and localization of the electronic charge on an inner,  $\text{Au}_7$  core of the nanoparticle). The same pattern, a doublet of oxidation steps, is also seen in the voltammetry of  $\text{Au}_{38}$ <sup>58</sup> and  $\text{Au}_{75}$ .<sup>84</sup> At negative potentials, multiple electron transfer steps are seen, but there is difficulty in making detailed measurements there, since the negatively charged nanoparticles are not very stable and sometimes the reverse voltammetric scan shows an attenuated wave (see Figure 10c, for example). Maran<sup>97</sup> has shown that, in DMF solvent, decomposition of a reduced MPC (the reduced form labeled as  $\text{Au}_{38}^-$  but probably  $\text{Au}_{25}^{2-}$ ) occurs by thiolate ligand dissociation.

There is limited literature on molecule-like nanoparticle electrochemistry other than the thiolate-stabilized Au family summarized in Figure 9. Crooks has learned<sup>31,101</sup> to prepare metal nanoparticles by sequestering and reducing metal ions within dendrimers (these include  $\text{AuAg}$ ,<sup>102</sup>  $\text{Ni}$ ,<sup>103</sup>  $\text{Pd}$ ,<sup>104</sup> core/shell  $\text{Pd/Au}$ ,<sup>105</sup>  $\text{Pt}$ ,<sup>101</sup> and  $\text{PtPd}$ <sup>106</sup>) and to extract<sup>102,103,107,108</sup> them from within the dendrimers (they are electrochemically silent in that state) by thiolate coordination. Both Au and Pd nanoparticles have been thusly produced and their voltammetry described.<sup>76</sup> As mentioned above, QDL voltammetry was obtained for both Au and Pd hexanethiolate-coated MPCs, and the charging properties observed for  $\text{Au}_{140}$ ,  $\text{Au}_{225}$ , and  $\text{Pd}_{140}$  MPCs were consistent with other reports based on MPCs made by the Brust reaction. A surprising observation noted<sup>76</sup> was that the dendrimer preparation of nominally  $\sim\text{Pd}_{40}$  and  $\sim\text{Pd}_{80}$  hexanethiolate-coated MPCs gave voltammetry with current peaks spaced apart by  $\Delta V$  values appropriate according to eq 9 for this core size but lacking of any electrochemical energy gap. This is an intriguing, as yet unresolved, result.

Does the thiolate ligand of the MPC's core-protecting monolayer influence its electrochemistry? The descriptor "monolayer-protected clusters" implies that the thiolate monolayer simply stabilizes the Au cores against aggregation, which is the general case for other metal colloids. There are, however, at least two aspects of the MPC thiolate monolayer that provide a more chemically specific ligand influence on MPC electrochemistry. In the preceding, the ligand's effective dielectric constant appears in the concentric sphere (eq 9) estimate of the MPC charging properties. If the ligand's dielectric constant is too large, then QDL charging would not be seen, since  $\Delta V$  would be depressed. A factor of 6-fold would decrease the ca. 0.25 V  $\Delta V$  of Figure 6<sup>58</sup> to 40 mV, which would place any QDL observation at the margin of being obscured by thermal broadening. This, at least in part, is apparently responsible for the absence of QDL charging voltammetry in studies of MPCs with highly polar ligands.<sup>109,110</sup>

A second way in which thiolate ligands can matter in MPC electrochemistry of molecule-like MPCs is that their defined molecular orbitals may be susceptible to, for example,

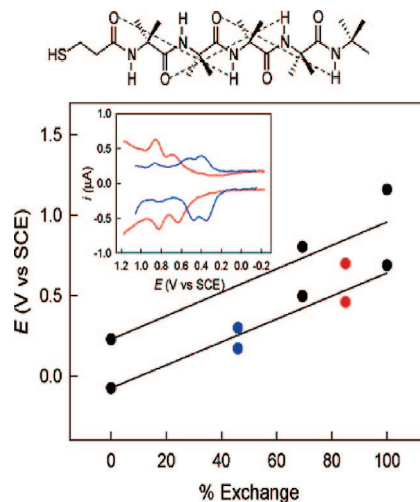


**Figure 11.** DPV potentials of the first (lower plot) and second (upper plot) oxidation processes of  $\text{Au}_{38}$  clusters exchanged with the thiolated  $\alpha$ -aminoisobutyric acid peptide shown, as a function of the percent of the peptide in the monolayer. The lines are first order fits to the data and are meant to underline the trend. The inset shows the DPV traces of the first two oxidation peaks of two samples (blue circle, 46%; red circle, 85%), as obtained at 0.5 mM concentration in  $\text{DCM}/0.1 \text{ M Bu}_4\text{NPF}_6$ . Reprinted with permission from ref 59. Copyright 2006 American Chemical Society.

electron inductive or dipolar effects of attached thiolate ligands. This has indeed been demonstrated. Homo-oligomers of the  $R$ -aminoisobutyric acid unit form stiff helices that generate a substantial dipole moment along the helical axis. Thiolated versions of such peptides<sup>111</sup> exchanged into the monolayers of a nanoparticle with composition assigned as  $\text{Au}_{38}(\text{SC}_2\text{Ph})_{24}$  produce substantial (as much as 0.7 to 0.8 V) positive shifts in the first and second oxidation (HOMO level) waves of this MPC.<sup>59</sup> The extent of the potential shifts depended on the number of thiolated peptide ligands exchanged into the MPC monolayer, as shown in Figure 11. Another example<sup>94</sup> was based on exchanging the ligands (all of them, verified by  $^1\text{H}$  NMR) of the  $\text{Au}_{25}(\text{SCH}_2\text{CH}_2\text{Ph})_{18}$  nanoparticle with five different  $p$ -substituted thiophenols, where the substituents varied from the electron withdrawing  $-\text{NO}_2$  to the relatively electron donating  $-\text{OCH}_3$  substituent. Analogous to the result in Figure 11, a systematic shift of the voltammetric formal potentials toward more positive values—as much as 0.45 V—occurred with increasingly electron-withdrawing substituents. The shift of the HOMO (first oxidation wave) and LUMO (first reduction wave) were approximately equal, so that the electrochemical energy gap remained substantially unchanged. These reports show that the MPC ligand shells of very small nanoparticles can measurably influence the core—electronic energy levels, which is a distinctly molecule-like characteristic.

The recent crystal structures<sup>36b,c</sup> of  $\text{Au}_{102}$  and  $\text{Au}_{25}$  offer additional insights into our view of the thiolate ligands as being a "monolayer" shell around a Au nanocrystal core, analogous to a self-assembled monolayer on a flat Au surface. This picture may ultimately prove to be too simplistic, since the recent results reveal a ligand shell with a more complex Au—SR bonding motif, bound to a nanocrystal core.

Finally, a semantics issue should be mentioned—what kind of nanoparticle should be called a quantum dot? Quantum dot is a common descriptor in the semiconductor nanoparticle literature,<sup>112</sup> where it normally connotes a property—such as band gap—that discernibly changes with the nanoparticle size. This writer has been accosted in the past by a reviewer



that the term is reserved for semiconductor nanoparticles. A variety of size-dependent properties has now been detected for metal nanoparticles, such as the QDL charging size and protecting monolayer dependence, the emergence of demonstrable HOMO–LUMO gaps, and the metal–insulator transition. The term quantum dot, in my opinion, is quite appropriately applied to metal nanoparticles that have size dependent properties.

### 3.4. Electron Transfer Chemistry of Nanoparticle Solutions

The rates of electron transfers of Au nanoparticle MPCs have been investigated in solutions of MPCs,<sup>97,113,114a,115</sup> at liquid/liquid interfaces,<sup>92,113</sup> and in room temperature molten salts containing MPCs.<sup>95,116</sup> The ionic conductivities of MPC-containing molten salts have also been investigated,<sup>117,118</sup> as has the electrolysis of MPCs (or by chemical reactions) to various states of MPC core charge that can be stored,<sup>47,79,96,119</sup> used for further electron transfer reactions,<sup>117</sup> or used in investigation of the effects of charging the MPC cores on their properties.<sup>96,117,120–122</sup>

The traditional approaches<sup>37</sup> to measuring rates of electrochemical reactions involve—for moderately fast one-electron reactions and in order to defeat the competition between electron transfer and mass transfer rate control of the current—the use of very short observation times or very small distances. These are tactics that accelerate mass transfer rates and bias the experimental responses toward electron transfer rate control. The ideas of Marcus theory<sup>123</sup> suggest that electron transfer reactions might be rather fast for a rather large entity (the MPC core) in a low dielectric medium (its hydrophobic, low-dielectric thiolate monolayer). Assuming that the electron transfer activation barriers for electron transfers of MPCs may be “outer-sphere” thus guides the selection of methods that one might wish to apply to heterogeneous electron transfer rate measurements for MPCs. Additionally, the problem of preparing a sufficiently monodisperse (or at least not highly polydisperse) MPC sample is one not commonly encountered in studies of simpler molecular species.

Most electrochemical electron transfer rate observations on dissolved MPCs<sup>92,113,114a</sup> have relied on feedback approach curves from scanning electrochemical microscopy<sup>114b</sup> (SECM). Reports by Quinn<sup>113</sup> and Cliffel<sup>114a</sup> highlight this approach in studies of alkanethiolate-protected  $\sim\text{Au}_{140}$  MPCs. The general idea of the SECM feedback method is shown in Figure 12, where the charge state of the MPC is cycled between a microelectrode and a flat substrate electrode. Controlled at potentials relative to a reference electrode elsewhere in the solution, one electrode is made to be an electron donor to the MPC and the other electrode an electron acceptor. Allowing the microelectrode to move and more closely approach the substrate electrode increases the mass transport flux (inversely with intervening distance) and biases the current toward control by the electron transfer rates between the MPC and the electrode (as opposed to MPC diffusion rates). One compares theoretical and experimental “approach curves” (current vs distance between the two electrodes) for pure mass transport and for mixed mass transport/electron transfer current control. When using 10  $\mu\text{m}$  diameter microelectrodes,<sup>113,114a</sup> the approach curve currents did not show a discernible electron transfer kinetic component. When, on the other hand, the effective mass transport rate was accelerated by choosing a smaller (5  $\mu\text{m}$ )

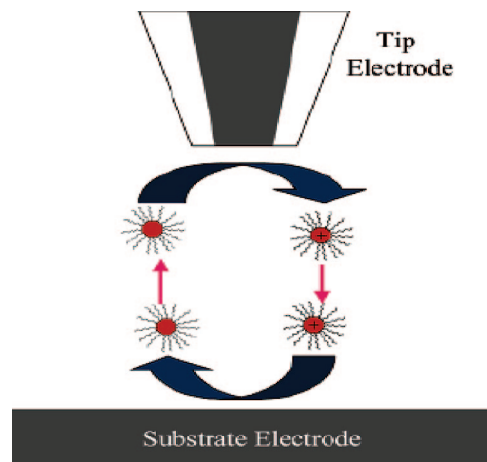
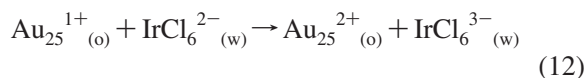


**Figure 12.** Mass-transfer and kinetic transfer limiting processes. The diffusion of the species through the bulk solution to the electrode is the mass-transfer limited process while the movement of the electron from the electrode to the species is the kinetically limited process. Reprinted with permission from ref 114a. Copyright 2006 American Chemical Society.

microelectrode,<sup>114a</sup> partial electron transfer rate control was attained and the rate constant was assessed as 0.11 cm/s. The rate decreased for MPCs with longer chain length monolayers, but the samples were insufficiently monodisperse to decipher the electronic coupling factor of the tunneling rate versus monolayer thickness relation.

Another recent electron transfer rate measurement has been reported<sup>97</sup> for MPCs labeled as  $\text{Au}_{38}$  (but probably  $\text{Au}_{25}$ ), based on digital simulations of the voltammograms and the traditional Nicholson cyclic voltammetry method,<sup>124</sup> which uses the relation between potential sweep rate and  $\Delta E_{\text{PEAK}}$  values. A rate constant of  $k^{\circ}_{\text{HET}} = 0.1$  cm/s and an activation barrier energy of  $\Delta G_0^{\ddagger} = 5.2$  kcal/mol ( $\sim 22$  kJ/mol) were assessed for the nanoparticle electrode reaction. The authors concluded that the electron transfer rate might be slowed by an inner sphere barrier term associated with changes in Au–S bond lengths, which had also been suggested from solid state electron hopping data<sup>96</sup> (where a 20 kJ/mol activation barrier was observed) and has been since supported by observations of differences in Au–S Raman bond stretch energies between different nanoparticle charge states.<sup>125</sup>

SECM measurements have also been directed at the liquid–liquid interface, where the MPC is a solute in one phase and a chosen electron transfer couple in the other. This method relies on the scheme illustrated in Figure 13. The first attempt in this direction<sup>113</sup> used  $\sim\text{Au}_{140}$  MPCs and encountered very slow apparent reaction rates between the MPCs—dissolved in dichloroethane (DCE)—at its interface with a variety of aqueous redox couples. A subsequent study<sup>92</sup> using  $\text{Au}_{25}(\text{SC}_2\text{Ph})_{18}$  MPCs (earlier misidentified as  $\text{Au}_{38}$  MPCs, as noted above) was reported of the (water/DCE) interfacial reaction



The  $\text{Au}_{25}^{1+}$  nanoparticle (now known to actually be  $\text{Au}_{25}^0$  based on the recent charge state results<sup>91</sup>) was prepared by the propensity of the native  $\text{Au}_{25}^{-}$  state to become oxidized when passed through a silica gel column. Figure 14 shows liquid–liquid approach curves under several different conditions—in curve 1 there was no MPC in the DCE phase, and the liquid interface simply acts as a diffusion-field

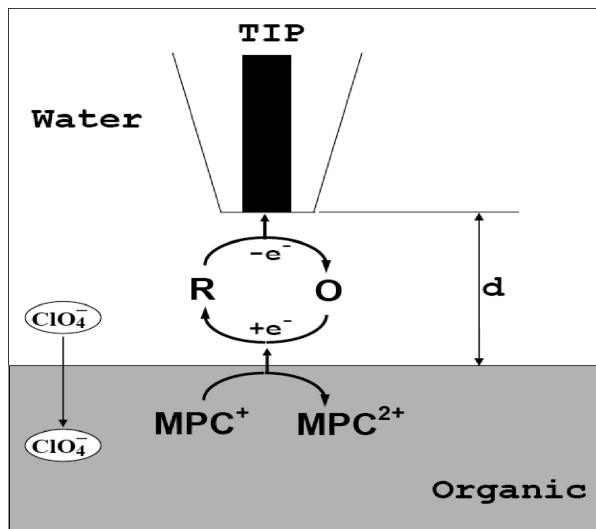


**Figure 13.** Schematic diagram of SECM approach measurement of the ET rate between an organic-soluble MPC and an aqueous redox species. Electroneutrality is maintained by transfer of perchlorate ions across the interface. Reprinted with permission from ref 92. Copyright 2004 American Chemical Society.

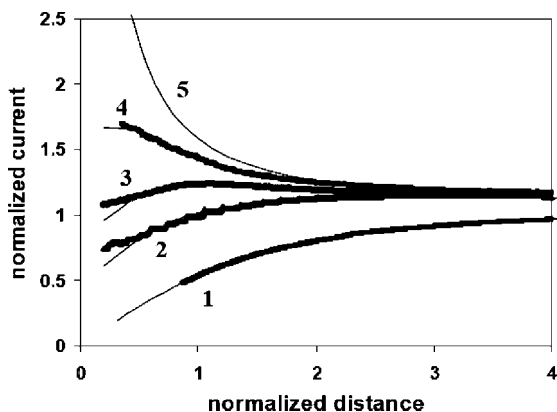


**Figure 14.** SECM current–distance curves for a 12.5  $\mu\text{m}$  radius Pt tip in aqueous solution approaching the water/dichloroethane (DCE) interface. Currents are normalized to  $i_{T,\infty}$  and distance to tip electrode radius. The aqueous solution contained 0.1 M  $\text{NaClO}_4$  and (1) 0.5, (2) 0.32, (3) 0.145, or (4) 0.057 mM  $\text{Na}_3\text{IrCl}_6$ . DCE contained 0.01 M  $\text{Hx}_4\text{NClO}_4$  and 0.4 mM MPC (curves 2–4). The tip potential was held at 0.8 V vs  $\text{Ag}/\text{AgCl}$ , corresponding to the plateau current for oxidation of  $\text{IrCl}_6^{3-}$ . The tip was approached at 1  $\mu\text{m}/\text{s}$ . Solid lines are as follows: theory for pure negative feedback (curve 1), simulated curves for finite heterogeneous kinetics (curves 2–4), and theory for a diffusion-controlled process (curve 5). Reprinted with permission from ref 92. Copyright 2004 American Chemical Society.

shielding barrier (so-called “negative feedback”) to the tip-generated  $\text{IrCl}_6^{2-}$  oxidant. Curve 5 corresponds to a calculated diffusion-controlled rate of reaction 12, whereas curves 2–4 are for different combinations of the MPC and  $\text{IrCl}_6^{3-}$  concentrations. The theoretical curves fitted to experimental curves 2–4 correspond to a rate constant of  $k = 76 \text{ M}^{-1} \text{ cm s}^{-1}$ . This reaction rate is faster than that of other known redox reactant pairs having comparable reaction driving energies, which for reaction 12 was 0.31 V. As expected, use of  $\text{Fe}(\text{CN})_6^{3-}$  as oxidant produced only mass transport controlled currents; its reaction with the MPC is uphill ( $\Delta E_{1/2} = -0.15 \text{ V}$ ) and was expected to be very slow.

NMR line-broadening is yet another method useful for electron transfer rate measurements, for example in studies by Weaver<sup>126,127</sup> of solvent dynamics effects on ferrocene<sup>+1/0</sup>

self-exchanges. The broadening of NMR resonances relies on exchanges occurring with a frequency comparable to the frequency difference in chemical shifts between the oxidized and reduced forms of the redox couple. This method, when applied to the  $\text{Au}_{25}^{0/1-}$  nanoparticle couple, has produced a preliminary  $T_{300\text{K}}$  rate constant<sup>115</sup> of  $\sim 3 \times 10^7 \text{ M}^{-1} \text{ s}^{-1}$  and a  $E_A$  of ca. 25 kJ/mol.

Yet another setting for investigating rates of electron transfers between MPCs in solutions is in mixed valent layers formed around a working electrode (the diffusion layer). In electrode reactions of redox species dissolved in fluid solutions (such as acetonitrile or water), physical diffusion rates ( $D_{\text{PHYS}}$ ) are sufficiently fast that electron hopping (self-exchange) between oxidized and reduced species does not measurably contribute to the rate of electrochemical charge transport. In media where physical diffusion is slower and redox concentrations are high, however, electron hopping between oxidized and reduced species can augment (and even dominate) the physical diffusion transport.<sup>128–131</sup> The electron hopping component follows Fickian rules and is often called the electron diffusion coefficient,  $D_E$ . The pertinent (“Dahms–Ruff”) relationship<sup>128,129</sup> is

$$D_{\text{APP}} = D_{\text{PHYS}} + D_E = D_{\text{PHYS}} + \frac{k_{\text{EX}} \delta^2 C}{6} \quad (13)$$

where  $D_{\text{APP}}$  is the overall diffusive rate of electrochemical charge transport and  $k_{\text{EX}}$  is the electron hopping rate constant for electron transfer between redox species separated by an average equilibrium distance  $\delta$  and at total concentration  $C$ . The factor 6 accounts for the three coordinate dimensions along which electron hopping can occur. The use of eq 13 was introduced by Buttry and Anson<sup>130</sup> in the context of metal complexes sequestered by Nafion films on electrodes, and it has since been an inspiration for other<sup>132</sup> electron transfer rate studies in viscous and semisolid media.

The monolayers of MPCs can be comprised<sup>116–118</sup> of thiolated polyethylene (PEG) ligands, and  $\text{LiClO}_4$  electrolyte can be dissolved in the material by coordination with the PEG dipoles, giving a highly viscous, ionically conductive “polymer electrolyte” containing Au nanoparticles. Figure 15 shows a cartoon of  $\text{Au}_{25}(\text{SC}_2\text{Ph})_{18}$  MPCs (earlier misidentified as  $\text{Au}_{38}$  MPCs, as noted above) bearing (by ligand exchange) thiolated oligomeric PEG chains.<sup>95,116</sup> Microelectrode voltammetry could be conducted in this nanoparticle melt, containing  $\text{LiClO}_4$ , and in its undiluted state, and the characteristic doublet of oxidation current peaks (like Figure 10) could be seen and the rate of charge transport through the mixed valent melt next to the working electrode could be measured. Based on the assumption that  $D_{\text{PHYS}}$  was negligible, an MPC electron self-exchange rate of  $2 \times 10^4 \text{ s}^{-1}$  (or  $4 \times 10^5 \text{ M}^{-1} \text{ s}^{-1}$ ) was deduced from chronoamperometric results. Subsequent and more detailed measurements of charge transport in PEG-based  $\text{Au}_{25}$  MPC melts have suggested<sup>95</sup> that the rates of  $\text{Au}_{25}^{+1/0}$  electron hopping (actually  $\text{Au}_{25}^{0/-1}$  according to the recent charge state results<sup>91</sup>) are controlled by the rates at which charge-compensating counterions relocate in response to the charge displacement of the electron transfer, e.g., “ion atmosphere relaxation”.<sup>132</sup>

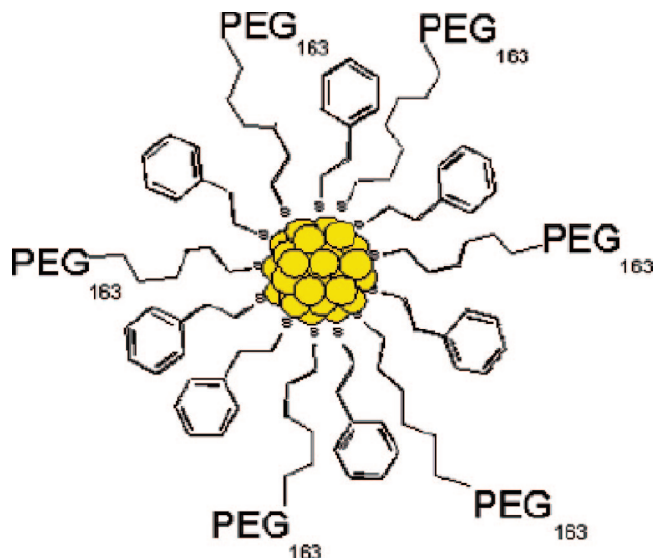


**Figure 15.** Cartoon of  $\text{Au}_{25}(\text{SCH}_2\text{CH}_2\text{Ph})_{18}$  MPC partially exchanged with (1-mercaptophex-6-yl)tri(ethylene glycol) methyl ether ( $\text{HSC6PEG}_{163}$ ). Reprinted with permission from ref 95. Copyright 2006 American Chemical Society.

### 3.5. Voltammetry of Nanoparticles with Molecular Redox Labels

Redox and other functionalities can readily be incorporated into the monolayers of MPCs by using thiolated redox molecules in the nanoparticle synthesis<sup>74,133</sup> or in ligand exchanges<sup>40,42,133–139</sup> onto preformed MPCs. They can also be coupled to already-functionalized MPCs by, for example, amide or ester-forming<sup>41,110</sup> reactions. In these ways, various redox functionalities such as ferrocene,<sup>40,42,75,134,140,141</sup> biferrocene,<sup>133–136</sup> anthraquinone,<sup>135,142,143</sup> viologen,<sup>42,110</sup> phenothiazine,<sup>41</sup> phenol,<sup>133</sup> and nitrobenzene<sup>134</sup> have been combined with nanoparticles, which with few exceptions<sup>43,138d,139,141</sup> have been Au MPCs. These materials are interesting multiredox entities capable of as many as 77 (and commonly over 10–15) electrons transferred per nanoparticle.<sup>43</sup>

The electrochemistry of redox moieties on MPCs has been observed by a variety of electrochemical methods. Rotating disk electrode (RDE) voltammetry produces steady state currents that suppress the contribution of adsorption of the redox-labeled MPCs onto the electrode. Adsorption or precipitation of electrode reaction products has been common in the cases of ferrocene, biferrocene, and viologen-labeled MPCs. The adsorption itself is typically studied using cyclic voltammetry or chronocoulometry and electrochemical quartz crystal microbalance (QCM). By and large, the observed voltammetry of redox moieties on MPCs has been unremarkable in regards to the electrochemical reaction potential(s). What is more interesting is the size of the electrochemical wave in relation to the number of copies of redox species present per nanoparticle.

Is there any synergy between the multiple electron transfer reactions that a multiredox MPC can undergo at an electrode surface or with another molecule? Do all of the redox species present on the MPC react? This issue has been addressed, first, by thin layer electrochemical coulometry performed<sup>144</sup> on a  $\sim\text{Au}_{140}$  MPC bearing phenothiazine ligands (see Figure 2), which showed that the number of electrochemically oxidizable phenothiazine groups was identical to the average number present as measured by  $^1\text{H}$  NMR. Second, wave-

shape analysis of steady state (RDE) voltammograms by conventional plots of potential vs  $\log[(i_{\text{lim}} - i)/i]$  exhibited<sup>41,110,134</sup> slopes close to that expected for a one electron ( $n = 1$ ) reaction. The slight curvature seen in some<sup>43,134</sup> of the plots made was attributed to possible variation in the formal potentials of the several redox groups present, which is not unreasonable given the possibilities for electrostatic interactions within the small volume encompassed by the MPC and its redox fringe. The result,  $n = 1$ , showed that—to a first approximation—the redox species react one-at-a-time, more or less independently of one another. The evidence thus indicates that all of the redox moieties attached to an MPC are independently, electrochemically reactive.

Possible pathways by which multiple, independent electron transfers might occur serially for multiredox labeled MPCs have been discussed<sup>134,142</sup> in the context of anthraquinone and ferrocene redox groups attached to the MPC core by alkanethiolate chains. For the latter, the electrochemical reversibility of the ferrocene couples means that hydrodynamic transport ( $\sim 25 \text{ s}^{-1}$  at 3600 rpm RDE rotation) is much slower than the overall electron transfer process. (A) One electron transfer pathway, imagined for a redox site on the opposite side of the core from the electrode, at the time of diffusional contact with the electrode, is electron transfer through the MPC Au core, by tunneling through the linker chains connecting the redox couple to the core and through other linker chains onward to the electrode on the other side of the core. This rate depends on the linker chain lengths; for C5 and C8, rates of  $\sim 2 \times 10^6$  and  $3 \times 10^4 \text{ s}^{-1}$  were estimated. (B) A second pathway imagined involves rotational diffusion of the nanoparticle at the electrode/solution interface. According to the relation

$$\tau_R = 4\pi R^3 \eta / 3kT \quad (14)$$

where  $R$  is MPC radius and  $\eta$  the medium viscosity, taking  $R = 1 \text{ nm}$  and  $\eta = 0.5 \text{ cp}$ , the rotational time constant  $\tau_R \sim 2 \times 10^7 \text{ s}^{-1}$  was estimated. (C) A third pathway relies on the redox groups exchanging electrons with one another so as to circumnavigate the MPC “globe”. (This nanoparticle reaction mechanism has been treated in some detail for the analogous case of adsorbed, multiply redox-labeled dendrimers.<sup>145</sup>) This rate was estimated based on assuming various values of  $D_E$  (*vide supra*) and site–site distances, which produced electron transfer rates from  $2 \times 10^3$  to  $1 \times 10^6 \text{ s}^{-1}$ , depending on assumptions about  $D_E$ . One sees from this analysis that, for the case examined, rotational diffusion is the likely most dominant—but perhaps not exclusive—electron transfer pathway. The principal value of this discussion is to bring out the parameters that must be optimized in order to force electron transfer rate control to one or the other of these three pathways.

A fourth circumstance would arise when *multiple* redox species are *electronically coupled* to one another, *through* the MPC core. This MPC architecture requires that the redox site(s) have some resonance interaction with the MPC core, and perhaps that the core is of the molecule-like dimension. At least three reports<sup>133,135,140</sup> would appear, from the thiolate ligand structures employed (4-hydroxyl- and 4-nitro thiophenol<sup>133,135</sup> and 4-ferrocene thiophenol<sup>140</sup>) to have achieved the former but not the latter condition. This extremely interesting prospect for redox labeled MPCs would seem to deserve further scrutiny.

Given the preceding analysis of electron transfer pathways, that show likely control by rotational diffusion in the absence



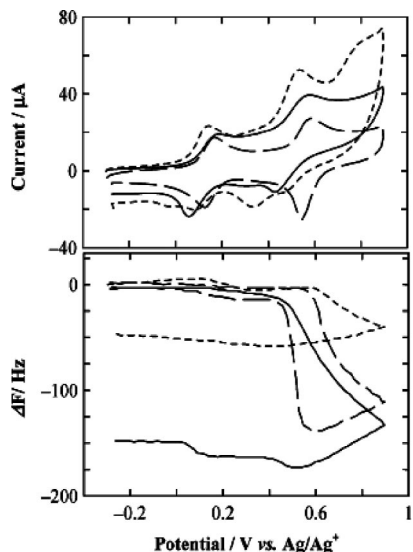


**Figure 16.** Cyclic voltammograms (top) and  $\Delta F$  (QCM frequency) – potential curves (bottom) of  $5.2 \mu\text{M Au}_n\text{-BFC}$  at a gold electrode in  $0.1 \text{ M Bu}_4\text{NClO}_4\text{-THF}$  (solid line), toluene/MeCN (dotted line), and  $\text{CH}_2\text{Cl}_2$  (dashed line) at  $100 \text{ mV/s}$  between  $-0.3$  and  $0.9 \text{ V vs Ag/Ag}^+$ . Reprinted with permission from ref 134. Copyright 1998 American Chemical Society.

of through-core coupling, it is not surprising that attempts to evoke multielectron or accelerated rates using redox labeled MPCs have not thus far achieved special catalytic results. For example, the rate of electron transfer-mediated reduction of 1,1-dinitrocyclohexane by electrode-generated anthraquinone (AQ) radical anions attached to Au MPCs was higher than reaction rates of freely diffusing AQ, but the main reason was reaction layer compression caused by the relatively slower MPC diffusion rate, allowing a faster net turnover.<sup>142</sup>

Another direction for functionalized MPCs lies in schemes wherein substituents of nanoparticle ligands influence electrochemical processes through their binding chemistry. This was illustrated by Rotello<sup>146</sup> with MPCs with diacyldiaminopyridine hydrogen-bonding recognition sites in their monolayers. These sites were shown to bind a flavin and alter its redox potential—with the reduced flavin being bound more strongly than the oxidized form. This binding chemistry in effect yields a route to an electrochemically controlled modulation of the MPC functionality.

Another interesting feature of multiredox labeled MPCs is their adsorption or precipitation onto electrodes. Au MPCs bearing ferrocene,<sup>40,42,75,134</sup> phenothiazine,<sup>41,142</sup> and viologen<sup>42,110</sup> groupings all tend to adsorb onto working electrodes following their electrode reactions. These adsorptions are relatively weak, generally desorbing from the electrode upon reversal of a cyclic voltammetric scan and/or are easily rinsed off in fresh electrolyte. An exception<sup>75</sup> is a perferrocenated  $\sim\text{Au}_{225}$  MPC, which forms a tenacious adsorbed monolayer that can be transferred to give stable voltammetry in MPC-free electrolyte solutions. Another notable exception<sup>134–137</sup> is the behavior of Au and Pd MPCs bearing, by ligand exchanges, 4–20 biferrocene groupings. As shown in Figure 16, the cojoined ferrocenes react in two waves, and the second oxidation is accompanied, in the electrochemical QCM (quartz crystal microbalance) response, by a large frequency decrease signifying deposition of considerable quantities of MPCs onto the electrode. The electrode reaction produces quite highly charged nanopar-

ticles, and the biferroceniums thereon are not intrinsically highly soluble in the solvents used, so aggregation and deposition onto the electrode occurs. Also, as might be expected, the process is very sensitive to both solvent<sup>134</sup> and electrolyte; the data in Figure 16 show, for example, that the deposition tendency is highest in tetrahydrofuran (THF) and lowest in methylene chloride.

#### 4. Electrochemistry of Films of Nanoparticles

Diverse chemistries have been used to incorporate (mostly Au MPCs) nanoparticles into monolayer and multilayer films on electrodes. In studies of film electrochemistry where the film is in contact with an electrolyte solution, monolayers of MPCs have been linked to electrodes using dithiols<sup>48,61,68,70,147,148</sup> as bridges between the electrode and the MPC core and by coupling carboxylate functionalities<sup>149</sup> on the electrode (self-assembled monolayer) and on the MPC together by coordination to a suitable metal ion (such as zinc or copper). Monolayers of MPCs have also been prepared by the Langmuir–Blodgett (LB) method and their electrochemistry studied at the air/water interface<sup>150–153</sup> and as monolayer films transferred to electrodes.<sup>154–156</sup> LB films can be further modified by dithiol linking,<sup>150,151</sup> and the MPCs in the LB film can include redox functions in their monolayers.<sup>155</sup>

For films containing multilayers of MPCs, maintaining electroneutrality during changes in the charge state of the film's nanoparticles requires some level of ionic conductivity of the film. Using multilayer films cast from MPC solutions in solvent/electrolyte media in which the MPCs are insoluble<sup>72,157</sup> (and the film perhaps poorly swollen) tends to be tricky, since the films may have minimal ionic conductivity. Some form of MPC-to-MPC linking chemistry and good film solvation makes the experiment more controllable. Electrochemical studies have been reported for multilayer films in which the MPCs are linked together using carboxylate/metal ion/carboxylate<sup>158,159</sup> and pyridine (or poly pyridine)/metal ion/pyridine linking,<sup>69</sup> dithiol linking,<sup>160,161</sup> and DNA hybridization.<sup>32,33,162</sup> Layer-by-layer deposition<sup>163</sup> is also possible, taking advantage<sup>158,164</sup> of multiple electrostatic interactions between electrode-adsorbed cationic polymer chains and negatively charged MPCs (or the reverse charges) to form insoluble but ionically conductive layers. Electrostatic interactions are also important in formation of strongly adsorbed monolayers<sup>75</sup> and multilayers<sup>134–137</sup> of MPCs bearing redox labels.

In another category of multilayer MPC film electrochemistry, the film is formed between two electrode contacts, typically an interdigitated electrode array (IDA), and its electronic conductivity is measured with the film bathed in a gas of various composition or a nonionic solvent. In this experiment, the electronic conductivity is supplied by electron hopping between MPCs and desirably does not involve electrolysis at the film/electrode interfaces; thus, ionic conductivity is avoided in the experiment design. The rate of electron hopping in dry MPC films is affected, among other factors, by the (electron tunneling) distances between metal MPC cores, by their local site mobilities,<sup>165</sup> and by anything (such as sorbed organic vapor) that would affect those properties. The MPC films can be simply cast (unlinked) films,<sup>96,119,165–170</sup> can be films made by the LB method and transferred to an IDA,<sup>171</sup> or may be MPCs linked together by carboxylate/metal ion or dithiol<sup>165,167,172–178,178,180,181</sup> chemistries similar to those mentioned above. Studies of these MPC films have been oriented on the one hand to

gaining understanding of factors influencing their conductivity and on the other hand toward their applications as sensors of organic vapors. In the latter application, the films are often referred to as “chemiresistors”.

#### 4.1. Electrochemistry of Monolayers of Nanoparticles

An early study<sup>48</sup> of MPC monolayers used dithiol linking in two different schemes. In one, an electrode bearing a self-assembled monolayer (SAM) of 4,4'-thiobisbenzenethiol (TBBT, (HSPH)<sub>2</sub>S) was exposed for an extended period of time to a solution of carefully fractionated butanethiolate-protected  $\sim$ Au<sub>140</sub> MPCs. The thiols on the SAM surface exchanged into the MPC monolayer, displacing butanethiol. This procedure, hopefully self-limiting to formation of a single layer of nanoparticles, produced a surface coverage of about  $1.3 \times 10^{-11}$  mol/cm<sup>2</sup>. In a second scheme, the TBBT dithiol was exchanged into the MPC monolayer, producing mixed monolayer MPCs with protruding thiol groups which could subsequently bind to a naked Au electrode surface. While a submonolayer coverage was obtained ( $\sim 0.8 \times 10^{-11}$  mol/cm<sup>2</sup>), this procedure is not intrinsically self-limiting, since MPC oligomers may form, requiring more caution.

The AC impedance of the above MPC monolayers displayed<sup>48</sup> undulations in the capacitance and resistance elements of the electrode/electrolyte interface whose spacing on the potential axis was consistent with that expected for QDL voltammetry of the  $\sim$ Au<sub>140</sub> nanoparticle. A useful part of the impedance results was to establish the potential of a capacitance minimum at  $-0.1$  to  $-0.2$  V vs Ag/AgCl, which was assigned to the  $E_{PZC}$ , or potential of zero charge, of the  $\sim$ Au<sub>140</sub> MPCs.

Subsequent work by Chen<sup>147</sup> presented an improved procedure for preparing Au MPCs with mixed hexanethiolate/1,6-hexanedithiolate monolayers, without contamination by oligomers, and forming SAMs of these MPCs on Au electrodes. The AC impedance results confirmed the  $E_{PZC}$  potential as  $-0.22$  V vs Ag/AgCl. Estimates of the rates of electron transfers between electrode and MPC gave rate constants of  $\sim 20$  and  $\sim 10$  s<sup>-1</sup>, using AC impedance and linear sweep results, respectively. Analogous experiments<sup>149</sup> in which  $\sim$ Au<sub>140</sub> MPCs coated with a mixed monolayer of hexanethiolate and mercaptoundecanoic acid (MUA) were bound by Zn<sup>2+</sup> coordination to a MUA SAM on a Au electrode gave estimates of heterogeneous electron-transfer rates in from 40 to 160 s<sup>-1</sup>, using linear potential sweeps, ac impedance, and potential step techniques.

These quantitative rate studies of MPC monolayers provide a valuable beginning for understanding the dynamics of electron transfers to metal nanoparticles but are far from achieving the convincing detail in studies of SAMs on flat, Au(111) surfaces bearing redox groupings such as ferrocene.<sup>182–184</sup> The electron transfers of these surface bound redox materials presumably occur by tunneling via the chain linking the redox molecule or MPC core and the electrode, or via the surrounding, nonlinking ligands. The classical signature of electron tunneling, an exponential relation between linking chain length and electron transfer rate constant, has been identified for the well-defined ferrocene SAMs but not for monolayers of nanoparticles on electrodes. Also, the rate constant for ferrocene oxidation through a hexanethiolate connector is  $> 10^6$  s<sup>-1</sup>, far larger than the existing MPC-based measurements.

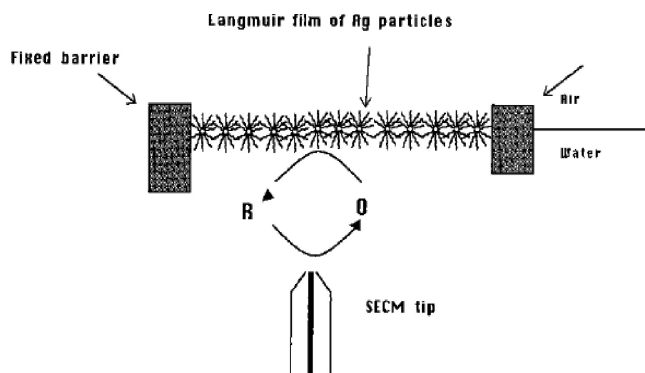


**Figure 17.** Schematic representation illustrating positive feedback at an inverted SECM tip upon compressing a Langmuir film of Ag MPCs through the insulator-metal transition at the air/water interface (not to scale). Reprinted with permission from ref 113. Copyright 2002 American Chemical Society.

#### 4.2. Nanoparticle Films Made by Langmuir Methods

Spreading of a layer of hydrophobic (e.g., alkanethiolate-protected at least in part) MPCs at the air/water interface of a Langmuir trough offers the opportunity to observe the surface pressure, optical, and electrical properties of potentially well-defined monolayers of MPCs. Seminal experiments by Heath et al.<sup>185–187</sup> on monolayers of alkanethiolate-protected Ag MPCs provoked a metal-insulator transition by compression of the LB monolayer. The transition was detected by observing a sharp change in monolayer reflectivity and luster when the ratio  $D/2r$  was decreased (by film compression) below a certain value that depends on the alkanethiolate chain length ( $D$  = separation between nanoparticle centers;  $r$  = radius of the Ag core). When strongly compressed, so that the edges of the Ag cores became separated by  $\sim 1$  nm, the overlap of quantum mechanical wave functions of adjacent particles led to exchange coupling, a diminution of the charging energy, and a transition to metallic-like properties. This interpretation was supported by ac impedance measurements<sup>185</sup> (using IDA electrodes) of the Ag MPC monolayers. The Ag MPC films are described<sup>185</sup> as superlattice Mott insulators that are characterized by a Coulomb gap that originates from the single particle charging energy. Their experiments also demonstrated the power of the LB approach to manipulate the MPC spacing in a more or less continuous manner.

Quinn and Bard observed<sup>188</sup> the metal-insulator transition for monolayers of Ag MPC in a Langmuir trough, under increasing compression, in a different way. Oxidation currents for ferrocene methanol at an upward facing scanning electrochemical microscope (SECM) tip in the Langmuir subphase (Figures 17 and 18) signaled negative feedback, or diffusional blocking, when the tip approached a loosely compressed and nonconductive MPC monolayer. As seen in Figure 18, at higher compression, the response changed to positive feedback as the MPC layer became more conductive and could dissipate the charges transferred from the electrogenerated ferrocenium species to the nanoparticles under the SECM tip. This experiment was extended<sup>156b</sup> to Langmuir monolayers of alkanethiolate-protected Au MPCs ( $\sim 7$  nm diameter) that had been transferred to a glass slide, examining the SECM approach curves as a function of the Langmuir trough compression of the Au MPC before transfer. Films with  $D/2r = 1.38$  behaved as insulators, showing diffusional blocking behavior toward the ferrocene

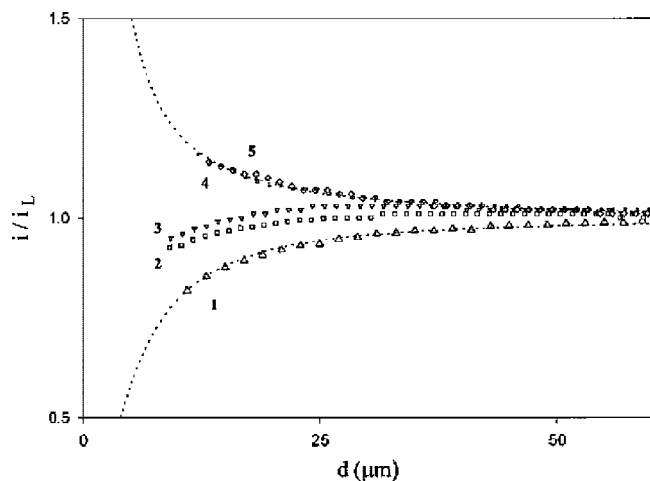


**Figure 18.** SECM approach curves to the MPC film at various compressions (1–5 as in Figure 2): (1) open barrier position  $0 \text{ mN m}^{-1}$ , (2)  $11 \text{ mN m}^{-1}$ , (3)  $22 \text{ mN m}^{-1}$ , (4)  $42 \text{ mN m}^{-1}$ , and (5)  $56 \text{ mN m}^{-1}$  (closed barrier position). Dotted lines represent the theoretical approach curves to an insulator (lower) and a conductor (upper). Reprinted with permission from ref 188. Copyright 2001 American Chemical Society.

methanol mediator, whereas those with  $D/2r = 1.19$  showed conductive behavior, producing feedback in the approach curves. The kinetics of electron transfers between the SECM redox mediator ( $\text{Fe}(\text{CN})_6^{4-}$ ) and the MPCs in tightly and loosely compressed LB monolayers of Au MPCs were also deduced<sup>156</sup> as  $k^0 = 1.1 \times 10^{-3}$  and  $1.7 \times 10^{-4} \text{ cm/s}$ , respectively. The diminution of the latter rate was interpreted as an enhanced charging energy in the loosely compressed monolayer, decreasing the rate of electron transfers between MPCs and the rate of conducting charge away from the SECM tip's area of mediator injection.

Experiments by Majda<sup>153</sup> on Langmuir monolayers of octanethiolate and dodecanethiolate MPCs showed that film compression could produce packing comparable to that in the pure MPC solid (according to observed octanethiolate and dodecanethiolate MPC radii). Charging currents could be seen at microband electrodes contacting the monolayer film, but it was evident that only segments of the film nearest the electrode were electronically accessed. In contrast, monolayers of MPCs with about 20% of the alkanethiolates replaced with ferrocene-terminated ones ( $\omega$ -(ferrocenylcarbonyloxy)hexadecanethiolate) gave cleanly defined voltammetry, demonstrating redox connectivity by electron hopping between ferrocenes. Following previous, analogous experiments with osmium complexes,<sup>189</sup> a  $\text{Fc}^{1+/0}$  electron exchange rate constant of  $4 \times 10^6 \text{ M}^{-1} \text{ s}^{-1}$  was deduced from the 2-D electron diffusion coefficient at the air/water interface. This rate constant is very close to that known<sup>126</sup> for  $\text{Fc}^{1+/0}$  electron exchange in acetonitrile ( $4 \times 10^6 \text{ M}^{-1} \text{ s}^{-1}$ ), and it appears that the electron exchange occurs solely by  $\text{Fc}^{1+/0}$  reactions and that the MPC core is not part of the reaction pathway.

Langmuir monolayers can be linked together to prepare<sup>150,151,190</sup> rather robust films, by mixing TBBT or alkane dithiols with various alkanethiolate-protected Au MPCs and then bringing the film under compression for a period of time to allow ligand exchange reactions to occur. Langmuir films can also be prepared,<sup>151</sup> using Au MPCs with mixed monolayers of alkanethiolates and  $\omega$ -ferrocenated alkanethiolates, and transferred to Au film electrodes, either as single MPC monolayers or multiple layers up to four monolayers. (Larger

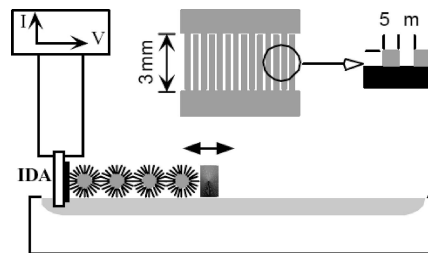


**Figure 19.** Schematic setup of electrical conductivity measurements of nanoparticle Langmuir monolayers. The inset shows the dimensions of the interdigitated array (IDA) electrode. Reprinted from ref 155, Copyright 2003, with permission from Elsevier.

numbers of monolayers could not be transferred). These films, when placed in aqueous electrolyte, showed a variety of symptoms of reorganizing and loss of electroactivity.

Other interesting experiments<sup>152,156</sup> with Langmuir films have involved inserting an IDA vertically through the air/water interface (Figure 19) and allowing the subsequently spread MPC film to contact the electrode/gap/electrode structure at varied film compressions. Upon sweeping the voltage bias between the IDA fingers, some experiments produced<sup>155</sup> reasonably linear current–voltage responses and 2-D conductivities sensitive to the Langmuir balance pressure. Others produced<sup>152</sup> remarkably QDL voltammetric-like features. Even though highly purified water was used for the subphase, this electrolytic reaction-like behavior would seem to demand the participation of counterions entering the monolayer film. The electroneutralization of a monolayer of MPC charges would require only an extremely low ionic content of the subphase.

Lee<sup>190</sup> carried out an analogous experiment on LB films of nanoparticles (labeled as  $\text{Au}_{38}$  but as noted previously probably  $\text{Au}_{25}$ ), using a line electrode in the manner described by Majda<sup>191</sup> and including an electrolyte in the subphase. The voltammetry of the first oxidation wave of this nanoparticle was well defined, and its current maximum responded to the chain length of the alkanedithiol used to link the film together. Oxidation charge spreads outward from the line electrode by electron hopping between nanoparticles; and the electron diffusion coefficients  $D_E$  varied with alkanedithiol chain length with an electronic coupling factor of  $\beta = 0.82 \text{ \AA}^{-1}$ .

### 4.3. Electrochemistry of Multilayer Films of Nanoparticles

Forming molecular or nanoparticle monolayers is typically straightforward as a paper scheme but is more difficult to execute in practice. It is not surprising then that the literature on multilayer MPC films is more highly developed. As noted above, films containing multilayers of nanoparticles have been used in voltammetric experiments, where they are contacted by electrolyte solutions, and in a “dry” state where the film is bathed in a nonionic or gaseous medium.

#### 4.3.1. Films Wetted by Electrolyte Solutions

An early multilayer Au MPC film was prepared<sup>161</sup> by adsorbing bromide-stabilized 6 nm diameter Au nanoparticles onto conductive indium tin oxide (ITO, optically transparent) films and then dithiol-linking the nanoparticles together by bathing in a solution of 1,4-benzenedimethanethiol. The film formation was tracked by ellipsometric spectroscopy as the above procedure was repeated, building  $>30 \text{ nm}$  thick



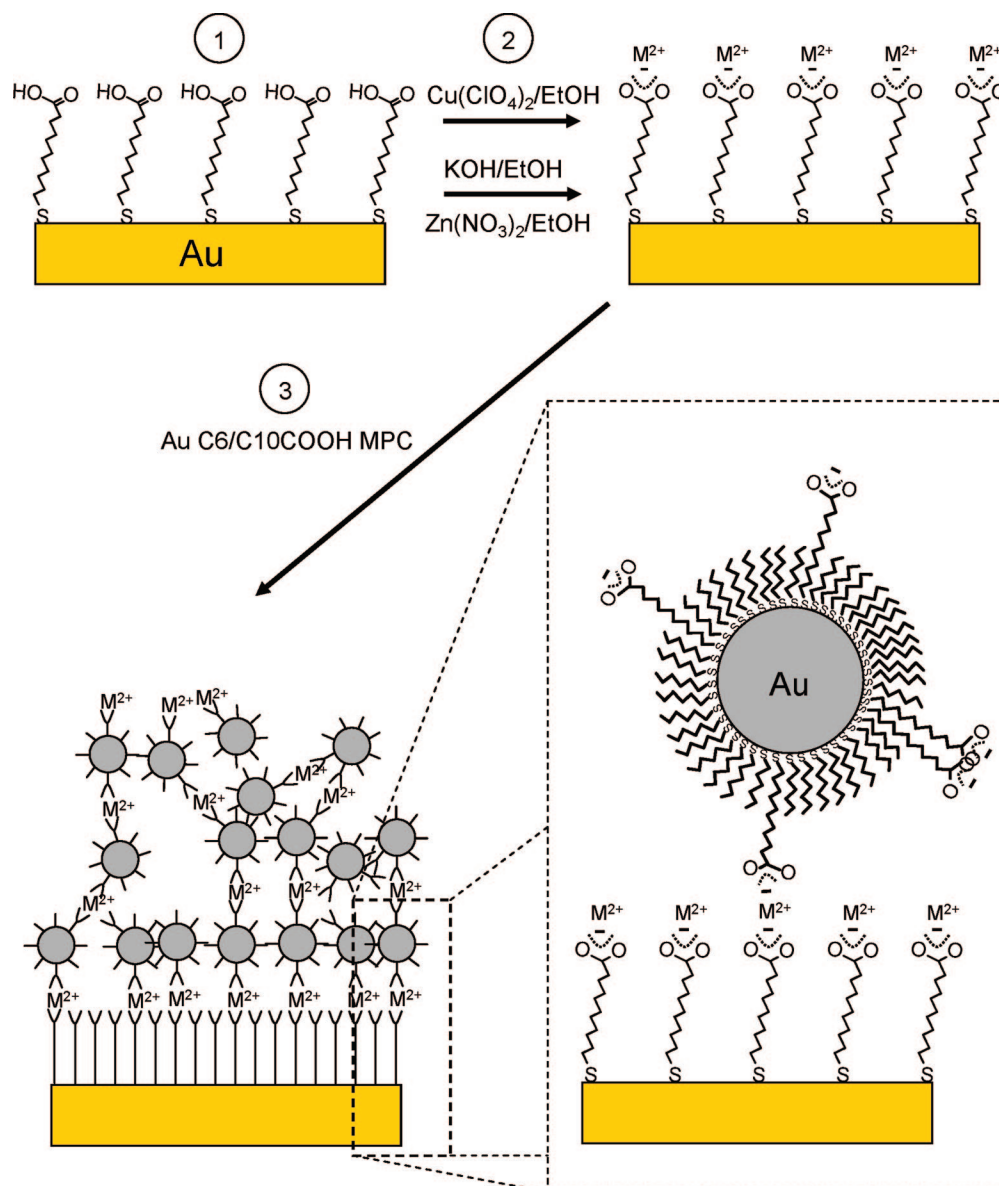


**Figure 20.** Scheme for forming carboxylate/metal ion/carboxylate films from mixed monolayer MPCs. Adapted from ref 159. Copyright 2000 American Chemical Society.

multilayer films. When it was placed in aqueous KCl electrolyte and a modulating ac potential was applied, a modulated optical transmittance spectrum of the nanoparticle film was obtained that could be considered in light of the optical theory of metals. The spectral changes meant that charge could be electrolytically injected into the film, but it was concluded that this involved only the outer layer of nanoparticles. The film was sufficiently conductive when used as an electrode to give well defined cyclic voltammetry of  $\text{Fe}(\text{CN})_6^{4-}$ .

Further studies using multilayer nonlinked-together films of smaller Au MPCs showed that their electroactivity is quite sensitive to the chosen aqueous electrolyte and to doping the aqueous medium with an organic component. Multilayer voltammetry reflective of  $\sim\text{Au}_{140}$  QDL charging<sup>71</sup> could be seen only with selected electrolytes that, with undoubtedly some accompanying solvent, could permeate to MPC sites below those immediately present at the MPC/aqueous interface. Ranganathan<sup>157</sup> showed that multilayer  $\text{Au}_{25}$  MPC films can act as working electrode surfaces only at potentials near the intrinsic redox energies of  $\text{Au}_{25}$  nanoparticles, and

not at potentials within the band gap of this molecule-like nanoparticle.

Linking MPCs together allows use of solvents in which the thiolate ligand monolayers are well-solvated, which facilitates counterions entering/leaving for the sake of electroneutrality as the film is internally charged by electron hopping. A scheme for binding  $\sim\text{Au}_{140}$  MPCs together with carboxylate/metal ion/carboxylate coordination<sup>158,159</sup> is illustrated in Figure 20. Carboxylic acid groups on SAMs are exposed first to a metal ion solution and then to a solution of MPCs with mixed monolayers that include carboxylic acid functions. Repetition of this procedure ("dip cycles") builds up multiple layers of MPCs (as evidenced by adsorption spectra and voltammetry) at a rate exceeding one monolayer per cycle, apparently owing to the retention of metal ions in the film. Cyclic and differential pulse voltammetries (CV, DPV, respectively) showed<sup>149,159</sup> well defined current peaks spaced by potential intervals consistent with QDL charging of  $\sim\text{Au}_{140}$  MPCs, even for films containing as many as *ca.* 55 monolayers (measured by CV charge integration). The presence of QDL charging peaks requires that the time scale

for electron hopping through the multilayer, and equilibration of the entire MPC film with the applied electrode potential, be shorter than that of changing the working electrode potential in the voltammetric experiment. The rate of electron hopping between MPCs was fast (average first-order rate constant  $k_{\text{HOP}} = 2 \times 10^6 \text{ s}^{-1}$  and average self-exchange rate constant  $k_{\text{EX}} = 2 \times 10^8 \text{ M}^{-1} \text{ s}^{-1}$ ), as measured<sup>149</sup> by potential step chronoamperometry, and was not discernibly dependent on which MPC core charge state change was measured. This electron transfer rate being larger than could be rationalized on the basis of electron tunneling through the MPC linker chains lead to the conclusion that the linker chain flexibility allowed considerable local mobility of the MPC structures and that the operative electron tunneling pathways involved the shorter, *non*-linker MPC ligands. This conclusion and the failure of the carboxylate/metal ion/carboxylate coordination linking chemistry to rigorously enforce distances of electron transfer were also evident in RDE results<sup>160a</sup> and in the electronic conduction of similarly prepared dry MPC films, as noted later.

A metal ion-linker scheme analogous to Figure 20 was reported by Chen<sup>69</sup> in which pyridine groups replaced the carboxylic acids and the metal ion of choice was Cu(II). This chemistry also formed multilayers at a fast rate, probably again by retention of metal ions in the film, whose growth was tracked by QCM measurements. The  $\sim\text{Au}_{314}$  MPC multilayer films were investigated in aqueous media, where the features of selective anion incorporation,<sup>61</sup> and cation rejection, called rectified quantized charging were again seen.

Uosaki et al.<sup>158,192</sup> showed that 1.8 nm diameter Au MPCs with mixed hexanethiolate/mercaptoundecanoic acid/ferrocenylhexanethiolate monolayers could also be assembled into multilayer films using carboxylate/ $\text{Cu}^{2+}$ /carboxylate coupling (Figure 20) and that such films displayed well-defined ferrocene electroactivity up to ferrocene charges of  $3 \times 10^{-9} \text{ mol/cm}^2$ . The increments of ferrocene charge were linear with dip cycle up to 6 cycles, which was consistent with ellipsometric and QCM data. Layer-by-layer growth of multilayers of MPCs was also achieved by exposing the electrode alternately to solutions of the cationic polymer poly(allylamine) hydrochloride and MPCs with mixed hexanethiolate/mercaptoundecanoic acid monolayers, tracking the film growth with ellipsometric and QCM data. Layer-by-layer formation of  $\sim\text{Au}_{140}$  MPC multilayers having mixed monolayers containing anionic and cationic groupings, with cationic and anionic polymers, was also demonstrated by Hicks et al.<sup>164a</sup> QDL charging peaks could be indistinctly seen in the voltammetry of the multilayer. The electrostatic ideas of layer-by-layer film formation can also be used for patterning of MPC deposition by patterning the charges present on the initial substrate surface.<sup>164b</sup>

The outer surfaces of multilayer films of MPCs can act as electrodes toward redox solutes in the adjoining solution. Brennan et al.<sup>160a</sup> described a scheme (Figure 21) analogous to those used earlier on redox polymer films<sup>193</sup> on electrodes, to assess the rate of electron hopping between  $\sim\text{Au}_{140}$  MPCs in multilayer films linked together by dithiolate bridges and by carboxylate/ $\text{Cu}^{2+}$ /carboxylate bridges. With electrode potentials chosen—based on the observed QDL charging voltammetry—to generate  $\sim\text{Au}_{140}^{2+}$ ,  $\sim\text{Au}_{140}^{3+}$ , or  $\sim\text{Au}_{140}^{4+}$  charge states in the film, ferrocene could be oxidized at the film/solution interface. The experimental design aimed at achieving rates of ferrocene mass transport and interfacial MPC oxidation of the ferrocene that were larger than the

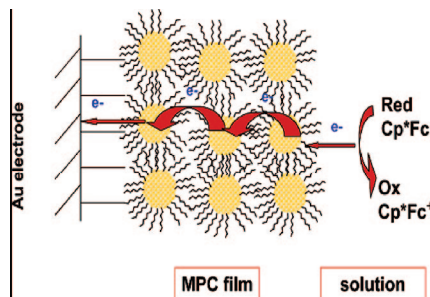


**Figure 21.** Cartoon depicting mediated electron-transfer oxidation of decamethylferrocene ( $\text{Cp}^*\text{Fe}$ ) by a multilayer MPC film assembled on an electrode. Reprinted with permission from ref 160a. Copyright 2004 American Chemical Society.

rate of electron hopping within the MPC film. The behavior of the RDE currents was in apparent accord with theory<sup>193</sup> for this scheme, except that the dependency of apparent hopping rate on film thickness was not ideal. Rate constants for electron hopping were in the  $k_{\text{HOP}} \sim 1 \times 10^5 \text{ s}^{-1}$  range (somewhat smaller than an earlier study<sup>159</sup>) and did not systematically respond to changes in the MPC charge state, to changes in the dithiolate linker length, or to the differences between lengths of dithiolate vs carboxylate/ $\text{Cu}^{2+}$ /carboxylate linkers. These results again show that the use of flexible linkers surrounded by shorter nonlinker ligands does not rigorously enforce distances (and tunneling lengths) between MPC cores in these films. It is here appropriate to call attention to the above-cited capabilities of the LB approach to enforce nanoparticle spacing, at least in monolayers of MPCs.

#### 4.3.2. Electronic Conductivity of Dry Films

As mentioned above, measurements of the electronic conductivities of MPC films not contacted by electrolyte solutions have been variously aimed at understanding of their conductivity and of structural factors influencing it, and on their possible applications as sensors of organic vapors.

Conductivity measurements<sup>194</sup> on films of unlinked 2.4 nm core diameter Au MPCs (cast on IDAs), having alkanethiolate (C8, C12, C16) monolayers, produced linear current–potential responses to potential scans (at low potentials) and well-formed AC impedance semicircles reflective of frequency-independent film resistance and capacitance. The conductivities and electron hopping rates of these films decrease and the activation energy barrier increases systematically with increasing alkanethiolate chain length. The relevant parameter for analysis of the dependency of electron hopping rate on alkanethiolate ligand is the average separation between MPC core edges, which from density measurements on solid samples proved to be close to the length of a single chain. Extensive *intercalation*, or bundling, of the alkane chains of adjacent MPC monolayers was inferred, in agreement with theory<sup>52</sup> and microscopy.<sup>195</sup> The film conductivities changed exponentially with the core–core edge separation (electronic coupling slope  $\beta \sim 1.2 \text{ \AA}^{-1}$ ), a result consistent with distance-dependent tunneling through the intervening alkanethiolate monolayers. Further measurements<sup>161</sup> on dithiol-linked 6 nm diameter Au nanoparticle films produced conductivities that decreased by  $\sim 10$ -fold for three-methylene increments in chain length (C6, C9, and C12 dithiolate linkers).

The preceding results were on Au MPC films that were nominally uncharged, so that the electron carriers that hop

between MPC cores were thermally generated, i.e., by the disproportionation reaction



In MPC films in which the carrier populations are, in contrast, synthetically controlled by how the film was prepared, the electron transport should be faster and proceed by the hopping mechanism



where the  $x1$  and  $x2$  subscripts denote positions between which the electronic charge is transported by the reaction. This reaction is analogous to electron transport in mixed valent redox polymers<sup>196</sup> and is a bimolecular reaction. Wuelfing<sup>117a</sup> ascertained the bimolecularity of charge transport rate for alkanethiolate-protected  $\sim\text{Au}_{140}$  MPCs, using films chemically prepared to be mixed valent in (for example) known  $\sim\text{Au}_{140}^{1+}$  and  $\sim\text{Au}_{140}^0$  proportions through the relation of rest potentials of mixed valent solutions to the formal potential of the  $\sim\text{Au}_{140}^{1+/0}$  QDL charging peak. Assuming a cubic lattice model, an estimate of the bimolecular electron transfer rate constant  $k_{\text{EX}}$  ( $\text{M}^{-1} \text{s}^{-1}$ ) from film conductivity  $\sigma_{\text{EL}}$  ( $\Omega^{-1}\text{cm}^{-1}$ ) is gained through the equation

$$k_{\text{EX}} = \frac{6RT\sigma_{\text{EL}}}{10^{-3}F^2\delta^2[\text{MPC}^0][\text{MPC}^{+1}]} \quad (17)$$

where  $R$  is the gas constant,  $T$  is temperature (K),  $F$  is the Faraday constant, and  $\delta$  is the core center-to-center distance (cm) in the film. Values of  $k_{\text{EX}}$  thus derived were independent of the degree of mixed valency, as expected, and were quite large, near  $10^{10} \text{M}^{-1} \text{s}^{-1}$  with activation barriers of  $6.7 \pm 0.7 \text{ kJ/mol}$ .

Quinn et al.<sup>117b</sup> have recently extended ideas of a previous study<sup>188</sup> in an SECM measurement of local electronic conductivity of MPC films; this report has promise for comparing electronic hopping rates in dry and solvent-wetted films.

An extension<sup>96</sup> of this theme to mixed valent films of much smaller  $\text{Au}_{25}(\text{SC2Ph})_{18}$  MPCs (earlier misidentified as  $\text{Au}_{38}$  MPCs, as noted above) confirmed the bimolecular character of their electron transport mechanism but produced the surprising result that the  $\text{Au}_{25}$   $k_{\text{EX}}$  is much smaller (by  $\sim 10^3$ -fold) and the activation barrier much larger (by  $\sim 3$ -fold). Figure 22 compares the fitted second order rate plots for the  $\sim\text{Au}_{140}$  and  $\sim\text{Au}_{25}$  MPCs. Following a process of elimination of other plausible reasons, it was speculated that the  $\text{Au}_{25}(\text{SC2Ph})_{18}$  MPCs might be influenced by an inner sphere energy barrier-like term. Subsequent solution electron transfer rate measurements<sup>97,115</sup> and Raman spectra that show<sup>125</sup> that the Au–S stretch energy differs for the two charge states of the  $\text{Au}_{25}$  couple have confirmed this speculation. The detailed  $\text{Au}_{25}(\text{SC2Ph})_{18}^-$  structure is now known,<sup>36c</sup> it remains for future determination of that of  $\text{Au}_{25}(\text{SC2Ph})_{18}^0$  to attain a detailed understanding of the role of structural changes in the electron transfer behavior of this nanoparticle.

Measurements were also made<sup>117</sup> on nonmixed valent (i.e., neutral) films of  $\sim\text{Au}_{309}$  MPCs as a function of the alkanethiolate chain length, taking account of chain intercalation. In this more refined analysis of electron tunneling control of electron hopping, linear conductivity vs core–core separation plots gave the electronic coupling constant  $\beta \sim 0.8 \text{ \AA}^{-1}$ , a result lying within the range of coupling constants

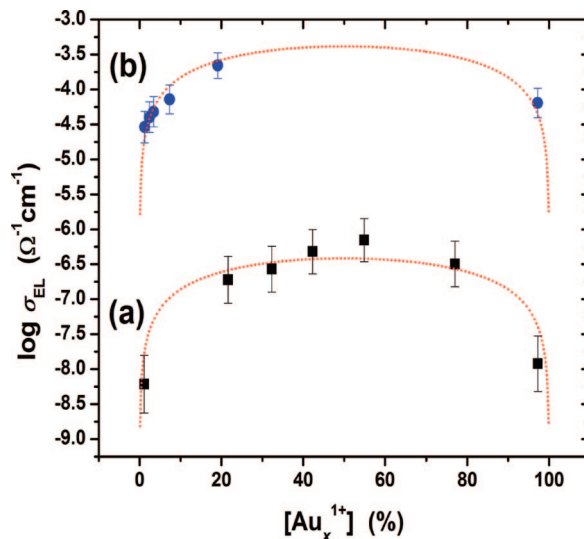


**Figure 22.** Effect of the concentration,  $[\text{Au}_x^{1+}]$  ( $x = 25$  or  $140$ ), on  $\sigma_{\text{EL}}$ : (a) mixed-valent  $\text{Au}_{25}$  MPCs; (b) mixed-valent  $\text{Au}_{140}$  MPCs. Estimated error bars are  $\pm 10\%$ . The red curves are  $\sigma_{\text{EL}}$  values simulated for a bimolecular reaction with rate constants  $1.5 \times 10^6 \text{M}^{-1} \text{s}^{-1}$  for  $\text{Au}_{25}$  and  $4.3 \times 10^9 \text{M}^{-1} \text{s}^{-1}$  for  $\text{Au}_{140}$ . Reprinted with permission from ref 96. Copyright 2006 American Chemical Society.

measured<sup>197</sup> for donor–acceptor pairs separated by trans-staggered alkane chains.

There are at present few examples in which electron hopping rate measurements in dry MPC films can be compared to measurements made in structurally and compositionally equivalent solvated films or solutions. Designing exactly parallel solid state and solution electron transfer environments and appropriate experimental tests is not straightforward. Electron hopping rates in solid state mixed valent MPC films, in which the mobility of counterions of charged species is insignificant on the global but not necessarily the very local scale, may be affected by the Coulombic effects of the counterion's local mobility and other factors. A recently examined case is that of the  $\text{Au}_{25}(\text{SC2Ph})_{18}^{0/1-}$  MPC couple (earlier misidentified as  $\text{Au}_{38}$  MPCs, as noted above), whose electron hopping rates were measured<sup>97</sup> in solid state mixed valent solids as  $2 \times 10^6 \text{M}^{-1} \text{s}^{-1}$  and in solutions of the MPC (by NMR) as  $3 \times 10^7 \text{M}^{-1} \text{s}^{-1}$ .<sup>115</sup> The observed activation energy barriers and pre-exponential terms are, respectively, 20 and 25 kJ/mol and  $\sim 3 \times 10^8$  and  $\sim 9 \times 10^{11} \text{M}^{-1} \text{s}^{-1}$ . Thus, the slower hopping rates in the mixed valent solid are provoked by the smaller pre-exponential term, as compared to the dilute mixed valent solution. The large activation energy barriers indicate the presence of a substantial “inner sphere” reorganizational term in both media.

Mirkin et al.<sup>32</sup> in 1996 described important experiments in which (much larger) oligonucleotide-modified Au nanoparticles could become linked together in solution, or aggregated, by hybridization with complementary strands of DNA (target). The ensuing optical changes generated a clear signal of specific interbinding of nanoparticles. This work set off a broad investigation in many laboratories on the use of DNA for highly specific nanoparticle linking chemistry and analytical uses of it. The bioanalytical aspects of this area, including DNA-induced nanoparticle aggregation, have been recently reviewed<sup>198</sup> and are not further assessed here.

Others have taken up the use of DNA hybridization with oligonucleotide-modified nanoparticles to, for example, elicit



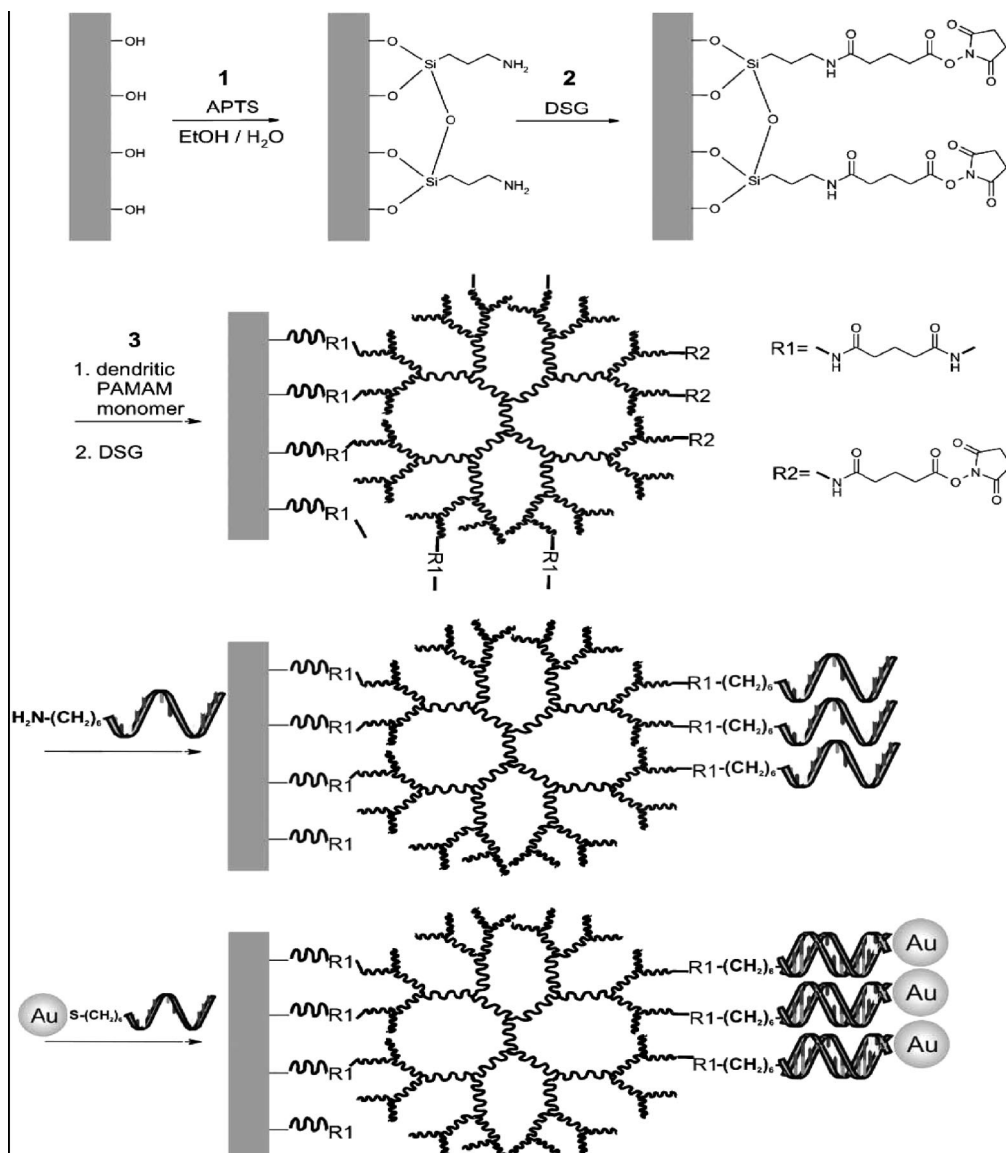


**Figure 23.** Schematic of the immobilization of gold nanoparticles by DNA hybridization on silicon dioxide surfaces. Hydroxy groups at the substrate surface condense with APTS to form aminosilylated surfaces. After treatment with the homobifunctional linker reagent DSG, the surfaces are activated for the coupling of dendritic PAMAM starburst monomers. This polymeric dendrimer thin layer is activated by further use of DSG for the covalent attachment of 59-aminofunctionalized DNA oligomers. Due to specific Watson–Crick base pairing, gold nanoparticles, functionalized with oligonucleotides of complementary base sequence, were immobilized on substrate surfaces. From ref 162. Reproduced by permission of The Royal Society of Chemistry.

electrocatalytic responses, by using Pt nanoparticles. Willner et al.<sup>199a</sup> showed that the hybridization-based binding of Pt nanoparticles to an electrode could evoke currents for the electrocatalytic reduction of H<sub>2</sub>O<sub>2</sub>. A similar aptamer-based recognition scheme was used to detect thrombin. Response amplification in DNA hybridization schemes can also be based on dissolution of the Au nanoparticles<sup>199b,c</sup> and changes in electrical conductivity of nanoparticle networks.<sup>199d</sup> DNA hybridization can also be used for building Au nanoparticle scaffolds, including preparation of conducting films. Niemeyer showed<sup>162</sup> it is possible to fashion a surface-attached monolayer of nanoparticles on an IDA using the specific binding properties of complementary oligonucleotide hybridization (Figure 23). The PAMAM dendrimer foundation to which the capture oligonucleotide was linked (in the third reaction) provided more coupling sites and an ultimately more dense coverage of the 15 nm diameter Au nanoparticles ( $\geq 850$  particles/ $\mu\text{m}^2$ ) than was achieved in previous work. The inherent flexibility of the

dendrimer structure may also have promoted higher coverage by allowing relief from steric interactions between adjacent nanoparticles. The ac impedance of the film conductivity showed that electron transport across it was a thermally activated process—without any evidence of concurrent ionic transport—with an activation barrier of 0.3 eV.

Another major point of interest is the electronic conductivity of nanoparticle films analytical in nature, as the electronic conductivity has been shown to be sensitive to the film's environment, including sorption of other chemicals from the gas phase. Wohltjen and Snow<sup>168</sup> airbrushed films of octanethiolate-protected Au MPCs onto a heated (120 °C) IDA device and tested the response of the films to vapor exposure (with the IDA at room temperature). The film conductivity decreased strongly in the presence of toluene and tetrachloroethylene, with a sensitivity suggesting sub-1 ppmv vapor detectability. The film's conductivity was, on the other hand, unresponsive to water vapor and only slightly responsive to propanol. The inference of these observations

was that sorption of the organic components into the MPC film was facile but that sorption of water into the strongly hydrophobic material was not.

Numerous subsequent papers have described effects of sorbed vapors on the electronic conductivity of MPC films, including in a gas chromatographic detector<sup>170a</sup> and responding to H<sub>2</sub> sorption by Pd nanoparticle films.<sup>170b</sup> The effects reported tend to be somewhat confusing, since some studies based on unlinked films describe decreases in electron hopping conductivity as vapors are sorbed,<sup>167,172,176–181</sup> while others report either increase or decrease depending on the particular vapor.<sup>168,173</sup> Films made from linked-together MPCs, on the other hand, rather uniformly display decreases in conductivity upon vapor sorption.<sup>167,172,176–181</sup> There is general agreement in these works regarding the importance of thermally activated electron tunneling and the idea that *decreasing* conductivity is consistent with increased core–core separations upon vapor sorption and swelling. There is, however, no generally accepted explanation for *increases* in conductivity caused by sorbed vapors. Effects of sorbed vapor on the dielectric permittivity of the nanoparticles (which would affect the charging energy or energy of reaction 16 involved in charge carrier generation) have been suggested,<sup>168,173</sup> and this parameter has been made part of a recent generalized theory<sup>169</sup> that is somewhat successful in accounting for conductivity responses across a range of 11 different organic samples. Another recently demonstrated<sup>165</sup> parameter is that of how the local mobility of MPC sites may change with sorption of organic vapor or CO<sub>2</sub> gas. Sufficiently large or frequent thermal motions that bring sites into closer proximity can result in faster electron hopping even though the average site–site distances have increased by swelling. In *unlinked* films, as a result, sorption causes an increase in electron hopping conductivity (rather than the decrease that swelling, without site local thermal mobility, would lead to). *Linking* the same MPCs together, on the other hand, so as to eliminate the local motions, reverses the response and leads to a conductivity decreasing with sorption. Thus, vapor responses must be understood in the context of whether a MPC film is linked or not, in addition to other local parameters that affect the intrinsic electron hopping probability.

## 5. Electrochemistry at Nanoscopic Electrodes

The voltammetric use of working electrodes with micrometer dimensions (commonly 1–25  $\mu\text{m}$  diameter) began<sup>200</sup> in the 1980s and has since become a major research area in electrochemistry.<sup>201–203</sup> The consequences of shrinking the working electrode are multiple. Several relate to the way that the electrical double layer capacitance ( $C_{\text{EL}}$ ) of an electrode, coupled with the uncompensated ionic resistance ( $R_{\text{UNC}}$ ) of the electrolyte solution, places limitations on electrochemical experiments. The small area of a microelectrode decreases  $C_{\text{EL}}$  and thus also decreases the time constant  $R_{\text{UNC}}C_{\text{EL}}$  on which the working electrode potential can be controlled, enabling experiments on the nanosecond time scale.<sup>204</sup> Smaller  $R_{\text{UNC}}C_{\text{EL}}$  values also open the way to experiments in media with very large  $R_{\text{UNC}}$ , such as solvents without deliberately added electrolyte<sup>205</sup> and ionic liquid semisolids.<sup>206,207</sup> The small electrode size additionally enables voltammetry in very small spaces, producing important openings to voltammetry<sup>208,1</sup> close to and even within single biological cells, and giving rise to the new and now widespread form of microscopy<sup>209–211</sup> called scanning

electrochemical microscopy (SECM). New hydrodynamic transport experiments<sup>212</sup> also came into existence. The faster radial diffusion flux to microelectrodes (relative to linear diffusion) can enhance current signal/noise ratios and benefit electroanalysis<sup>213</sup> at low analyte concentrations.

Some of these forms of microelectrode use and voltammetry will be featured in other articles in this review issue. The focus here will be on electrodes of *sub*-micrometer dimensions and in particular of dimensions in the smaller numbers of nanometers, popularly called nanoelectrodes. The first example was a nanoband, with 5–2300 nm widths and macroscopic lengths.<sup>214</sup> There are ample reasons for exploring these electrode dimensions, besides the further potential benefits to lowering voltammetric time scales and electroanalysis in smaller spaces. These include issues of transport within diffusion layers that have depths comparable to the double layer, the structure of the double layer itself, the reactant/product crowding attentive to acutely radial (fast) transport conditions, reactions of molecules with electrode interfaces of comparable dimensions, quantum size effects of smaller electrodes (akin to quantized double layer charging, QDL, see above), and a better understanding of the atomic-scale aspects of electrodeposition and corrosion.

### 5.1. Nanoelectrode Fabrication and Characterization

Progress in nanoelectrode research is, as one might expect, directly correlated to progress in fabrication and characterization. Electrode geometry and that of the insulating shroud surrounding the electrode are issues as important as actual electrode size, since they determine the mass transport of electrode reactants<sup>202,209</sup> and thereby the proper interpretation of currents and current–potential curves. Zoski<sup>202</sup> and Arrigan<sup>215</sup> have reviewed the different geometries and fabrication methods for microelectrodes (disks and other shapes such as bands and rings), and nanoelectrodes and arrays thereof, respectively. Methods producing single nanoelectrodes of submicron dimensions have been based on glass encapsulation,<sup>202,216,217</sup> micropipette pulling technology,<sup>218a</sup> electrochemical or chemical etching followed by photoresist, polyimide,<sup>218b</sup> Teflon,<sup>219</sup> or electrophoretic paint deposition.<sup>220–223</sup> carbon nanotubes both multi-<sup>224</sup> and single-walled,<sup>225</sup> and carbon nanotube and etched metal array electrodes.<sup>225,226</sup> Arrigan<sup>215</sup> provides a convenient summary of many of these methods and their products. Cylindrical nanoelectrodes have also been reported,<sup>222</sup> using single multiwalled carbon nanotubes which were immersed to various depths in electrode/redox sample solution and which produced radial-transport controlled currents.

The ideal shape of a microelectrode, and a nanoelectrode, from the viewpoint of uniform flux of mass transport of reactants to it and uniform current density across its electrode/electrolyte interface, is a perfect hemisphere, surrounded by a flat shroud at the level of the hemisphere's rim. For a band electrode, the ideal geometry is a hemicylinder bounded by a flat insulating (shroud) surface. Experimental deviations from this geometry may include flattening of the hemisphere electrode by various degrees, an oval rather than circular electrode shape, and irregular roughening. The insulating shroud may be flat on one side and not the other, or it may have a rim protruding above the working electrode. The latter "shroud effect" can decrease nanoelectrode currents by shutting off radial lines of mass transport. In the limit, a protruding shroud's rim around the electrode forms a

cylindrical pore with the working electrode at the bottom, and mass transport becomes linear rather than radial. In another extreme shroud geometry, a larger diameter “lagoon” of solution is formed under a pore mouth; this can, if overlooked or ignored, lead to suspected orders-of-magnitude overestimation of electron transfer rate constants.<sup>227</sup> Some of these nonideal geometries can be useful rather than deleterious, for example in creation of ultrasmall collection/generation cells for single molecule experiments<sup>228</sup> and in design of model nanopore structures,<sup>229</sup> as discussed later.

The various geometrical aspects of micro- and nanoelectrodes are products of their fabrication. Nonideal geometries (or undesired ones) are more serious at the nanoscale because geometrical effects on mass transport become amplified there (and perhaps other geometry-related aspects of electrochemical reactions are amplified as well, although that is a less understood subject at present). The effects of undesired geometries are also more serious at the nanoscale because microscopy of any sort, including scanning electron microscopy (SEM), becomes of limited quantitative usefulness at nanoscopic dimensions, when one wishes to (a) exactly define the edges of objects, (b) reveal contours and topology, and (c) apply it nondestructively to dozens of fabricated electrodes. SEM has been valuable for characterizing the larger of nanosized working electrodes but diminishes in usefulness at the several nanometer dimensions.

A variety of methods have been employed to assess electrode geometries at the micro- and nanoscale. None are trivial to implement, especially for nanoelectrodes. Judging a nanoelectrode radius ( $r$ ) from a limiting current using the microelectrode hemisphere equation,<sup>36</sup>

$$i_{\text{LIM}} = 2nFDC^{\text{BULK}}r \quad (18)$$

where  $D$  and  $C$  are the (known) diffusion coefficient and concentration of a redox probe, implicitly assumes the hemispherical shape. If the electrode is recessed (i.e., protruding shroud around the electrode rim), the current will be depressed and the values of  $r$  and current density underestimated and overestimated, respectively. Responses more explicitly responding to electrode and shroud shape are required for adequately thorough nanoelectrode characterization. This problem has been addressed in the context of SECM by Bard and co-workers,<sup>202,209</sup> based on approach curves, which are measurements of the limiting current of a redox probe as the electrode is brought to within diffusion layer distances of insulating (blocking) or conducting (feedback, under potential control) surfaces. The profile of current against distance is sensitive to the degree of radial transport to the working electrode tip, and inferences about its shape can be obtained by comparing current–distance data to mass transport computations for different geometries. Such information can also be obtained from approach curves within an electroactive medium, such as a Nafion film containing an electroactive counterion.<sup>230</sup> These ideas have been applied particularly thoroughly to nanoelectrode characterization by Fan et al.<sup>231</sup> and by Mirkin.<sup>232–234</sup>

Another important measurement is of the actual, microscopically electrode area. White et al.<sup>221</sup> introduced an elegant method in which a monolayer of the complex bis(2,2′-bipyridine)chloro(4,4′-trimethylenedipyridine)osmium(II) is adsorbed on the (Pt) electrode (Figure 24) and the charge ( $Q$ ) associated with the Os<sup>III/II</sup> oxidation is measured in fast-scan ( $10^3$  V/s) voltammetry. This measurement gave surface

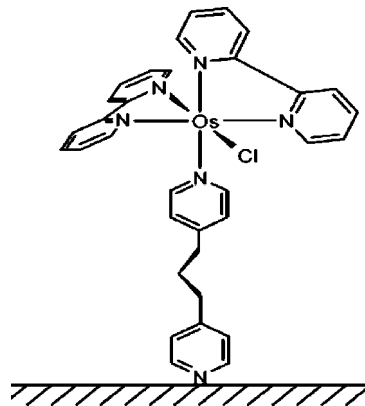


**Figure 24.** Schematic depiction of the adsorption of  $[\text{Os}(\text{bpy})_2(\text{dipy})\text{Cl}]^{1+}$  at the Pt/electrolyte interface. Reprinted with permission from ref 221. Copyright 2003 American Chemical Society.

areas as small as  $\sim 10^{-10}$  cm<sup>2</sup>, for a  $\sim 60$  nm radius electrode, corresponding to as few as  $\sim 7000$  copies of the complex. Criteria were developed to distinguish hemispherical nanoelectrodes from those which are not or which have protruding shrouds.

## 5.2. Nanoelectrode Properties

The increased radial mass transport flux at a nanoelectrode (as compared to macro- or microelectrodes) aids the competition between mass transport and electron transfer control of current, which in principle allows measurements of faster electron transfer processes at the electrode/electrolyte interface. In one early example of nanoscopic electrodes, Lewis et al.<sup>216</sup> reported heterogeneous electron transfer rate constants for ferrocene<sup>1+/0</sup> of 220 cm/s (at a 1.6 nm radius electrode, in CH<sub>3</sub>CN) and for Ru(NH<sub>3</sub>)<sub>6</sub><sup>3+/2+</sup> of 79 cm/s (at a 1.1 nm radius electrode, in water). These reaction rates are extremely high as compared to any preceding or since-reported rates. This work preceded the research on nanoelectrode shape and size characterization issues noted above and was particularly scrutinized<sup>227</sup> in a discussion of effects of recessed nanoelectrodes and lagooning.

Other early nanoelectrode work<sup>235–237</sup> employed nanoband electrodes, fashioned by exposing the edges of thin metal films sandwiched between insulators. The attractive  $R_{\text{UNC}}C_{\text{EL}}$  property of a 20 nm-wide nanoband enabled<sup>237</sup> voltammetry at temperatures as low as 88 K. Nanobands offer increased currents (by virtue of length) but fast radial transport (by virtue of narrow width). The validity of the equation for limiting currents at microband electrodes

$$i(t) = \frac{nFDlC^{\text{BULK}}\pi}{\ln\left[\frac{4Dt}{r_0^2}\right]} \quad (19)$$

where  $r_0$  and  $l$  are band radius and length, respectively, has been established.<sup>238</sup> The current is predicted to be time-dependent, but the form of the equation means that, in practical terms, especially at small  $r_0$ , the time dependency is slight.

Quantitative study of nanoband currents<sup>235,236</sup> indicated a deviation from the above mass transport equation at very small electrode widths. Nanobands thicker than  $\sim 20$  nm gave limiting currents for the oxidation of ferrocene that followed the mass transport relations anticipated for the hemispherical nanoband electrode geometry, while thinner nanobands gave



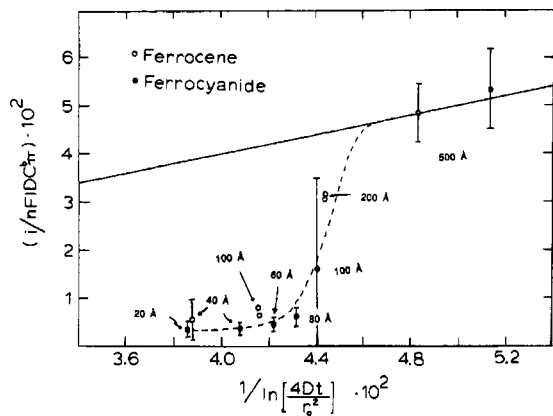


**Figure 25.** Plot of normalized limiting current  $(i/nFIDC\pi) \cdot 10^2$  vs  $\{\ln[4Dt/r_0^2]\}^{-1}$  obtained at Pt and Au band electrodes. Solid line (slope = 1) corresponds to eq 1. Dashed lined drawn through experimental points obtained for the oxidation of 1–10 mM ferrocene (○) in acetonitrile (0.1 M  $\text{Bu}_4\text{NClO}_4$ ) and 1–10 mM ferrocyanide (●) in  $\text{H}_2\text{O}$  (0.1 M KCl). Electrode widths are indicated on the plot. Reprinted with permission from ref 235. Copyright 1987 American Chemical Society.

currents much smaller than predicted (Figure 25). The uncertainties of electrode shape were acknowledged; a  $>5$  nm wide nanoband may be interrupted by occasional gaps along its length, but it was appropriately argued that such gaps do not destroy the explicit intensity of the radial diffusion field from its sides.

The currents plotted in Figure 25 were measured<sup>235</sup> at a fixed time after a potential step, for two different redox probes in two different solvents. The sharp diminution of current for the smallest electrodes was the first evidence for a change in mass transport at nanoscopic electrodes at molecule-sized distances. Examination of the possible underlying factors included changes in solvent viscosity at near-surface distances, changes in near-surface concentrations owing to double layer electric field effects on ionic reactants, and interruption of molecular flux when the similarity of electrode reaction space and reactant size requires some kind of serial access to the surface. The last point is simply that current flux cannot increase beyond the instant dimension that each reactant requires for electron transfer with the electrode. This notion was supported by comparison of reactants having different radii. Lemay et al.<sup>239</sup> have reported further observations bearing on the crowding of motions of charged species near a nanoelectrode and have raised a further point,<sup>240</sup> specific to single walled carbon nanotubes used as electrodes, of the effect(s) of their nonuniform densities of electronic states on the currents observed in electrochemical processes. The latter has been probed<sup>241</sup> by observing deposition of metal nanoparticles onto single walled carbon nanotubes used as electrodes.

Further theoretical study of size effects has included the effect<sup>242</sup> of the electrode double layer field on transport to nanoscopic electrodes. When the Debye length  $\kappa$  becomes comparable to or greater than the diffusion depletion length, the transport flux of the reactant can be depressed or accelerated, depending on reactant charge and sign of the electric field. This is a kind of nanoscopically induced Frumkin effect.<sup>37</sup> The nanoradial dispersion of the diffuse double layer tends to compress it, which lessens the effect, but nonetheless it is made clear that the ionic space charge effect around a nanoscopic electrode can have major effects on its reaction flux and consequent current. The authors point out the implications for reactions involving metal colloids,

which were encountered in much later work.<sup>60</sup> The 2–150 nm radius nanoelectrodes were applied<sup>221</sup> to measurement of the electron transfer rate constant for ferrocenylmethyltrimethylammonium in aqueous medium; the  $4.8 \pm 3.2$  cm/s result was close to other literature on ferrocene but much smaller than that reported by the earlier<sup>216</sup> study. Experiments on thoroughly characterized (by shape and size) nanoelectrodes have also produced<sup>234,243</sup> smaller rate constants for both the ferrocene (ferrocenemethanol, 7 cm/s) and the  $\text{Ru}(\text{NH}_3)_6^{3+/2+}$  reactions (17 cm/s). The maximum observable rate constant might<sup>244</sup> actually be in the lower range. These reports underscore the importance of characterizing both nanoelectrode and shroud size/shape.

Observing voltammetric reactions in the absence of the traditionally added supporting electrolyte is another opening into the study of basic electrochemical phenomena provided by small working electrodes and has been pursued by a number of workers. The  $iR_{\text{UNC}}$  electric field that develops when electrolyte ions are absent (or scarce) extends over macroscopic distances, so that coupling of diffusion and migration effects in transport rates becomes observable<sup>220,245–247</sup> even at micrometer-sized working electrodes. Kucernak showed how<sup>220</sup> to make carbon nanoelectrodes over a range of sizes, and down to about 1 nm radius, and found profound effects on transport rates and apparent reversibility over a variety of redox couples. The effects were discussed in terms of the dynamic double layer effect, a kind of super-Frumkin effect in which not only concentrations but also transport rates of electrodes reactants are affected by the extensive electrical field developed in the absence of electrolyte. These ideas were recently extended<sup>248</sup> to note that electroneutrality effects in depletion layers at nanometer scale electrode/electrolyte interfaces can cause voltammetric responses to vary with electrode size, reactant charge, formal redox potential, and compact layer dielectric properties.

Further work<sup>223</sup> on the oxidation of  $\text{IrCl}_6^{3-}$  in aqueous medium, comparing nanoelectrode voltammetry obtained with varied levels of supporting electrolyte concentration, found that, irrespective of electrode radius, at low electrolyte concentrations (a) this couple's formal potential ( $E^0$ ) was shifted positively by electrolyte owing to differences in ion pairing interactions for the redox partners and (b) its heterogeneous electron transfer rate constant was sharply decreased. Subsequent work suggested<sup>222</sup> that measuring the dynamics of ion-pairing interactions might be possible using nanoelectrode voltammetry. This study provides a good illustration of the complexity of reactions of highly charged species in the presence of low concentrations of supporting electrolyte.

When you have a tool designed for small things, its ultimate use is observing a single, isolated molecule. A classical strategy<sup>249</sup> in single molecule observations is to somehow isolate and observe a very small volume segment of a dilute solution, aiming at residency of a single molecule or only a few molecules therein. A variety of small-volume isolation tactics have emerged, some based on electrochemistry. Fan and Bard<sup>228,250,251</sup> showed that a nanoelectrode with a soft (deformable), protruding shroud can be used to isolate a small solution volume in an SECM approach experiment by pushing it against a second, flat, electrode substrate (Figure 26). With the nanoelectrode and substrate potentials biased as in a collector-generator, or positive feedback, mode, the current flowing due to entrapment of a single molecule becomes amplified by repeated recycling

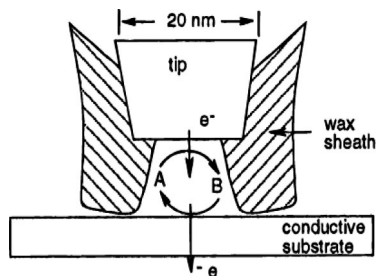


**Figure 26.** Single-molecule detection with the SECM. Molecule A is trapped between the tip and surface. Reprinted with permission from ref 228. Copyright 1996 American Chemical Society.

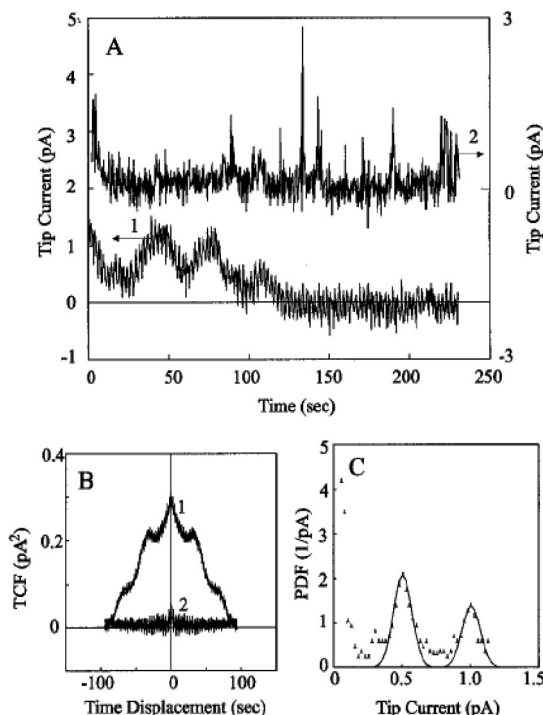


**Figure 27.** (A) Curve 1: Tip current with time for a solution of 2 mM CpFeCpTMA<sup>+</sup> and 2.0 M NaNO<sub>3</sub> with a Pt–Ir tip at 0.55 V vs SCE and an ITO substrate at –0.3 V; *d* = 10 nm. Curve 2: Time series of the tip current for *d* within the tunneling range in a solution containing only 2.0 M NaNO<sub>3</sub>; tip radius 7 nm. Data sampling rate 0.4 s per point. (B) Corresponding time correlation functions. (C) Probability density function of time series 1 in panel A. Reprinted with permission from ref 228. Copyright 1996 American Chemical Society.

between its oxidation states. The amplification was estimated to be  $\sim 10^6$ -fold, and the estimated single molecule current of  $\sim 1.6$  pA was indeed not far from actual observations, as illustrated by the current peaks in Figure 27, panel A, curve 1. The slow rise and fall of currents was ascribed to slow drift of the electrode tip toward and away from the n-TiO<sub>2</sub> substrate.

Procedures and theory for characterization have recently appeared<sup>233</sup> for nanoelectrode disks that (by careful etching of the Pt disk) are very slightly recessed (small numbers of nanometers). Such well-defined protruding shroud geometries would seem to be appealing for further single molecule-type experiments and other circumstances requiring isolation of a very small volume of electrode reactant. In current work,<sup>252</sup> the recessed electrodes have been used as SECM tips which when immersed in a mercury pool produce a thin layer cell which can contain from one to a few thousand redox

molecules. Steady-state voltammograms of  $\geq 1$  molecules have been observed for a variety of neutral and charged redox species.

Another single molecule strategy built on small observation volumes should be mentioned (albeit one not using a nanoelectrode but a microelectrode). Electrogenerated chemiluminescence (ECL)<sup>253</sup> occurs when energetic electron donors and acceptors are, by suitable electrolytic means, cogenerated within a working electrode's diffusion layer and react with one another to produce an excited-state product, such as D\*, which luminesces.



If the ECL process is efficient, and a reductive potential pulse following an oxidative one is executed on a sufficiently short time scale, the volume of the diffusion layer containing D<sup>–</sup> and A<sup>+</sup>, and the flux of D<sup>–</sup> + A<sup>+</sup> reactions, is small enough that individual excited-state emissions can be detected<sup>254</sup> by suitable single photon counting detection.

Nanoelectrode ECL can also be used as a light source, which because of its small size approximates a point source. Several publications have taken successfully accomplished imaging experiments based on this idea. Bard et al.<sup>255</sup> evoked ECL emission at electrodes with effective diameters down to 155 nm to carry out near-field scanning optical microscopy imaging measurements. Wightman et al.<sup>256</sup> used ECL emission at a ca. 500 nm radius electrode tip as a light source for scanning optical microscopy, attaining light transmission images with a resolution of about 600 nm.

A further example of small space analysis where nanoscale electrodes provide a benefit is in monitoring of exocytosis of dopamine release from biological nerve cells. Cheng et al.'s<sup>257</sup> use of a carbon fiber nanoelectrodes with a 100–300 nm tip diameter produces improved spatial resolution of the vesicular release event at the cell membrane. Mirkin et al.<sup>258</sup> have penetrated mammalian cells with 42 nm diameter nanoelectrodes and report voltammetry inside.

Other types of nanoscale electrochemistry involve using nanoscopic tips in scanning and imaging, as in SECM and electrochemical STM and AFM. Those fields are beyond the scope of this review, but a few contemporary examples will be mentioned. Resolution will of course be enhanced in SECM by the use of smaller probe tips, as shown by Schuhmann et al.<sup>259</sup> Unwin and MacPherson et al.<sup>260</sup> have described methods for the production of metal nanoelectrodes based on use of electrophoretic paint and on using single-walled carbon nanotubes on the tips of AFM probes as templates. Penner<sup>261</sup> has deposited 10–60 nm wide nanoparticles of poly(aniline) by appropriate potential pulsing of a Pt STM tip at an HOPG graphite surface. The experiments were aimed at improving understanding of PANI nanoparticle growth mechanisms. Previous, similar experiments had been developed<sup>262</sup> for depositing nearby 10–20 nm Cu and Ag nanoparticles on HOPG, subsequently observing their spontaneous galvanic reaction with one another to produce a Cu coating on the Ag nanoparticles. Crooks<sup>263</sup> demonstrated the electrochemical basis for STM tip-induced removal of organic monolayers from Au(111) surfaces; water condensation from humid air and capillary forces fill an ultrathin electrochemical cell between the tip and surface. Surface features as small as 10 nm could be generated in the organic monolayer. Using a Ag-coated STM tip, analogous electrochemistry could be carried out<sup>264</sup> to fill features in the monolayer with Ag nanoparticles deposited on the exposed nanopatch of Au(111).

STM tips<sup>265–268,267,270</sup> and SECM tips<sup>271</sup> can also be used for investigation of individual metal nanoparticles that had been deposited with the tip. These studies open the way to a more exacting interrogation of the dependence of electrocatalytic reactions occurring on the nanoparticles, on their size.

## 6. Electrochemistry at Single Nanopores

Electrochemistry at (of) nanopores, broadly conceived, includes (a) detection of charge flow through nanopores in membranes dividing two electrolyte solutions (membrane ion currents), (b) detection of transport to/from nanoelectrodes lying at the bottom of nanopores (nanopore electrodes), and (c) electrophoretic and electroosmotic transport of solvent and ions, as occurs in nanochannels when a voltage bias is imposed at the channel ends. (Nanoelectrospray mass spectrometry<sup>272</sup> is a distant cousin, since the ion source tips have larger orifices). Either circumstance may refer to concurrent transport through multiple nanopores and nanochannels.

This review will be substantially confined to experiments on single nanopores. The extensive work by Martin et al. and others on arrays of nanopores has been reviewed.<sup>273–276</sup> Transport related to nanofluidics will not be covered. Aside from the well-established area of ion channel formation<sup>273,277,278</sup> in lipid bilayer membranes, only recently have fabrication techniques appeared that allow experiments on *single* nanopores of a few nanometer diameter—i.e., of molecular dimensions. Single nanopores in membranes have been made using multiwalled 150 nm diameter carbon nanotubes (cnt) embedded in an epoxy membrane as the nanopores,<sup>279–283</sup> by milling nanometer-size holes in silicon nitride and SiO<sub>2</sub> membranes with ion<sup>284–287</sup> and electron<sup>288,289</sup> beams, by templating 0.5–2  $\mu\text{m}$  nanopores with a glass fiber embedded in an electroplated Au membrane,<sup>290</sup> by lithographic and electron beam procedures that formed a SiO<sub>2</sub> nanopore,<sup>291</sup> by track etching a polymer membrane with a single heavy ion,<sup>292</sup> and by laser ablation of a mica membrane.<sup>221</sup> Electroporation, the formation of a transient nanopore in a biological cell membrane for the injection of molecular probes, can be assisted<sup>208</sup> by pushing a 770 nm i.d. glass capillary against the cell wall prior to application of a voltage pulse. Kasianowicz and Deamer<sup>293–295</sup> describe the use of  $\alpha$ -hemolysin as a nanopore ion channel to detect transit of nucleic acids, and Kasianowicz<sup>291</sup> has embellished the formation of analytically useful ion channels in lipid bilayers with novel polymer chain threading ideas. Bayley and Martin<sup>270</sup> have reviewed the area of ion channels for detecting nucleic acids and other biologically relevant compounds, and Dekker<sup>296</sup> has reviewed developments in solid state (as opposed to lipid bilayer ion channels) nanopores. The technology impetus<sup>297</sup> given by the prospects of detecting and sequencing oligonucleotides and DNA chains by characteristics of their passage through nanopores has stimulated interest in fashioning of single nanopores in robust membranes. Imaging of individual nanopores by SECM has been reported,<sup>298–300</sup> including those in human skin.<sup>301</sup>

Nanopore electrodes have principally been fashioned by procedures that make enshrouded nanoelectrodes,<sup>229,233</sup> followed by controlled etching of the nanoelectrode. A new form of nanopore array<sup>302,303</sup> electrode was based on nanoporous opal films of 440 nm silica spheres.

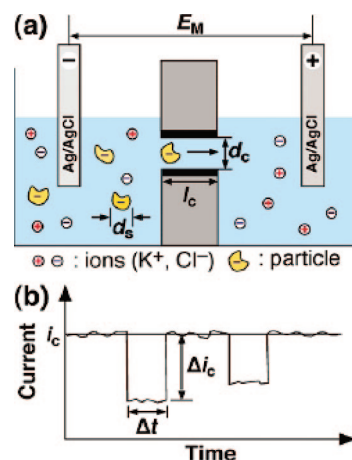


**Figure 28.** (a) The general experimental approach for electric field-driven Coulter counting. A membrane containing a single channel divides two chambers containing an electrolyte solution. When an appropriate potential is applied across the membrane, an ionic current is driven through the channel. If particles of an appropriate size and charge are present, they will enter the channel and reduce the ion current. (b) Coulter counter data consist of a series of current pulses associated with the presence of particles within the channel. The height of the pulse,  $\Delta I_C$ , is related to particle size, and the width,  $\Delta t$ , corresponds to the particle transit time. In favorable cases, data such as these can provide information about the size, charge, and concentration of the particles. Reprinted with permission from ref 279. Copyright 2004 American Chemical Society.

### 6.1. Single Nanopores in Membranes

The most common experiment done with single nanopores in membranes is illustrated<sup>279</sup> by Figure 28. The membrane is bounded by two electrolyte solutions, one of which contains a species of interest (shown here as a nanoparticle, but it can be anything with a dimension that approaches, or at least is not insignificant in relation to, the nanopore diameter). Some form of electrochemical excitation is applied to the electrodes—a dc or ac potential, or a current—such that ionic charge is induced to flow through the nanopore. The value of the ionic current is determined by the electrolyte, its concentration, the applied potential, and the width and length of the nanopore—which acts as a resistive element. The ionic current is also sensitive to the pore shape; for example, conical pores yield much higher ionic currents<sup>289,304</sup> than do cylindrical ones of diameter equal to the small end of the conical pore. When a nanoparticle or molecule enters the nanopore, the ionic current is attenuated by an amount and with a duration and frequency related to the concentration, charge, and physical size of the nanoparticle in relation to the nanopore diameter and length. When the membrane contains a single nanopore, the change in ionic current signals (usually) passage of a single nanoparticle or other sample molecule. When the membrane contains an array of nanopores, passage of single molecules cannot be resolved, but the continuum of ionic current is nonetheless sensitive to multiple momentary blockages by the flux of transiting molecules<sup>273,305</sup> and thereby to their concentration. An important variant of the Coulter experiment is “capture and release”, where the nanopore is too small to accommodate the blocking species (a nanoparticle or polymer bead).<sup>306</sup> Ion flow attenuation is sensed as the nanoparticle occludes the nanopore mouth, and then the nanoparticle is released by reversing the potential bias applied to the nanopores. While there is general appreciation in the single nanopore community about the value(s) of nanopore chemi-



cal functionality, for more selective single molecule detection, with the exception of engineered hemolysin channels in lipid bilayers, single nanopore structures reported thus far have not yet achieved the chemical diversity that has been developed for nanopore arrays.<sup>273,302,303</sup>

The experiment in Figure 28 was invented by Coulter over a half-century ago as a highly successful and commercialized device for counting the population of biological cells in a suspension. The procedure is often called a Coulter Counter experiment, and its essential features and evolution have been lucidly summarized by Crooks<sup>279</sup> for single pore experiments and by Bayley and Martin<sup>273</sup> for experiments with arrays of nanopores. The distinction between a single pore Coulter Counter and detecting transport of individual species through ion channels in lipid bilayers has become somewhat artificial given that the pores in the former have become shrunk to molecular dimensions.

The interiors of multiwalled carbon nanotubes (cnt's) are thought to be atomically smooth, uncharged graphitic sheets and thus might approximate an ideal cylinder for forming a single nanopore. Sun and Crooks<sup>279</sup> embedded single cnt's in epoxy blocks and then prepared membranes penetrated by the single cnt by microtoming, mounting the membranes on silicon nitride membrane supports. Opposite ends of the cnt were exposed to pH 7 0.1 M KCl electrolyte solutions, one of which also contained either nominally neutral 60 nm diameter polystyrene beads or 100 nm diameter beads with  $\text{-CO}_2\text{H}$  surface functionalities. Electrophoretic transport of the latter occurred stochastically (Poisson statistics) through the cnt pore and was detected as ionic current blockages (Figure 28). Under low potential bias, transit of the smaller polystyrene bead was slow enough to approximately resolve the transit time (ionic current blocked for a few milliseconds).

The preceding experiment was later refined<sup>281</sup> so as to reduce the S/N ratio and improve the time resolution for passage of 57–60 nm diameter polymer beads, of varying levels of  $\text{CO}_2\text{H}$  surface functionalization, through 132 nm diameter cnt nanopores. The magnitude of the pulse of the ion current depression responds to the nanobead diameter, and assuming solely electrophoretic transport through the cnt (no electroosmotic flow, since the cnt walls are uncharged), the nanobead transit time (electrophoretic mobility) gave a collective surface charge on the nanobead  $Q = 91 \text{ nm}^2/\text{CO}_2^-$  surface charge, that was close to the nanobead manufacturer's specification (by titration) of  $85 \text{ nm}^2/\text{surface charge}$ . (Such agreement was not obtained, however, for nanobeads with higher densities of  $\text{CO}_2\text{H}$  groups; among the reasons discussed was incomplete ionic screening).

The polymer nanobead samples were not monodisperse in size and overall surface charge, and since they are individually detected, the distribution of sizes and charge could be determined.<sup>281</sup> Rather good agreement was obtained in size comparison determinations<sup>283</sup> by the cnt nanopore experiment, transmission electron microscopy (TEM), and dynamic light scattering (DLS). There are subtle, somewhat complementary distinctions between the different methods; the cnt nanopore experiment on nanobeads with low surface charge density gives a distribution of individual hydrodynamic diameters, whereas DLS gives an averaged value and TEM images portray the dehydrated diameter.

The study of ion channel nanopores was given an important boost by Kasianowicz, who in collaboration with Deamer<sup>293,295</sup> showed that the relatively stable, 2.6 nm channels formed by heptamers of  $\alpha$ -hemolysin in lipid

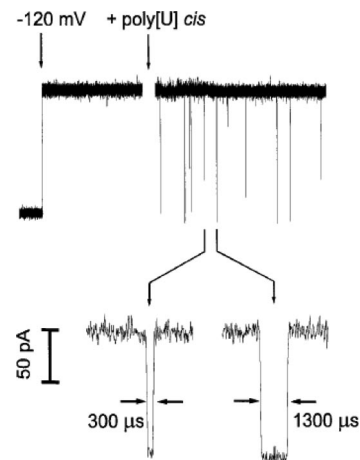


**Figure 29.** Oligomers of poly[U] caused transient blockades in the  $\alpha$ -hemolysin single channel current. At the first arrow, a potential of  $-120 \text{ mV}$  was applied across the membrane. This voltage caused a continuous current of  $-120 \text{ pA}$  to flow. At the second arrow, poly[U] of mean length 210 bases was stirred into the negative potential compartment to a final concentration of  $0.1 \text{ mg/mL}$ . The polynucleotides caused short-lived current blockades. The inset (expanded time scale) shows two typical blockades with lifetimes of  $300$  and  $1300 \mu\text{s}$ . Reprinted with permission from ref 293. Copyright 1996 National Academy of Sciences.

bilayers could, under a potential bias, accommodate passage of single stranded RNA and DNA, producing as they did so recognizable ion current blockages. The homopolynucleotide polyuridylic acid (poly[U]) was used as a test molecule, having minimal secondary structure and base pairing. Poly[A] and poly[T] showed similar behavior; sometimes a strand would exhibit longer blockages, symptomatic of pore blockages possibly due to secondary structure; these could be cleared by reversal of the potential bias. Figure 29 shows examples of the ion current blockades, which gave histograms of transit times peaking at 92, 290, and 1288 microseconds. The two longer transit time histograms contained approximately even numbers of transit events and were related to polymer length and inversely to applied potential, whereas the shorter time did not respond to those parameters. It was attributed to a transient interaction of the oligonucleotides with the nanopore, failing to transit through it. The reason(s) for the two equally probable slower transit times might be connected to different ends of the chain first entering the nanopore. The suggestion was clear that this experiment has promise for determining the chain length and even the sequencing of oligonucleotides.

Subsequently, Kasianowicz<sup>294</sup> showed how  $\alpha$ -hemolysin nanopores in lipid bilayers could be used to “image” the mass of pore-transiting poly(ethylene glycol) molecules and as reporters of pore-transiting DNA polymers of the selective binding of other analytes to the DNA. In the latter study, in the absence of analyte, chains bearing analyte binding sites freely transit the nanopores and cause short-lived blockades of the ionic current whose frequency is proportional to the free chain concentration. When the polymer chain becomes bound to an analyte, the blockage frequency is lowered, or both lowered and blockade time lengthened according to the mean duration of the polymer/analyte binding. Further, because different DNA polymer chains have different lifetime themes, multianalyte detection schemes become imaginable. These ideas were substantially illustrated with experiments. These reports showed how nanopore transit can be linked

both directly and indirectly to the concentrations and properties of a number of neutral and nontransiting species.

Deamer<sup>295</sup> has reviewed the flurry of investigations that followed the preceding report.<sup>293</sup> Much is being learned about the structural complexities of a complex—structurally and dimensionally—DNA molecule entering the structurally complex topology of  $\alpha$ -hemolysin nanopores. This continues to be one of the more exciting areas of nanopore electrochemistry. It invites application of potential excitation patterns as alternative probes of nanopore transit time and frequency.

Single nanopores can also be formed in polymer films by micromolding and single track etching. Micromolding gave relatively large pores (200 nm diameter), which nonetheless gave evidence of DNA ion current blockage events.<sup>307</sup> Single nanopores have been made by impact of single energetic heavy ions on polyethylene terephthalate<sup>308</sup> and Kapton<sup>292</sup> polymer films, followed by chemical etching of the latent ion track. The size and shape of such pores are manipulable by the details of the etching treatment; a conical shape gives lower nanopore resistance (higher ion currents). Conical nanopores are also “rectifying” voltage gates,<sup>308a</sup> meaning that the magnitude of the electrolyte ion current can depend on its direction through the narrow end of the cone—an effect suggested to be associated with the surface charges there. White<sup>308b</sup> has shown by detailed simulations that ion current rectification in conical-shaped glass nanopores instead, and in agreement with earlier more qualitative suggestions,<sup>308c</sup> reflects a voltage-dependent solution conductivity in the vicinity of the pore mouth.

The polyimide Kapton 50 HN (DuPont) gave<sup>292</sup> very stable ion currents. The small and large ends of the  $\sim 10\ \mu\text{m}$  long conical nanopores were 2–7 nm and  $\sim 2\ \mu\text{m}$ , respectively, and 4 nm was selected as optimum for the small end for ds DNA observations. A histogram analysis of an extended record of ion current blocking responses is shown in Figure 30A, where the DNA sample was a mixture of 284 bp and 4.1 kbp strands. The histogram peak at shortest blocking times was invariant with experimental conditions and was interpreted as a transient, unfruitful interaction of DNA with the pore. The longer time histogram maximum (0.4 ms) is in reasonable agreement with experiments using  $\alpha$ -hemolysin ion channels on DNA fragments of similar length. Much longer blocking times observed (not shown) were attributed to the 4.1 kbp fragment. Figure 30B shows another histogram record of blocking times for a more complex mixture of DNA chain lengths.

50 nm diameter nanopores formed<sup>291</sup> by a lithographic procedure in  $\text{SiO}_2$  membranes were also roughly conical with a length of  $\sim 50$ –60 nm of the small end. Translocation events of 200 bp ds DNA seen in the ion currents are unusual by being momentary increases in current, rather than depressions, as usually is observed. The authors interpret the effect as reflecting an interaction between the highly charged ds DNA and the high population of cations resident—owing to the  $\text{SiO}_2$  surface charge—within the channel. Dekker et al.<sup>309</sup> have reported evidence that surface charges within the channel can vary with the electrolyte employed.

Substantial interest in solid-state techniques for preparing robust nanopores has emerged. Golovchenko<sup>285</sup> described a new approach to making nanometer-sized nanopores in silicon nitride membranes based on low energy ion beams (“ion-beam sculpting”). The authors concluded from pore-shrinking effects that the ion-sputtering was accompanied

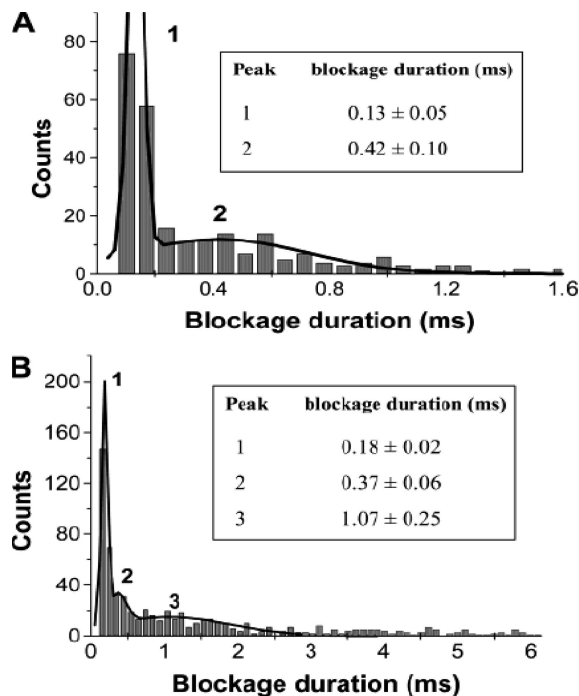


**Figure 30.** Histograms of ds DNA blockage durations in 1 M KCl, pH 7.2, 0.01% Triton-X100. Panel A. Solution on the small-pore side of the membrane contained 284 bp and 4.1 kb ds DNA fragments. The histogram has been fitted with the sum of two Gaussians. Panel B. Solution containing a mixture of blunt-ended 286, 974, and 4126 bp DNA fragments; histogram fitted with three Gaussians. Reprinted with permission from ref 292. Copyright 2004 American Chemical Society.

by a flow of matter to the pore, stimulated by the ion beam parallel to the surface. Volcano-like ridges could be formed.<sup>284</sup> When used as a membrane separating electrolyte solutions, intermittent ionic conductivity blockages of a 5 nm diameter nanopore were seen when double stranded 500 bp DNA was added to one of the solutions. Subsequent investigations<sup>286</sup> of detection of DNA transiting molecules have been aimed at folding phenomena and blockage distinctions based on DNA chain length and on unraveling the details of transit by trapping single molecules.

Letant et al.<sup>287</sup> also used focused ion milling to drill holes in a silicon membrane, followed by deposition of a ring of  $\text{SiO}_2$  around the pore, shrinking it to a 50–500 nm diameter. The  $\text{SiO}_2$  ring could be derivatized using silane chemistry and further functionalized with ssDNA probes. Both cylindrical and conical nanopores could be formed. While ion current measurements were consistent with the DNA functionalization, no blockage data were reported.

Timp et al.<sup>289</sup> used a tightly focused electron beam to form single 0.5–1.6 nm diameter pores in a 10 nm thick silicon nitride membrane. Nanopores this small provoke substantial wall effects. When the membrane is used to separate aqueous KCl solutions, its ion conductance is initially very low; many hours pass before the pore is wetted—and the interfacial material solvated—and conductance rises to a reproducible and repeatable value. The observed pore conductance is depressed below the bulk solution value when the Debye length is comparable to or less than the pore radius. Supported by theoretical modeling, the effect is due to the negative charges of the pore walls. (There is parallel interest<sup>310</sup> in the effects of charge of nanochannel walls on electrokinetic behavior, where effects are seen even for 70

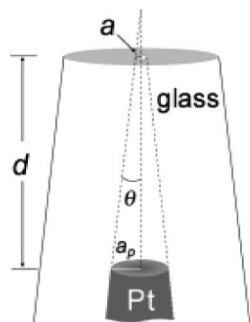


**Figure 31.** Drawn-to-scale schematic of a nanopore electrode characterized as having a nanopore orifice = 96 and 827 nm diameter electrode recessed by 5.96  $\mu\text{m}$ . Reprinted with permission from ref 229. Copyright 2006 American Chemical Society.

nm deep nanochannels at sufficiently low electrolyte concentrations).

Further detailed work<sup>288</sup> has been initiated to better understand the process of nanopore formation by electron beam milling of silicon nitride and  $\text{SiO}_2$  membranes. It was concluded that the nanopores have wedgelike edges. Understanding such geometrical details is evidently as important to proper interpretation of charge transport through nanopores, as protruding shrouds are to interpretation of currents at nanoelectrodes (*vide supra*).

Most (nearly all) of the information in the above reports about the dimensions and shapes of nanopore openings have come from imaging by TEM and SEM. The SECM has strong sensitivity to shape and dimension, as noted above regarding studies of nanoelectrodes, and has accordingly been applied to nanopore imaging. These reports include imaging of individual pores in track-etched membranes whose pores are filled with a solution of electroactive probe,<sup>212</sup> imaging of the same effect but when stochastically blocked by electrophoretic capture of nanoparticles at the nanopore mouth,<sup>311</sup> imaging of diffusive and iontophoretic transport of a redox species into pores in human skin,<sup>301</sup> and of imaging contrast<sup>298</sup> and ac impedance responses in SECM.<sup>299</sup>

## 6.2. Nanopore Electrodes

Nanopore electrodes are electrodes recessed into a nanoscopic pore structure. They can be models of single nanopore structures. Fabrication<sup>229,311</sup> involves preparation of a Pt nanoelectrode with a glass shroud. The Pt wire sealed in glass has a conical tip, so that electrochemically etching the Pt back leaves a glass walled pore with a conical shape and orifice roughly equal to the diameter of the original nanoelectrode, ranging from 30<sup>312</sup> to 2000<sup>229</sup> nm. Figure 31 illustrates this geometry for an actual, dimensionally characterized example.<sup>229</sup> The characterization was based on a combination of analytical theory and finite-element simulations with exhaustive measurements of the diffusive flux of a redox molecule through the pore orifice (e.g., that of ferrocene in acetonitrile solvent). As indicated by Figure 32, the diffusive redox flux to the nanopore orifice from the bulk solution follows a radial geometry, whereas that inside the conical pore just above the electrode will approach a linear geometry if the pore is deep enough. If the nanopore electrode is placed in a ferrocene solution, voltammetry on long time scales gives steady state (radial diffusion) limiting currents (for ferrocene oxidation) that are transport controlled through the nanopore orifice. These steady state currents decrease for increasing pore depth, up to a pore depth 50-

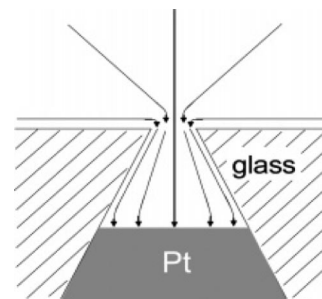


**Figure 32.** Schematic of the flux of a redox species into a nanopore. Reprinted with permission from ref 229. Copyright 2006 American Chemical Society.

fold larger than the pore orifice, whereupon they become constant and depend only on the nanopore orifice diameter and cone angle. At sufficiently short voltammetric times, currents become controlled by linear diffusion to the electrode (within the pore cone), giving classically shaped cyclic voltammograms (CV) that follow eq 5. On intermediate time scales, the CV response can be that of a thin layer cell, in which all of the initially resident ferrocene in the pore cone is exhausted before any significant contribution from ferrocene influx at the pore orifice.

Voltammetry at nanopore electrodes was examined<sup>313</sup> at low electrolyte concentrations to ascertain whether electroneutrality could be maintained within the conical pore interior by the ion current at the pore orifice on the time scale of voltammetric measurements. Finite-element simulations showed that the maximum concentration gradients of a ferrocene electrode reactant, normally next to the electrode surface, become displaced to the nanopore orifice when transport is pore-controlled. Well-defined voltammetry could be observed, even without deliberately added electrolyte, and for both ferrocene (neutral) and a positively charged ferrocene derivative, the currents could be quantitatively accounted for by known diffusion/migration theory. It was concluded that electroneutrality is maintained within the nanopore cone (except of course within the double layer itself). Shifts in the ferrocene apparent formal potential for nanopore orifices >100 nm diameter were ascribed to a Donnan potential difference between the pore interior and the bulk solution.

Potent nanopore surface effects can be invoked<sup>312</sup> for nanopore orifices >100 nm diameter when the interior glass walls of the nanopore cone are derivatized with an amino-organosilane so that they are positively charged at pH >4. (The exterior of the glass structure is treated with a surface-neutral organosilane). The nanopore orifice becomes permselective toward the charge on a redox reactant, admitting negatively charged redox reactants but not positively charged ones. The permselective effect goes away at higher pH (>6) or when the nanopore orifice is significantly larger than the Debye screening length. This provides an example of pH gating of nanopore transport.

An analogous, photon-gating behavior<sup>314</sup> was devised for the nanopore electrode by derivatizing the interior pore walls with a (neutral) spiropyran that could be photolytically converted to a protonated merocyanine form by UV irradiation. Voltammetry of cationic redox species was nearly entirely suppressed following the photolytic conversion, which could be reversed by visible light irradiation. Both of these gating experiments were conducted at low electrolyte content; addition<sup>314</sup> of electrolyte in the second example



would also reverse the effects of UV irradiation by screening the positive surface charges.

The White laboratory has shown that the glass nanopore electrode structure can be employed in a variety of experiments. It was used<sup>315</sup> to fashion a nanoscopic ion selective electrode—which was employed in a SECM experiment to image chloride ion flux through a micropore and to support<sup>316</sup> exceptionally stable lipid membrane structures containing the  $\alpha$ -hemolysin ion-channel-former. The latter have been employed in ac/dc studies of a nine bp DNA hairpin molecule transit through the ion channel.<sup>317</sup>

## 7. Acknowledgments

The support of the Office of Naval Research and the National Science Foundation is gratefully acknowledged. The fine efforts of my colleagues and of professional friends who worked on projects mentioned in the review are warmly acknowledged, as is the able assistance of Deborah Norton in preparing the review.

## 8. References

- (1) Hayat, M. A., Ed. *Colloidal Gold: Principles, Methods and Applications*; Academic Press: 1991.
- (2) Schmid, G. *Chem. Rev.* **1992**, 92, 1409.
- (3) G. Schmid, G., Ed. *Clusters and Colloids*; VCH: Weinheim, Germany, 1994.
- (4) Faraday, M. *Philos. Trans.* **1857**, 147, 145.
- (5) Mie, G. *Ann. Phys.* **1908**, 25, 377.
- (6) Henglein, A. *J. Phys. Chem.* **1979**, 83, 2209.
- (7) Kiwi, J.; Gratzel, M. *J. Am. Chem. Soc.* **1979**, 101, 7214.
- (8) Henglein, A. *Chem. Rev.* **1989**, 89, 1861.
- (9) Henglein, A. *Top. Curr. Chem.* **1988**, 143, 113.
- (10) Henglein, A.; Lillie, J. *J. Am. Chem. Soc.* **1981**, 103, 1059.
- (11) Henglein, A. *Ber. Bunsen-Ges.* **1995**, 7, 903.
- (12) Henglein, A. *Ber. Bunsen-Ges.* **1997**, 101, 1562.
- (13) Henglein, A. *Langmuir* **2001**, 17, 2329.
- (14) Henglein, F.; Henglein, A.; Mulvaney, P. *Ber. Bunsen-Ges.* **1994**, 2, 180.
- (15) Mulvaney, P.; Giersig, M.; Henglein, A. *J. Phys. Chem.* **1993**, 97, 7061.
- (16) Henglein, A.; Mulvaney, P.; Holzwarth, A.; Sosebee, T.; Fojtik, A.; Bereich, S. *Ber. Bunsen-Ges.* **1992**, 6, 754.
- (17) Henglein, A. *J. Phys. Chem.* **2000**, 104, 6683.
- (18) Henglein, A.; Giersig, M. *J. Phys. Chem.* **2000**, 104, 5056.
- (19) Henglein, A. *J. Phys. Chem. B* **2000**, 104, 1206.
- (20) Henglein, A. *J. Phys. Chem. B* **1999**, 103, 9302.
- (21) Janata, E.; Henglein, A.; Ershov, B. *J. Phys. Chem.* **1996**, 100, 1989.
- (22) Henglein, A.; Giersig, M. *J. Phys. Chem.* **1994**, 98, 6931.
- (23) Henglein, A.; Gutierrez, M.; Janata, E.; Ershov, B. *G. J. Phys. Chem.* **1992**, 96, 4598.
- (24) Miller, D.; McLendon, G. *Inorg. Chem.* **1981**, 20, 950.
- (25) Miller, D. S.; Bard, A. J.; McLendon, G.; Ferguson, J. *J. Am. Chem. Soc.* **1981**, 103, 5336.
- (26) Schmid, G.; Giebel, U.; Hunter, W.; Schwenk, A. *Inorg. Chim. Acta* **1984**, 85, 97.
- (27) Larpent, C.; Patin, H. *J. Mol.* **1988**, 44, 191.
- (28) Vargaftik, M. N.; Zagorodnikov, V. P.; Stolyarov, I. P.; Moiseev, I. I.; Likhobolov, V. I.; Kochuvev, D. I.; Chuvin, A. L.; Zaikovsky, V. I.; Zamaraev, K. I.; Timofeeva, G. I. *J. Chem. Soc., Chem. Commun.* **1986**, 937.
- (29) Schmid, G.; Morun, B.; Malm, J.-O. *Agnew. Chem., Int. Ed. Engl.* **1989**, 28, 778.
- (30) Brust, M.; Walker, M.; Bethell, D.; Schiffrin, D. J.; Whyman, R. *J. Chem. Soc., Chem. Commun.* **1994**, 7, 801.
- (31) Scott, R. W. J.; Wilson, O. M.; Crooks, R. M. *J. Phys. Chem. B* **2005**, 109, 692.
- (32) Mirkin, C. A.; Letsinger, R. L.; Mucic, R. C.; Storhoff, J. J. *Nature* **1996**, 382, 607.
- (33) Rosi, N. L.; Mirkin, C. A. *Chem. Rev.* **2005**, 105, 1547.
- (34) Ostwald, W. *Die Welt der vernachlässigten Dimensionen* 4 Aufl., Tit. Steinkopff, Dresden, 1920.
- (35) Jortner, J.; Ratner, M. A., Eds.; *Molecular Electronics*; IUPAC Series Chemistry for the 21st Century; Blackwell Science: Oxford, U.K., 1997.
- (36) (a) Schichibu, Y.; Negishi, Y.; Watanabe, T.; Chaki, N. K.; Kawaguchi, H.; Tsukuda, T. *J. Phys. Chem. C* **2007**, 111, 7845. (b) Jazdzinsky, P. D.; Calero, G.; Ackerson, C. J.; Bushnell, D. A.; Kornberg, R. D. *Science* **2007**, 318, 430. (c) Heaven, M. W.; Dass, A.; White, P. S.; Holt, K. M.; Murray, R. W. *J. Am. Chem. Soc.* **2008**, 130, 3754.
- (37) Bard, A. J.; Faulkner, L. R. *Electrochemical Methods, Fundamentals and Applications*, 2nd ed.; Wiley: New York, 2001.
- (38) Ung, T.; Giersig, M.; Dunstan, D.; Mulvaney, P. *Langmuir* **1997**, 13, 1773.
- (39) Hostetler, M. J.; Wingate, J.; Zhong, C.-J.; Harris, J. E.; Vachet, R. W.; Clark, M. R.; Londono, J. D.; Green, S. J.; Stokes, J. J.; Wignall, G. D.; Glish, G. L.; Porter, M. D.; Evans, N. D.; Murray, R. W. *Langmuir* **1998**, 14, 17.
- (40) Green, S. J.; Stokes, J. J.; Hostetler, M. J.; Pietron, J.; Murray, R. W. *J. Phys. Chem. B* **1997**, 101, 2663.
- (41) Miles, D. T.; Murray, R. W. *Anal. Chem.* **2001**, 73, 921.
- (42) (a) Hostetler, M. J.; Green, S. J.; Stokes, J. J.; Murray, R. W. *J. Am. Chem. Soc.* **1996**, 118, 4212. (b) Templeton, A. C.; Hostetler, M. J.; Kraft, C. T.; Murray, R. W. *J. Am. Chem. Soc.* **1998**, 120, 1906. (c) Agasti, S. S.; You, C.-C.; Arumugam, P.; Rotello, V. M. *J. Mater. Chem.* **2008**, 18, 70.
- (43) Chen, S.; Huang, K. *J. Cluster Sci.* **2000**, 11, 405.
- (44) (a) Ingram, R. S.; Hostetler, M. J.; Murray, R. W.; Schaaf, T. G.; Khoury, J.; Whetten, R. L.; Bigioni, T. P.; Guthrie, D. K.; First, P. N. *J. Am. Chem. Soc.* **1997**, 119, 9279. (b) Templeton, A. C.; Wuelfing, W. P.; Murray, R. W. *Acc. Chem. Res.* **2000**, 33, 27. (c) Devarajan, S.; Sampath, S. *Chem. Nanomater.* **2004**, 2, 646.
- (45) Chen, S.; Murray, R. W.; Feldberg, S. W. *J. Phys. Chem. B* **1998**, 102, 9898.
- (46) Cliffl, D. E.; Hicks, J. F.; Templeton, A. C.; Murray, R. W. In *Metal Nanoparticles: Synthesis, Characterizations, and Applications*; Feldheim, D., Foss, C., Eds.; Marcel Dekker, Inc.: New York, 2002; pp 297.
- (47) Pietron, J. J.; Hicks, J. F.; Murray, R. W. *J. Am. Chem. Soc.* **1999**, 121, 5565.
- (48) Chen, S.; Murray, R. W. *J. Phys. Chem. B* **1999**, 103, 9996.
- (49) Su, B.; Girault, H. H. *J. Phys. Chem. B* **2005**, 109, 111427.
- (50) Miles, D. T.; Leopold, M. C.; Hicks, J. F.; Murray, R. W. *J. Electroanal. Chem.* **2003**, 554, 87.
- (51) Schaaff, T. G.; Shafigullin, M. N.; Khoury, J. T.; Vezmar, I.; Whetten, R. L. *J. Phys. Chem. B* **2007**, 105, 8785.
- (52) Wyrwas, R. B.; Alvarez, M. M.; Khoury, J. T.; Price, R. C.; Schaaff, T. G.; Whetten, R. L. *Eur. Phys. J. D: At., Mol. Opt. Plasma Phys.* **2007**, 43, 91.
- (53) Luedtke, W. D.; Landman, U. *J. Phys. Chem. B* **1998**, 102, 6566.
- (54) Hicks, J. F.; Templeton, A. C.; Chen, S.; Sheran, K. M.; Jasti, R.; Murray, R. W.; Debor, J.; Schaaff, T. G.; Whetten, R. L. *Anal. Chem.* **1999**, 71, 3703.
- (55) Porter, M. D.; Bright, T. B.; Allara, D. L.; Chidsey, C. E. D. *J. Am. Chem. Soc.* **1987**, 109, 3559.
- (56) Lica, G. C.; Zelakiewicz, B. S.; Tong, Y. Y. *J. Elec. Chem.* **2003**, 127, 554–555.
- (57) Hicks, J. F.; Miles, D. T.; Murray, R. W. *J. Electroanal. Chem.* **2003**, 554, 127.
- (58) Quinn, B. M.; Liljeroth, P.; Ruiz, V.; Laaksonen, T.; Kontturi, K. *J. Am. Chem. Soc.* **2003**, 125, 6644.
- (59) Holm, A. H.; Ceccato, M.; Donkers, R. L.; Fabris, L.; Pace, G.; Maran, F. *Langmuir* **2006**, 22, 10584.
- (60) Guo, R.; Georganopoulou, D.; Feldberg, S. W.; Donkers, R.; Murray, R. W. *Anal. Chem.* **2005**, 77, 2662.
- (61) Chen, S. *J. Am. Chem. Soc.* **2000**, 122, 7420.
- (62) Yang, G.; Tan, L.; Yang, Y.; Chen, S.; Lui, G.-Y. *Surf. Sci.* **2005**, 589, 129.
- (63) Su, B.; Zhang, M.; Shao, Y.; Girault, H. H. *J. Phys. Chem. B* **2006**, 110, 21460.
- (64) Laaksonen, T.; Pelliniemi, O.; Quinn, B. M. *J. Am. Chem. Soc.* **2006**, 128, 14341.
- (65) Quinn, B. M.; Kontturi, K. *J. Am. Chem. Soc.* **2004**, 126, 7168.
- (66) Wuelfing, W. P.; Templeton, A. C.; Hicks, J. F.; Murray, R. W. *Anal. Chem.* **1999**, 71, 4069.
- (67) Garcia-Morales, V.; Mafe, S. *J. Phys. Chem.* **2007**, 111, 7242.
- (68) Chen, S.; Pei, R. *J. Am. Chem. Soc.* **2001**, 123, 10607.
- (69) (a) Chen, S.; Pei, R.; Zhao, T.; Dyer, D. *J. Phys. Chem. B* **2002**, 106, 1903. (b) Nishimori, Y.; Kanaizuka, K.; Murata, M.; Nishihara, H. *Chem. Asian J.* **2007**, 2, 367.
- (70) Chen, S. *J. Electroanal. Chem.* **2004**, 574, 153.
- (71) (a) Deng, F.; Chen, S. *Langmuir* **2007**, 23, 936. (b) Deng, F.; Chen, S. *Phys. Chem.* **2005**, 7, 3375.
- (72) Laaksonen, T.; Ruiz, V.; Murtomaki, L.; Quinn, B. M. *J. Am. Chem. Soc.* **2007**, 129, 7732.
- (73) Albrecht, T.; Mertens, S. F. L.; Ulstrup, J. *J. Am. Chem. Soc.* **2007**, 129, 9162.

- (74) Katz, E.; Lioubashevski, O.; Willner, I. *Chem. Commun.* **2006**, 1109.
- (75) (a) Wolfe, R. L.; Murray, R. W. *Anal. Chem.* **2006**, 78, 1167. (b) Stiles, R. L.; Balasubramanian, B.; Feldberg, S. W.; Murray, R. W. *J. Am. Chem. Soc.*, in press.
- (76) Kim, Y.-G.; Garcia-Martinez, J. C.; Crooks, R. M. *Langmuir* **2005**, 21, 5485.
- (77) Wolfe, R. L.; Balasubramanian, R.; Tracy, J. B.; Murray, R. W. *Langmuir* **2007**, 23, 2247.
- (78) (a) Chaki, N. K.; Kakade, B.; Sharma, J.; Mahima, S.; Vijayamohan, K. P. *J. Appl. Phys.* **2004**, 96, 5032. (b) Chaki, N. K.; Singh, P.; Dharmadhikari, C. V.; Vijayamohan, K. P. *Langmuir* **2004**, 20, 10208. (c) Kakade, B. A.; Bhaskar, S. S. S.; Sathe, R.; Halligudi, S. B.; Pillai, V. K. *Adv. Mater.* **2007**, 19, 272.
- (79) Chen, S.; Sommers, J. M. *J. Phys. Chem. B* **2001**, 105, 8816.
- (80) (a) Branham, M. R.; Douglas, A. D.; Mills, A. J.; Tracy, J. B.; White, P. S.; Murray, R. W. *Langmuir* **2006**, 22, 11376. (b) Cheng, W.; Dong, S.; Wang, E. *Electrochem. Commun.* **2002**, 4, 412. (c) Zamborini, F. P.; Gross, S. M.; Murray, R. W. *Langmuir* **2001**, 17, 481.
- (81) (a) Chen, S.; Yang, Y. *J. Am. Chem. Soc.* **2002**, 124, 5280. (b) Yang, Y.; Grant, K. M.; White, H. S.; Chen, S. *Langmuir* **2003**, 19, 9446.
- (82) (a) Franceschetti, A.; Zunger, A. *Phys. Rev. B* **2000**, 62, 2614. (b) Weaver, M. J.; Gao, X. *J. Phys. Chem.* **1993**, 97, 332.
- (83) Chen, S.; Ingram, R. S.; Hostetler, M. J.; Pietron, J. J.; Murray, R. W.; Schaaff, T. G.; Khoury, J. T.; Alvarez, M. M.; Whetten, R. L. *Science* **1998**, 280, 2098.
- (84) Balasubramanian, R.; Guo, R.; Mills, A. J.; Murray, R. W. *J. Am. Chem. Soc.* **2005**, 127, 8126.
- (85) Chaki, N. K.; Tsunoyama, H.; Negishi, Y.; Tsukuda, T. *Symposium on Nanoparticles, Electrons, and Photons*; 210th Annual Meeting of the Electrochemical Society, Cancun, Mexico, November 2006.
- (86) Lee, D.; Donkers, R. L.; Wang, G.-L.; Harper, A. S.; Murray, R. W. *J. Am. Chem. Soc.* **2004**, 126, 6193.
- (87) Jimenez, V. L.; Georganopoulou, D. G.; White, R. J.; Harper, A. S.; Mills, A. J.; Lee, D.; Murray, R. W. *Langmuir* **2004**, 20, 6864.
- (88) Tracy, J. B.; Kalyuzhny, G.; Crowe, M. C.; Balasubramanian, R.; Choi, J. P.; Murray, R. W. *J. Am. Chem. Soc.* **2007**, 129, 6706.
- (89) Menard, L. D.; Gao, S.; Xu, H.; Twisten, R. D.; Harper, A. S.; Song, Y.; Wang, G.; Douglas, A. D.; Yang, J. C.; Frenkel, A. I.; Nuzzo, R. G.; Murray, R. W. *J. Phys. Chem. B* **2006**, 110, 12874.
- (90) Shichibu, Y.; Negishi, Y.; Tsunoyama, H.; Kanehara, M.; Teranishi, T.; Tsukuda, T. *Small* **2007**, 5, 835.
- (91) (a) Tracy, J. B.; Kalyuzhny, G.; Crowe, M. C.; Balasubramanian, R.; Choi, J. P.; Murray, R. W. *J. Am. Chem. Soc.* **2007**, 129, 6706. (b) Negishi, Y.; Chaki, N. K.; Schichibu, Y.; Whetten, R. L.; Tsukuda, T. *J. Am. Chem. Soc.* **2007**, 129, 11322. (c) Tracy, J. B.; Crowe, M. C.; Parker, J. P.; Hampe, O.; Fields-Zinna, C. A.; Dass, A.; Murray, R. W. *J. Am. Chem. Soc.* **2007**, 129, 16209.
- (92) Georganopoulou, D. G.; Mirkin, M. V.; Murray, R. W. *Nano Lett.* **2004**, 4, 1763.
- (93) Wang, W.; Murray, R. W. *Langmuir* **2005**, 21, 7015.
- (94) Guo, R.; Murray, R. W. *J. Am. Chem. Soc.* **2005**, 127, 12140.
- (95) Wang, W.; Murray, R. W. *J. Phys. Chem. B* **2006**, 110, 10258.
- (96) Choi, J.-P.; Murray, R. W. *J. Am. Chem. Soc.* **2006**, 128, 10496.
- (97) Antonello, S.; Holm, A. H.; Instuli, E.; Maran, F. *J. Am. Chem. Soc.* **2007**, 129, 9836.
- (98) Dass, A.; Stevenson, A.; Dubay, G. R.; Tracy, J. B.; Murray, R. W. *J. Am. Chem. Soc.* **2008**, 130, 5940.
- (99) Negishi, Y.; Nobusada, K.; Tsukuda, T. *J. Am. Chem. Soc.* **2005**, 127, 5261.
- (100) Iwasa, T.; Nobusada, K. *Chem. Phys. Lett.* **2007**, 441, 268.
- (101) Oh, S.-K.; Kim, Y.-G.; Ye, H.; Crooks, R. M. *Langmuir* **2003**, 19, 10420.
- (102) Wilson, O. M.; Scott, R. W. J.; Garcia-Martinez, J. C.; Crooks, R. M. *J. Am. Chem. Soc.* **2005**, 127, 1015.
- (103) Knecht, M. R.; Garcia-Martinez, J. C.; Crooks, R. M. *Chem. Mater.* **2006**, 18, 5039.
- (104) (a) Kim, Y.-G.; Garcia-Martinez, J. C.; Crooks, R. M. *Langmuir* **2005**, 21, 5485. (b) Garcia-Martinez, J. C.; Scott, R. W. J.; Crooks, R. M. *J. Am. Chem. Soc.* **2003**, 125, 11190.
- (105) Knecht, M. R.; Weir, M. G.; Frenkel, A. I.; Crooks, R. M. *Chem. Mater.* **2008**, 20, 1019.
- (106) Ye, H.; Crooks, R. M. *J. Am. Chem. Soc.* **2007**, 129, 3627.
- (107) Garcia-Martinez, J. C.; Crooks, R. M. *J. Am. Chem. Soc.* **2004**, 126, 16170.
- (108) Knecht, M. R.; Garcia-Martinez, J. C.; Crooks, R. M. *Langmuir* **2005**, 21, 11981.
- (109) Templeton, A. C.; Chen, S.; Gross, S. M.; Murray, R. W. *Langmuir* **1999**, 15, 66.
- (110) (a) Templeton, A. C.; Cliffler, D. E.; Murray, R. W. *J. Am. Chem. Soc.* **1999**, 121, 7081. (b) Gittins, D. I.; Bethell, D.; Schiffrin, D. J.; Nichols, R. J. *Nature* **2000**, 408, 67.
- (111) Fabris, L.; Antonello, S.; Armelao, L.; Donkers, R. L.; Polo, F.; Toniolo, C.; Maran, F. *J. Am. Chem. Soc.* **2006**, 128, 326.
- (112) Reed, M. A.; Randall, J. N.; Aggarwal, R. J.; Matyi, R. J.; Moore, T. M.; Wetsel, A. E. *Phys. Rev. Lett.* **1988**, 60, 535.
- (113) Quinn, B. M.; Lijeroth, P.; Kontturi, K. *J. Am. Chem. Soc.* **2002**, 124, 12915.
- (114) (a) Peterson, R. R.; Cliffler, D. E. *Langmuir* **2006**, 31, 10307. (b) Kwak, J.; Bard, A. J. *Anal. Chem.* **1989**, 61, 1221.
- (115) Parker, J. F.; Murray, R. W. Unpublished results, University of North Carolina, Chapel Hill, NC, 2007.
- (116) Lee, D.; Donkers, R. L.; DeSimone, J. M.; Murray, R. W. *J. Am. Chem. Soc.* **2003**, 125, 1182.
- (117) (a) Wuelfing, W. P.; Gross, S. M.; Miles, D. T.; Murray, R. W. *J. Am. Chem. Soc.* **1998**, 120, 12696. (b) Ahonen, P.; Ruiz, V.; Kontturi, K.; Liljeroth, P.; Quinn, B. M. *J. Phys. Chem. C* **2008**, 112, 2724.
- (118) Shon, Y.-S.; Wuelfing, W. P.; Murray, R. W. *Langmuir* **2001**, 17, 1255.
- (119) Wuelfing, W. P.; Green, S. J.; Pietron, J. J.; Cliffler, D. E.; Murray, R. W. *J. Am. Chem. Soc.* **2000**, 122, 11465.
- (120) Templeton, A. C.; Pietron, J. J.; Murray, R. W.; Mulvaney, P. J. *J. Phys. Chem.* **2000**, 104, 564.
- (121) Song, Y.; Murray, R. W. *J. Am. Chem. Soc.* **2002**, 124, 7096.
- (122) Song, Y.; Harper, A.; Murray, R. W. *Langmuir* **2005**, 21, 5492.
- (123) Marcus, R. A. *Can. J. Chem.* **1959**, 37, 155.
- (124) Nicholson, R. S. *Anal. Chem.* **1965**, 37, 1351.
- (125) Choi, J.-P.; Murray, R. W. University of North Carolina, Chapel Hill, NC, 2006, manuscript in preparation.
- (126) Nielsen, R. M.; McManis, G. E.; Safford, L. K.; Weaver, M. J. *J. Phys. Chem.* **1989**, 93, 2152.
- (127) Nielson, R. M.; McManis, G. E.; Golovin, M. N.; Weaver, M. J. *J. Phys. Chem.* **1988**, 92, 3441.
- (128) Dahms, J. *J. Phys. Chem.* **1968**, 72, 362.
- (129) Ruff, I.; Botar, L. *J. Chem. Phys.* **1985**, 83, 1292.
- (130) Buttry, D. A.; Anson, F. C. *J. Am. Chem. Soc.* **1983**, 105, 685.
- (131) Majda, M. In *Molecular Design of Electrode Surfaces*; Techniques of Chemistry; Murray, R. W., Ed.; John Wiley and Sons, Inc.: New York, 1992.
- (132) Harper, A. S.; Lee, D.; Crooker, J. C.; Wang, W.; Williams, M. E.; Murray, R. W. *J. Phys. Chem. B* **2004**, 108, 1866.
- (133) Chen, S. *Langmuir* **1999**, 15, 7551.
- (134) Green, S. J.; Pietron, J. J.; Stokes, J. J.; Hostetler, M. J.; Vu, H.; Wuelfing, W. P.; Murray, R. W. *J. Phys. Chem. B* **1998**, 101, 2663.
- (135) Chen, S.; Huang, K. *Langmuir* **2000**, 16, 2014.
- (136) Yamada, M.; Nishihara, H. *Langmuir* **2003**, 19, 8050.
- (137) (a) Yamada, M.; Nishihara, H. C. R. *Chimie* **2003**, 6, 919. (b) Yamada, M.; Tadera, T.; Kubo, K.; Nishihara, H. *Langmuir* **2001**, 17, 2363. (c) Yamada, M.; Kubo, K.; Nishihara, H. *Chem. Lett.* **1999**, 1335.
- (138) (a) Yamada, M.; Tadera, T.; Kubo, K.; Nishihara, H. *J. Phys. Chem. B* **2003**, 107, 3703. (b) Horikoshi, T.; Itoh, M.; Kurihara, M.; Kubo, K.; Nishihara, H. *J. Electroanal. Chem.* **1999**, 473, 113. (c) Yamada, M.; Nishihara, H. *Eur. Phys. J. D* **2003**, 24, 257. (d) Yamada, M.; Nishihara, H. *Chem. Commun.* **2002**, 2578.
- (139) Yamada, M.; Quiros, I.; Mizutani, J.; Kubo, K.; Nishihara, H. *Phys. Chem. Chem. Phys.* **2001**, 3, 3377.
- (140) Li, D.; Zhang, Y.; Jiang, J.; Li, J. *J. Colloid Interface Sci.* **2003**, 264, 109.
- (141) Li, D.; Li, J. *Surf. Sci.* **2003**, 522, 105.
- (142) Ingram, R. S.; Murray, R. W. *Langmuir* **1998**, 14, 4115.
- (143) Pietron, J. J.; Murray, R. W. *J. Phys. Chem.* **1999**, 103, 4440.
- (144) Templeton, A. C.; Hostetler, M. J.; Warmoth, E. L.; Chen, S.; Hartshorn, C. M.; Krishnamurthy, M. V.; Forbes, M. D. E.; Murray, R. W. *J. Am. Chem. Soc.* **1998**, 120, 4845.
- (145) (a) Amatore, C.; Bouret, Y.; Maisonhaute, E.; Goldsmith, J. I.; Abruna, H. D. *Chem.—Eur. J.* **2001**, 7, 2206. (b) Amatore, C.; Bouret, Y.; Maisonhaute, E.; Goldsmith, J. I.; Abruna, H. D. *ChemPhysChem* **2001**, 21, 30.
- (146) (a) Boal, A. K.; Rotello, V. M. *J. Am. Chem. Soc.* **1999**, 121, 4914. (b) Shenhar, R.; Rotello, V. M. *Acc. Chem. Res.* **2003**, 36, 549. (c) Niemz, A.; Rotello, V. M. *Acc. Chem. Res.* **1999**, 32, 44.
- (147) Chen, S. *J. Phys. Chem. B* **2000**, 104, 663.
- (148) Men, Y.; Kubo, K.; Kurihara, M.; Nishihara, H. *Phys. Chem. Chem. Phys.* **2001**, 3, 3427.
- (149) Hicks, J. F.; Zamborini, F. P.; Murray, R. W. *J. Phys. Chem.* **2002**, 106, 7751.
- (150) Chen, S. *Adv. Mater.* **2000**, 12, 186.
- (151) Chen, S. *Langmuir* **2001**, 17, 2878.
- (152) Yang, Y.; Pradhan, S.; Chen, S. *J. Am. Chem. Soc.* **2004**, 126, 76.
- (153) Lee, W.-Y.; Hostetler, M. J.; Murray, R. W.; Majda, M. *Isr. J. Chem.* **1997**, 37, 213.
- (154) Chen, S. *Langmuir* **2001**, 17, 6664.
- (155) Chen, S. *Anal. Chim. Acta* **2003**, 496, 29.



- (156) (a) Liljeroth, P.; Quinn, B. M. *J. Am. Chem. Soc.* **2006**, *128*, 4922. (b) Liljeroth, P.; Vanmaekelbergh, D.; Ruiz, V.; Kontturi, K.; Jiang, H.; Kauppinen, E.; Quinn, B. M. *J. Am. Chem. Soc.* **2004**, *126*, 7126.
- (157) Ranganathan, S.; Guo, R.; Murray, R. W. *Langmuir* **2007**, *23*, 7372.
- (158) Uosaki, K.; Kondo, T.; Okamura, M.; Song, W. *Faraday Discuss.* **2002**, *121*, 373.
- (159) Zamborini, F. P.; Hicks, J. C.; Murray, R. W. *J. Am. Chem. Soc.* **2000**, *122*, 4514.
- (160) (a) Brennan, J. L.; Branham, M. R.; Hicks, J. F.; Osisek, A. J.; Donkers, R. L.; Georganopoulou, D. G.; Murray, R. W. *Anal. Chem.* **2004**, *76*, 5611. (b) Fishelson, N.; Shkrob, I.; Lve, O.; Gun, J.; Modestove, A. D. *Langmuir* **2001**, *17*, 403.
- (161) (a) Brust, M.; Bethell, D.; Kiely, C. J.; Schiffrin, D. J. *Langmuir* **1998**, *14*, 5425. (b) Gittins, D. I.; Bethell, D.; Nichols, R. J.; Schiffrin, D. J. *Adv. Mater.* **1999**, *11*, 737.
- (162) Koplin, E.; Niemeyer, C. M.; Simon, U. *J. Mater. Chem.* **2006**, *16*, 1338.
- (163) Decher, G. *Science* **1997**, *277*, 1232.
- (164) (a) Hicks, J. F.; Seok-Shon, Y.; Murray, R. W. *Langmuir* **2002**, *18*, 2288. (b) Xu, H.; Hong, R.; Wang, X.; Arvizo, R.; You, C.; Samanta, B.; Patra, D.; Tuominen, M. T.; Rotello, V. M. *Adv. Mater.* **2007**, *19*, 1383.
- (165) Choi, J.-P.; Coble, M. M.; Branham, M. R.; DeSimone, J. M.; Murray, R. W. *J. Phys. Chem. C* **2007**, *111*, 3778.
- (166) (a) Wuelfing, W. P.; Murray, R. W. *J. Phys. Chem. B* **2002**, *106*, 3139–3145. (b) (Addition/Correction) 2003, *107*, 6018.
- (167) Leopold, M. C.; Donkers, R. L.; Georganopoulou, D.; Fisher, M.; Zamborini, F. P.; Murray, R. W. *Faraday Discuss.* **2003**, *125*, 63.
- (168) Wohltjen, H.; Snow, A. W. *Anal. Chem.* **1998**, *70*, 2856.
- (169) Steinecker, W. H.; Rowe, M. P.; Zellers, E. T. *Anal. Chem.* **2007**, *79*, 4977.
- (170) (a) Cai, Q.-Y.; Zellers, E. T. *Anal. Chem.* **2002**, *74*, 3533. (b) Ibanez, F. J.; Zamborini, F. P. *J. Am. Chem. Soc.* **2008**, *130*, 622. (c) Ibanez, F. J.; Zamborini, F. P. *Langmuir* **2006**, *22*, 9789.
- (171) Pradhan, S.; Sun, J.; Deng, F.; Chen, S. *Adv. Mater.* **2006**, *18*, 3279.
- (172) Zamborini, F. P.; Leopold, M. C.; Hicks, J. F.; Kulesza, P.; Malik, M. A.; Murray, R. W. *J. Am. Chem. Soc.* **2002**, *124*, 8958.
- (173) (a) Evans, S. D.; Johnson, S. R.; Cheng, Y. L.; Shen, T. J. *Mater. Chem.* **2000**, *10*, 183. (b) Joseph, Y.; Peic, A.; Chen, X.; Michl, J.; Vossmeier, T.; Yasuda, A. *J. Phys. Chem. C* **2007**, *111*, 12855.
- (174) Pang, P.; Guo, J.; Wu, S.; Cai, Q. *Sens. Actuators, B: Chem.* **2006**, *B114*, 799.
- (175) Pang, P.; Guo, Z.; Cai, Q. *Talanta* **2005**, *65*, 1343.
- (176) Yvonne, J.; Guse, B.; Yasuda, A.; Vossmeier, T. *Sens. Actuators, B: Chem.* **2004**, *B98*, 188.
- (177) Joseph, Y.; Krasteva, N.; Besnard, I.; Guse, B.; Rosenberger, M.; Wild, U.; Knop-Gericke, A.; Schloegl, R.; Krustev, R.; Yasuda, A.; Vossmeier, T. *Faraday Discuss.* **2003**, *125*, 77.
- (178) Joseph, Y.; Besnard, I.; Rosenberger, M.; Guse, B.; Nothofer, H.-G.; Wessels, J. M.; Wild, U.; Knop-Gericke, A.; Su, D.; Schloegl, R.; Uasida, A. Y.; Vossmeier, T. *J. Phys. Chem. B* **2003**, *107*, 7406.
- (179) Nadejda, K.; Guse, B.; Besnard, I.; Yasuda, A.; Vossmeier, T. *Sens. Actuators, B: Chem.* **2003**, *B92*, 137.
- (180) Nadejda, K.; Besnard, I.; Guse, B.; Bauer, R. E.; Muellen, K.; Yasuda, A.; Vossmeier, T. *Nano Lett.* **2002**, *5*, 551.
- (181) (a) Vossmeier, T.; Guse, B.; Besnard, I.; Bauer, R. E.; Mullen, K.; Yasuda, A. *Adv. Mater.* **2002**, *3*, 238. (b) Krasteva, N.; Fogel, Y.; Bauer, R. E.; Muellen, K.; Joseph, Y.; Matsuzawa, N.; Yasuda, A.; Vossmeier, T. *Adv. Funct. Mater.* **2007**, *17*, 881.
- (182) Chidsey, C. E. D. *Science* **1991**, *251*, 919.
- (183) Smalley, J. F.; Finklea, H. O.; Chidsey, C. E. D.; Linford, M. R.; Creager, S. E.; Ferraris, J. P.; Chalfant, K.; Zawodzinski, T.; Feldberg, S. W.; Newton, M. D. *J. Am. Chem. Soc.* **2003**, *125*, 2004.
- (184) Robinson, D. B.; Chidsey, C. E. D. *J. Phys. Chem. B* **2002**, *106*, 10706.
- (185) Markovich, G.; Collier, C. P.; Henrichs, S. E.; Remacle, F.; Levine, R. D.; Heath, J. R. *Acc. Chem. Res.* **1999**, *32*, 415.
- (186) Sampaio, J. F.; Beverly, K. C.; Heath, J. R. *J. Phys. Chem. B* **2001**, *105*, 8797.
- (187) Markovich, G.; Collier, C. P.; Heath, J. R. *Phys. Rev. Lett.* **1998**, *80*, 3807.
- (188) Quinn, B. M.; Prieto, I.; Haram, S. K.; Bard, A. J. *J. Phys. Chem. B* **2001**, *105*, 7474.
- (189) Charych, D. H.; Anvar, D. J.; Majda, M. *Thin Solid Films* **1994**, *242*, 1.
- (190) Kim, J.; Lee, D. *J. Am. Chem. Soc.* **2006**, *128*, 4518.
- (191) (a) Charych, D. H.; Landau, E. M.; Majda, M. *J. Am. Chem. Soc.* **1991**, *113*, 3340. (b) Forster, R. J.; Keyes, T. E.; Majda, M. *J. Phys. Chem. B* **2000**, *104*, 4425.
- (192) Kondo, T.; Okamura, M.; Uosaki, K. *Chem. Lett.* **2001**, *30*, 930.
- (193) Andrieux, C. P.; Saveant, J. M. In *Molecular Design of Electrode Surfaces*; Murray, R. W., Ed. Wiley: New York, 1992.
- (194) Terrill, R. H.; Postlethwaite, T. A.; Chen, C.; Poon, C.-D.; Terzis, A.; Chen, A.; Hutchison, J. E.; Clark, M. R.; Wignall, G.; Londono, J. D.; Superfine, R.; Falvo, M.; Johnson, C. S., Jr.; Samulski, E. T.; Murray, R. W. *J. Am. Chem. Soc.* **1995**, *117*, 12537.
- (195) (a) Badia, A.; Singh, S.; Demers, L.; Cuccia, L.; Brown, G. R.; Lennox, R. B. *Chem.—Eur. J.* **1996**, *2*, 359. (b) Whetten, R. L.; Khoury, J. T.; Alvarez, M. M.; Murthy, S.; Vezmar, I.; Wang, Z. L.; Stephens, P. W.; Cleveland, C. L.; Luedtke, W. D.; Landman, U. *Adv. Mater.* **1996**, *8*, 428. (c) Ohara, P. C.; Leff, D. V.; Heath, J. R.; Gelbert, W. M. *Phys. Rev. Lett.* **1995**, *75*, 3466–3469.
- (196) Majda, M. In *Molecular Design of Electrode Surfaces*; Murray, R. W., Ed. Wiley: New York, 1992.
- (197) Durtis, L. A.; Naleway, C. A.; Miller, J. R. *J. Phys. Chem.* **1993**, *97*, 4050.
- (198) Willner, I.; Willner, B. *Pure Appl. Chem.* **2002**, *74*, 1773.
- (199) (a) Polsky, R.; Gill, R.; Kaganovsky, L.; Willner, I. *Anal. Chem.* **2006**, *78*, 2268. (b) Wang, J.; Xu, D.; Kawde, A.-N.; Polsky, R. *Anal. Chem.* **2001**, *73*, 5576. (c) Wang, J.; Liu, G.; Merkoci, A. *J. Am. Chem. Soc.* **2003**, *125*, 3214. (d) Park, S.-J.; Taton, T. A.; Mirkin, C. A. *Science* **2002**, *295*, 1503.
- (200) Dayton, M. A.; Brown, J. C.; Stutts, K. J.; Wightman, R. M. *Anal. Chem.* **1980**, *52*, 946.
- (201) Wightman, R. M. *Science* **2006**, *311*, 1570.
- (202) Zoski, C. G. *Electroanalysis* **2002**, *14*, 1041.
- (203) Eklund, J. C.; Bond, A. M.; Alden, J. A.; Compton, R. G. *Adv. Phys. Org. Chem.* **1999**, *32*, 1.
- (204) Amatore, C.; Maisonneuve, E. *Anal. Chem.* **2005**, *77*, 303A.
- (205) Bates, N.; Thouin, L.; Amatore, C.; Heinze, J. *Angew. Chem., Int. Ed. Engl.* **2004**, *43*, 1431.
- (206) Longmire, M. L.; Watanabe, M.; Zhang, H.; Wooster, T. T.; Murray, R. W. *Anal. Chem.* **1990**, *62*, 747.
- (207) Kulesza, P. J.; Cox, J. A. *Electroanalysis* **1998**, *10*, 73.
- (208) (a) Chen, G.; Ewing, A. G. *Crit. Rev. Neurobiol.* **1997**, *11*, 59. (b) Amemiya, S.; Guo, J.; Xiong, H.; Gross, D. A. *Anal. Bioanal. Chem.* **2006**, *386*, 458. (c) Sun, P.; Laforge, F. O.; Abeyweera, T. P.; Rotenberg, S. A.; Carpino, J.; Mirkin, M. V. *Proc. Natl. Acad. Sci. U.S.A.* **2008**, *105*, 443.
- (209) Bard, A. J.; Mirkin, M. V., Eds. *Scanning Electrochemical Microscopy*; Marcel Dekker: New York, 2001.
- (210) Lui, B.; Bard, A. J.; Mirkin, M. V.; Creager, S. E. *J. Am. Chem. Soc.* **2004**, *126*, 1485.
- (211) (a) Sun, P.; Laforge, F. O.; Mirkin, M. V. *Phys. Chem. Chem. Phys.* **2007**, *9*, 802. (b) Xiong, H.; Guo, J.; Amemiya, S. *Anal. Chem.* **2007**, *79*, 2735. (c) Xiong, H.; Gross, D. A.; Guo, J.; Amemiya, S. *Anal. Chem.* **2006**, *78*, 1946.
- (212) Macpherson, J. V.; Simjee, N.; Unwin, P. R. *Electrochim. Acta* **2001**, *47*, 29.
- (213) Wightman, R. M.; Wipf, D. O. *Electroanal. Chem.* **1989**, *15*, 267.
- (214) Wehmeyer, K. R.; Deakin, M. R.; Wightman, R. M. *Anal. Chem.* **1985**, *57*, 1913.
- (215) Arrigan, D. W. M. *Analyst* **2004**, *129*, 1157.
- (216) Penner, R. M.; Heben, M. J.; Longin, T. L.; Lewis, N. S. *Science* **1990**, *250*, 1118.
- (217) Zhang, B.; Galusha, J.; Shiozawa, P. G.; Wang, G.; Berggren, A. J.; Jones, R. M.; White, R. J.; Ervin, E. N.; Cauley, C. C.; White, H. S. *Anal. Chem.* **2007**, *79*, 4778.
- (218) (a) Shao, Y.; Mirkin, M. V. *Anal. Chem.* **1997**, *69*, 1627. (b) Sun, P.; Zhang, Z.; Guo, J.; Shao, Y. *Anal. Chem.* **2001**, *73*, 5346.
- (219) Liu, B.; Rolland, J. P.; DeSimone, J. M.; Bard, A. J. *Anal. Chem.* **2005**, *77*, 3013.
- (220) Chen, S.; Kucernak, A. *Electrochem. Commun.* **2002**, *4*, 80.
- (221) Watkins, J. J.; Chen, J.; White, H. S.; Abruna, H. D.; Maisonneuve, E.; Amatore, C. *Anal. Chem.* **2003**, *75*, 3962.
- (222) Watkins, J. J.; White, H. S. *J. Electroanal. Chem.* **2005**, *582*, 57.
- (223) Watkins, J. J.; White, H. S. *Langmuir* **2004**, *20*, 5474.
- (224) Campbell, J. K.; Sun, L.; Crooks, R. M. *J. Am. Chem. Soc.* **1999**, *121*, 3779.
- (225) (a) Baker, W. S.; Crooks, R. M. *J. Phys. Chem. B* **1998**, *102*, 10041. (b) Quinn, B. M.; Lemay, S. G. *Adv. Mater.* **2006**, *18*, 855.
- (226) (a) Li, J.; Koehne, J. E.; Cassell, A. M.; Chen, H.; Ng, H. T.; Fan, W.; Han, J.; Meyyappan, M. *Electroanalysis* **2005**, *17*, 15. (b) Bertonecello, P.; Edgeworth, J. P.; Macpherson, J. V.; Unwin, P. R. *J. Am. Chem. Soc.* **2007**, *129*, 10982.
- (227) Oldham, K. B. *Anal. Chem.* **1992**, *64*, 646.
- (228) Bard, A. J.; Fan, F.-R.R. *Acc. Chem. Res.* **1996**, *29*, 572.
- (229) (a) Zhang, B.; Zhang, Y.; White, H. S. *Anal. Chem.* **2006**, *78*, 477. (b) Lanyon, Y. H.; De Marzi, G.; Watson, Y. E.; Quinn, A. J.; Gleeson, J. P.; Redmond, G.; Arrigan, D. W. M. *Anal. Chem.* **2007**, *79*, 3048.
- (230) Mirkin, M. V.; Fan, F.-R. F.; Bard, A. J. *Science* **1992**, *257*, 364.
- (231) Mirkin, M. V.; Fan, F.-R. F.; Bard, A. J. *J. Electroanal. Chem.* **1992**, *328*, 47.
- (232) Zoski, C. G.; Mirkin, M. V. *Anal. Chem.* **2002**, *74*, 1986.



- (233) Sun, P.; Mirkin, M. V. *Anal. Chem.* **2007**, 79, 5809.
- (234) Sun, P.; Mirkin, M. V. *Anal. Chem.* **2006**, 78, 6526.
- (235) Morris, R. B.; Franta, D. J.; White, H. S. *J. Phys. Chem.* **1987**, 91, 3559.
- (236) Seibold, J. D.; Scott, E. R.; White, H. S. *J. Electroanal. Chem. Interfacial Electrochem.* **1989**, 264, 281.
- (237) McDevitt, J. T.; Ching, S.; Sullivan, M.; Murray, R. W. *J. Am. Chem. Soc.* **1989**, 111, 4528.
- (238) Kovach, P. A.; Caudill, W. L.; Peters, D. G.; Wightman, R. M. *J. Electroanal. Chem.* **1985**, 185, 285.
- (239) Krapf, D.; Quinn, B. M.; Wu, M.-Y.; Zandbergen, H. W.; Dekker, C.; Lemay, S. G. *NanoLett.* **2006**, 6, 2531.
- (240) Heller, I.; Kong, J.; Williams, K. A.; Dekker, C.; Lemay, S. G. *J. Am. Chem. Soc.* **2006**, 128, 7353.
- (241) Quinn, B. M.; Dekker, C.; Lemay, S. G. *J. Am. Chem. Soc.* **2005**, 127, 6146.
- (242) (a) Norton, J. D.; White, H. S.; Feldberg, S. W. *J. Phys. Chem.* **1990**, 94, 6772. (b) Smith, C. P.; White, H. S. *Anal. Chem.* **1993**, 65, 3343.
- (243) Shao, Y.; Mirkin, M. V. *Anal. Chem.* **1997**, 69, 1627.
- (244) (a) White, R.; White, H. S. *Anal. Chem.* **2005**, 77, 214A. (b) White, R. J.; White, H. S. *Langmuir* **2008**, 24, 2850.
- (245) Lee, C.; Anson, F. C. *J. Electroanal. Chem.* **1992**, 323, 381.
- (246) Beriet, C.; Fletcher, D. *J. Electroanal. Chem.* **1993**, 361, 93.
- (247) Rooney, M. B.; Coomber, D. C.; Bond, A. M. *Anal. Chem.* **2000**, 72, 3486.
- (248) Chen, S.; Kucernak, A. *J. Phys. Chem. B* **2002**, 106, 9396.
- (249) Moerner, W. E. *J. Phys. Chem. B* **2002**, 106, 910.
- (250) Fan, F.-R.F.; Kwak, J.; Bard, A. J. *J. Am. Chem. Soc.* **1996**, 118, 9669.
- (251) Fan, F.-R.F.; Bard, A. J. *Science* **1995**, 267, 871.
- (252) Mirkin, M. V.; Sun, P. S. ECM of individual molecules in zeptoliter volumes, 4th Workshop on Scanning Electrochemical Microscopy, Falcade, Italy, 2006; p 028.
- (253) Hercules, D. M. *Acc. Chem. Res.* **1969**, 2, 301.
- (254) Collinson, M. M.; Wightman, R. W. *Science* **1995**, 268, 1883.
- (255) Zu, Y.; Ding, Z.; Zhou, J.; Lee, Y.; Bard, A. J. *Anal. Chem.* **2001**, 73, 2153.
- (256) Maus, R. G.; Wightman, R. M. *Anal. Chem.* **2001**, 73, 3993.
- (257) Wu, W.-Z.; Huang, W. H.; Wang, W.; Wang, Z.-L.; Cheng, K. J.; Xu, T.; Zhang, R. Y.; Chen, Y.; Liu, J. *J. Am. Chem. Soc.* **2005**, 127, 8914.
- (258) Sun, P.; Laforge, F. O.; Abeyweera, T. P.; Rotenberg, S. A.; Carpino, J.; Mirkin, M. V. *Proc. Natl. Acad. Sci. U.S.A.*, in press.
- (259) Katemann, B. B.; Schulte, A.; Schuhmann, W. *Electroanalysis* **2004**, 16, 60.
- (260) (a) Slevin, C. J.; Gray, N. J.; Macpherson, J. V.; Webb, M. A.; Unwin, P. R. *Electrochem. Commun.* **1999**, 1, 282. (b) Burt, D. P.; Wilson, N. R.; Weaver, J. M. R.; Dobson, P. S.; Macpherson, J. V. *Nano Lett.* **2005**, 5, 639.
- (261) Nyffenegger, R. M.; Penner, R. M. *J. Phys. Chem.* **1996**, 100, 17041.
- (262) Li, W.; Virtanen, J. A.; Penner, R. M. *J. Phys. Chem.* **1992**, 96, 6529.
- (263) Schoer, J. K.; Zamborini, F. P.; Crooks, R. M. *J. Phys. Chem.* **1996**, 100, 11086.
- (264) Zamborini, F. P.; Crooks, R. M. *J. Am. Chem. Soc.* **1998**, 120, 9700.
- (265) Meier, J.; Friedrich, K. A.; Stimming, U. *Faraday Discuss.* **2002**, 121, 365.
- (266) Meier, J.; Schiot, J.; Liu, P.; Nørskov, J. K.; Stimming, U. *Chem. Phys. Lett.* **2004**, 390, 440.
- (267) Eikerling, M.; Meier, J.; Stimming, U. *Phys. Chem.* **2003**, 217, 395.
- (268) Chen, S.; Kucernak, A. *J. Phys. Chem. B* **2004**, 108, 13984.
- (269) Chen, S.; Kucernak, A. *J. Phys. Chem. B* **2003**, 107, 8392.
- (270) Kolb, D. M.; Ullmann, R.; Will, T. *Science* **1997**, 275, 1097.
- (271) Ran, T.-V.; Bard, A. J. *J. Phys. Chem. B* **2006**, 110, 25279.
- (272) Troxler, H.; Wetzel, E.; Kuster, T.; Heizmann, C. W. *Rev. Sci. Instrum.* **1999**, 70, 2257.
- (273) Martin, C. R. *Science* **1994**, 266, 1961.
- (274) Kohli, P.; Wirtz, M.; Martin, C. R. *Electroanalysis* **2004**, 16, 20030.
- (275) Martin, C. R.; Mitchell, D. T. *Anal. Chem.* **1998**, 70, 322A.
- (276) Bayley, H.; Martin, C. R. *Chem. Rev.* **2000**, 100, 2575.
- (277) Mueller, P.; Rudin, D. O.; Tien, H. T.; Westcott, W. C. *Nature* **1962**, 194, 979–980.
- (278) (a) Neher, E.; Sakmann, B. *Nature* **1976**, 260, 799. (b) Hille, B. *Ionic Channels of Excitable Membranes*, 2nd ed.; Sinauer: Sunderland, MA, 1992.
- (279) Ito, T.; Sun, L.; Henriquez, R. R.; Crooks, R. M. *Acc. Chem. Res.* **2004**, 37, 937.
- (280) Sun, L.; Crooks, R. M. *J. Am. Chem. Soc.* **2000**, 122, 12340.
- (281) Ito, T.; Sun, L.; Crooks, R. M. *Anal. Chem.* **2003**, 75, 2399.
- (282) Henriquez, R. R.; Ito, T.; Sun, L.; Crooks, R. M. *Analyst* **2004**, 129, 478.
- (283) Ito, T.; Sun, L.; Bevan, M. A.; Crooks, R. M. *Langmuir* **2004**, 20, 6940.
- (284) Mitsui, T.; Stein, D.; Kim, Y.-R.; Hoogerheide, D.; Golovchenko, J. A. *Phys. Rev. Lett.* **2006**, 96, 036102.
- (285) Li, J.; Stein, D.; McMullan, C.; Branton, D.; Aziz, M. J.; Golovchenko, J. A. *Nature* **2001**, 412, 166.
- (286) (a) Li, J.; Gershow, M.; Stein, D.; Brandin, E.; Golovchenko, J. A. *Nat. Mater.* **2003**, 2, 811. (b) Gershow, M.; Golovchenko, J. A. *Nature Nanotechnol.* **2007**, 2, 775.
- (287) Nilsson, J.; Lee, J. R. I.; Ratto, T. V.; Letant, S. E. *Adv. Mater.* **2006**, 18, 427.
- (288) Wu, M.-Y.; Krapf, D.; Zandbergen, M.; Zandbergen, H. *Appl. Phys. Lett.* **2005**, 87, 113106.
- (289) Ho, C.; Qiao, R.; Heng, J. B.; Chatterjee, A.; Timp, R. J.; Aluru, N. R.; Timp, G. *Proc. Natl. Acad. Sci. U.S.A.* **2005**, 105, 10445.
- (290) Sun, L.; Crooks, R. M. *Langmuir* **1999**, 15, 738.
- (291) Chang, J.; Kosari, F.; Andreadakis, G.; Alam, M. A.; Vasmatazis, G.; Bashir, R. *Nano Lett.* **2004**, 4, 1551.
- (292) Mara, A.; Siwy, Z.; Trautmann, C.; Wan, J.; Kamme, F. *Nano Lett.* **2004**, 4, 497.
- (293) Kasianowicz, J. J.; Brandin, E.; Branton, D.; Deamer, D. W. *Proc. Natl. Acad. Sci. U.S.A.* **1996**, 93, 13770.
- (294) (a) Kasianowicz, J. J.; Henrickson, S. E.; Weetal, H. H.; Robertson, B. *Anal. Chem.* **2001**, 73, 2268. (b) Kasianowicz, J. J.; Nguyen, T. L.; Stanford, V. M. *Proc. Natl. Acad. Sci. U.S.A.* **2006**, 103, 11431. (c) Robertson, J. W. F.; Rodrigues, C. G.; Stanford, V. M.; Robinson, K. A.; Krasilnikov, O. V.; Kasianowicz, J. J. *Proc. Natl. Acad. Sci. U.S.A.* **2007**, 104, 8207.
- (295) Deamer, D. W.; Branton, D. *Acc. Chem. Res.* **2002**, 35, 817.
- (296) Dekker, C. *Nat. Biotechnol.* **2007**, 2, 209.
- (297) Rhee, M.; Burns, M. A. *Trends Biotechnol.* **2006**, 24, 580.
- (298) Ervin, E. N.; White, H. S.; Baker, L. A.; Martin, C. R. *Anal. Chem.* **2006**, 78, 6535.
- (299) Ervin, E. N. E.; White, H. S.; Baker, L. A. *Anal. Chem.* **2005**, 77, 5564.
- (300) Macpherson, J. V.; Jones, C. E.; Barker, A. L.; Unwin, P. R. *Anal. Chem.* **2002**, 74, 1841.
- (301) Uitto, O. D.; White, H. S. *Pharm. Res.* **2003**, 20, 646.
- (302) Newton, M. R.; Bohaty, A. K.; White, H. S.; Zharov, I. *J. Am. Chem. Soc.* **2005**, 127, 7268.
- (303) White, R. N.; Kohaty, A. K.; Zhang, Y.; White, H. S.; Zharov, I. *Langmuir* **2006**, 22, 4429.
- (304) Li, N.; Yu, S.; Harrell, C.; Martin, C. R. *Anal. Chem.* **2004**, 76, 2025.
- (305) (a) Kobayashi, Y.; Martin, C. R. *Anal. Chem.* **1999**, 71, 3665. (b) Yu, S.; Lee, S. B.; Martin, C. R. *Anal. Chem.* **2003**, 75, 1239.
- (306) (a) White, R. J.; White, H. S. *Anal. Chem.* **2007**, 79, 6334. (b) Lee, S.; Zhang, Y.; Harrell, C.; Martin, C. R.; White, H. S. *Anal. Chem.* **2004**, 76, 6108.
- (307) Saleh, O. A.; Sohn, L. L. *Nano Lett.* **2003**, 3, 37.
- (308) (a) Siwy, A.; Gu, Y.; Spohr, H. A.; Bauer, D.; Wolf-Reber, A.; Spohr, R.; Apel, P.; Korchev, Y. E. *Europhys. Lett.* **2002**, 60, 349. (b) White, H. S.; Bund, A. *Langmuir* **2008**, 24, 2212. (c) Woermann, D. *Phys. Chem. Chem. Phys.* **2004**, 6, 3130–3132.
- (309) Smeets, R. M. M.; Keyser, U. F.; Krapf, D.; Wu, M.-Y.; Dekker, N. H.; Dekker, C. *Nano Lett.* **2006**, 6, 89.
- (310) Stein, D.; Kruithof, M.; Dekker, C. *Phys. Rev. Lett.* **2004**, 93, 35901.
- (311) Hang, B.; Zhang, Y.; White, H. S. *Anal. Chem.* **2004**, 76, 6229.
- (312) Wang, G.; Zhang, B.; Waymont, J. R.; Harris, J. M.; White, H. S. *J. Am. Chem. Soc.* **2006**, 128, 7679.
- (313) Zhang, Y.; Zhang, B.; White, H. S. *J. Phys. Chem. B* **2006**, 110, 1768.
- (314) Wang, G.; Bohaty, A. K.; Zharov, I.; White, H. S. *J. Am. Chem. Soc.* **2006**, 128, 13553.
- (315) Shim, J. H.; Kim, J.; Cha, G. S.; Nam, H.; White, R. J.; White, H. S.; Brown, R. B. *Anal. Chem.* **2007**, 79, 3568.
- (316) White, R. J.; Ervin, E. N.; Yang, T.; Chen, X.; Daniel, S.; Cremer, P. S.; White, H. S. *J. Am. Chem. Soc.* **2007**, 129, 11766.
- (317) Ervin, E. N.; Kawano, R.; White, R. J.; White, H. S. *Anal. Chem.* **2008**, 80, 2069.